Rochester Institute of Technology

RIT Digital Institutional Repository

8-2019

Implantable Microsystem Technologies For Nanoliter-Resolution Inner Ear Drug Delivery

Farzad Forouzandeh

ff7667@rit.edu

Recommended Citation

R·I·T

Implantable Microsystem Technologies For Nanoliter-Resolution Inner Ear Drug Delivery

by

Farzad Forouzandeh

A dissertation submitted in partial fulfillment of the requirements
for the degree of Doctorate of Philosophy in Microsystems Engineering

Microsystems Engineering Program
Kate Gleason College of Engineering

Rochester Institute of Technology
Rochester, New York
August 2019

Implantable Microsystem Technologies For Nanoliter-Resolution Inner Ear Drug Delivery
by
Farzad Forouzandeh

Committee Approval:

We, the undersigned committee members, certify that we have advised and/or supervised the candidate on the work described in this dissertation. We further certify that we have reviewed the dissertation manuscript and approve it in partial fulfillment of the requirements of the degree of Doctor of Philosophy in Microsystems Engineering.

_____

David A. Borkholder, PhD   Date
Bausch and Lomb Professor, Microsystems Engineering

_____

Denis Cormier, PhD   Date
Earl W. Brinkman Professor, Industrial and Systems Engineering

_____

Vinay Abhyankar, PhD   Date
Assistant Professor, Biomedical Engineering

_____

Michael Schrlau, PhD   Date
Associate Professor, Mechanical Engineering

Certified by:

_____

Bruce W. Smith, PhD   Date
Director, Microsystems Engineering Program

_____

Doreen D. Edwards, PhD   Date
Dean, Kate Gleason College of Engineering

ABSTRACT

Kate Gleason College of Engineering
Rochester Institute of Technology

Degree: Doctor of Philosophy   **Program**: Microsystems Engineering

Author: Farzad Forouzandeh

Advisor: David A. Borkholder

Dissertation Title: Implantable microsystem technologies for nanoliter-resolution inner ear drug delivery

Advances in protective and restorative biotherapies have created new opportunities to use site-directed, programmable drug delivery systems to treat auditory and vestibular disorders. Successful therapy development that leverages the transgenic, knock-in, and knock-out variants of mouse models of human disease requires advanced microsystems specifically designed to function with nanoliter precision and with system volumes suitable for implantation. The present work demonstrates a novel biocompatible, implantable, and scalable microsystem consisted of a thermal phase-change peristaltic micropump with wireless control and a refillable reservoir. The micropump is fabricated around a catheter microtubing (250 μm OD, 125 μm ID) that provided a biocompatible leak-free flow path while avoiding complicated microfluidic interconnects. Direct-write micro-scale printing technology was used to build the mechanical components of the pump around the microtubing directly on the back of a printed circuit board assembly. *In vitro* characterization results indicated nanoliter resolution control over the desired flow rates of 10–100 nL/min by changing the actuation frequency, with negligible deviations in presence of up to 10× greater than physiological backpressures and ±3°C ambient temperature variation. A biocompatibility study was performed to evaluate material suitability for chronic subcutaneous implantation and clinical translational development. A stand-alone, refillable, in-plane, scalable, and fully implantable microreservoir platform was designed and fabricated to be integrated with the micropump. The microreservoir consists two main components: a cavity for storing the drug and a septum for refilling. The cavity membrane is fabricated with thin Parylene-C layers, using a polyethylene glycol (PEG) sacrificial layer. The septum thickness is minimized by pre-compression down to 1 mm. The results of *in vitro* characterization indicated negligible restoring force for the optimized cavity membrane and thousands of punctures through the septum without leakage. The micropump and microreservoir were integrated into microsystems which were implanted in mice. The microtubing was implanted into the round window membrane niche for infusion of a known ototoxic compound (sodium salicylate) at 50 nL/min for 20 min. Real-time shifts in distortion product otoacoustic emission thresholds and amplitudes were measured during the infusion. The results match with syringe pump gold standard. For the first time a miniature and yet scalable microsystem for inner ear drug delivery was developed, enabling drug discovery opportunities and translation to human.

Acknowledgements

To my parents, thank you for believing in me at an early age. I always knew that you wanted the best for me. I am especially grateful for supporting me emotionally and financially. To my mother, for inspiring me to be dedicated to my career. To my father, who taught me how to have a good understanding of the world around me and think big. Thank you for guiding me integrity and the core values that I live my life by. To my sister, Firouzeh, who has always been a figure of a successful and down-to-earth person for me since childhood. To my brother, Farhad, who has believed in my talents since childhood and has always helped me to grow. To my sister, Farisa, who taught me how to plan for my work, for spending hours with me during the tough days of my life to help me. Thank you for inspiring me to find my path for more peace in my life. To my family, thank you all, this is just as much your Ph.D., as it is mine.

To Dave, my advisor, one of the smartest people I have ever met in my life. If I want to list out all the things you taught me, it would perhaps require another chapter in this thesis. I specifically appreciate you for teaching me 'thinking out of the box' as a real thing, not just a nice slogan. I would not be where I am today without your inspiration and support. I am looking forward to sharing my professional future and career with you as a lifelong friend.

I would like to thank Bob Carter for helping me, especially in the early stages my Ph.D. I also appreciate our collaborators at the University of South Florida, Xiao xia, Bob, and Joe, for their guidance and patience. I would also like to thank my seniors in Borkholder Biomedical Microsystems Laboratory. Thank you Nick, for helping me to cope with the difficulties in my professional career. Thank you Jing, for working with me especially in my early days at RIT to get handy with microfluidics approaches. Additionally, I would like to thank Ahmed for involving in long, inspirational conversations with me on the micropump project, opening doors to me to understand and solve many issues that came along.

Finally, I would like to thank my entire committee, my department, and Lisa Zimmerman. It has been a pleasure to be part of the microsystems department. I could not be more grateful for all that I have experienced and learned.

Contents

List Of Figures

List Of Tables

Chapter 1   Introduction To Inner Ear Drug Delivery

1.1 Introduction

In this chapter a brief introduction for inner ear drug delivery is presented. In the 'auditory dysfunction therapy development' section major auditory issues and available therapies are discussed, along with the necessity of therapy development. Benefits and challenges of site-directed delivery methods in mice are presented in the next sections. Finally, the advantages and challenges of microsystem-based delivery methods are discussed, along with objectives of this thesis.

1.2 Auditory dysfunction therapy development

Hearing loss affects 466 million people worldwide as estimated by the World Health Organization in 2018 [1]. Sensorineural hearing loss (SNHL) is of the most common inner ear diseases [2], which is caused by damage to or death of hair cells due to aging disease, drug ototoxicity, or noise exposure. SNHL accounts for 90% of permanent hearing loss, affecting approximately 278 million worldwide [3]. According to the American Speech-Language-Hearing Association, SNHL rarely responds to current medical or surgical therapies.

Current treatments for hearing loss include cochlear implants or hearing aids, which do not address the biological cause of hearing loss, instead reduces the symptoms by amplifying sound with low efficacy. There are several bases for hearing loss, such as hair cell damage due to aging and noise damage, which each of them needs targeted therapy. To address these biological bases gene, stem cell and pharmaceutical-based therapies for auditory dysfunction have been investigated. Gene-based therapies can ameliorate or cure some types of auditory dysfunctions, which can be delivered either through systemic or site-directed delivery.

Conventional routes for inner ear drug delivery (i.e., injections and oral delivery) are relatively ineffective, principally because of the blood-cochlear barrier [4]–[6], delivery to unintended targets, unknown cochlear drug concentration levels, and toxicity [2]. Furthermore, to deliver a small amount of therapeutic compound a large amount of it

should be taken by the patient (orally, or injection). Finally, due to effects of metabolism and blood circulation on the dose profile, it is a challenge to control the dose profile. In a review paper about bioMEMS devices for drug delivery, Nuxoll & Siegel concluded that success of therapeutic treatments requires site-directed delivery with 'proper temporal presentation' [7]. Site-directed therapies require the desired therapeutics to be delivered in the target site with a controlled dose profile, allowing efficacy improvement and systemic side-effect reduction.

1.3 Site-directed delivery: Benefits and challenges

Site-directed delivery of therapeutic agents with controlled dose profiles has significantly influenced the quality and success of disease treatment [8]. Akil et al. showed the potential benefits of site-directed for deafness research by using gene therapy to restore hearing to a deaf mouse, a mouse model of congenital deafness in human [9]. Delivery was accomplished with microinjections into the cochlea either via an apical cochleostomy or through the round window membrane. Studies like this demonstrate the necessity of delivery directly to the cochlea for therapy development in deafness research.

Targeting the cochlea, Izumikawa et al. successfully regrown auditory hair cells in guinea pigs via intracochlear Atoh1 gene infusion [10]. The importance of site-directed delivery of pharmaceuticals and gene therapies is highlighted in this study. Site-directed, programmable drug delivery systems are needed to leverage recent advances in protective

and restorative biotherapies that have created new opportunities to treat auditory and vestibular disorders [11]–[13].

On the other hand, the inner ear is one of the most challenging drug delivery target organs due to its small size and relative inaccessibility. It is surrounded by the temporal bone, which is the hardest bone in the body and the diameters of the coiled tubes within the inner ear are < 2 mm for human. The cellular machinery within the cochlea (e.g., the hair cells in the organ of Corti) are extremely sensitive to mechanical and chemical damage [2].

1.4 Mouse model system: Benefits and challenges

Rats, chinchillas, and guinea pigs are of interest of researchers [14], mainly due to their larger size, routine surgical approaches to access the cochlea, and larger cochlear volume which makes fluidic access easier. On the other hand, mouse models are beneficial to inner ear studies mainly because their genome is fully mapped, and transgenic mice are available to model human disease in a controlled model system for therapy development.

Transgenic technology has assisted researchers for the *in vivo* study of different genes on auditory function, by enabling gene function studies and modeling human diseases. For instance, Schütz et al. investigated human bilateral middle/high frequency hearing loss, utilizing transgenic mice to replicate mutation in the GJB2 and GJB6 genes, which are the most common cause of prelingual deafness in humans not associated with a syndrome [15].

Further, Inbred mouse strains have been identified to model deafness and presbycusis [16], which is the most common type of SNHL caused by the natural aging of the auditory system. The capacity for regeneration of the same anomaly that causes human deafness in a mouse model enables gene-therapy approach for this type of deafness. Mouse model provides a capacity to study human diseases in transgenic and mutant animals, which makes it a more desirable animal model than large animals such as guinea pigs.

However, working with mouse models presents new and significant challenges for inner ear drug delivery due to the extremely small size of the mouse cochlea. For instance, the mouse cochlea contains approximately 620 nL of fluid (perilymph)[17] while the human cochlea contains 150-200 µL perilymph [18], [19]. This small volume of perilymph in the cochlea makes it vulnerable to prolonged high-flow rate intracochlear delivery [20], [21]. Further, the small size of the cochlea restrains surgical approaches and fluidic interfacing with the mouse cochlea (e.g. [22]).

1.5 Microsystems for inner ear drug delivery

Therapy development is optimized by multiple agent deliveries at desired flow rates and duration for maximum impact. This has been traditionally accomplished only with animals tethered to a syringe as described in [23]–[25]. On the other hand, an implantable pump technology allows user control of the rate and duration of delivery. Implantable devices

facilitate chronic studies by allowing the animal to recover, while syringe pumps only allow acute studies.

To address the challenges regarding running chronic experiments on mice, and for safe and efficacious inner ear delivery, microsystems-based approaches have emerged [8], [26]–[29]. Such systems require precise and programmable ultra-low flow rates with a controllable profile, due to the small volume of perilymph and high sensitivity of the auditory organ to possible damage. Further, a pumping system must be sufficiently small and lightweight, with a planar form factor [30] to be subcutaneously implanted. Also, the system must be robust enough to provide highly controlled, time-sequenced, and ultra-low flow rates over periods of months to years [2], with the capability of remote activation/deactivation, and programming for automated delivery [13].

These and other considerations limit the applicability of many commercially available inner ear drug delivery microsystems-based devices. Current osmotic pumps (e.g., Alzet® micropumps) have been used for preclinical experiments for inner ear delivery in larger mammals, including some rodents [14], [31]–[33]. However, osmotic pumps lack delivery precision and cannot be started or stopped, nor can the flow rate be changed once the infusion is started. Recently, iPrecio® SMP-300 peristaltic micropump was used for infusion of fluorescein isothiocyanate-dextran-labeled dextran as a concentration marker into guinea pig cochlea, using a coupler to connect the tubing of the micropump tubing to a microcatheter [34]. Although these micropumps can provide controlled low flow rates, the overall size and the tubing dimensions are prohibitive for practical subcutaneous

implantation in smaller rodents and mice. Further, the weight of the micropump is 3.3 grams, which is too large for implantation in mice.

Recently a team from Draper Laboratory and the Massachusetts Eye and Ear Institute developed a head-mount reciprocating delivery system for direct intracochlear delivery in guinea pigs utilizing conventional machining and UV laser cutting [13], [35]. The system works based on infusion and withdrawal of the drug through the cochlear perilymph. Although it includes a micropump and a drug reservoir, it is too large for implantation, even in the guinea pig.

Microelectromechanical system technologies (MEMS) have also been used for fabrication of drug delivery microsystems [36]. In 2016, our laboratory reported the development of a miniaturized planar MEMS-based peristaltic micropump for nanoliter cochlear perfusion [37]. However, the device had to overcome significant microfluidic interconnection challenges [38] to allow integration of sub-mm scale in-plane microcatheter tubing without adding significant micropump volume. In addition to microfluidic interconnect challenges, incorporation of control electronics to MEMS-based micropumps can be accomplished either through expensive application specific integrated circuits (ASICS) integrated on-chip or via a separate printed circuit board assembly (PCBA) that adds significant bulk to the assembled system. Scaling of MEMS-based systems also requires modification of the fabrication processes and masks, creating challenges for scalability to human clinical translation.

However, peristalsis remains as one of the most robust mechanisms for drug delivery. Peristaltic micropumps have been widely used in drug delivery applications due to their robustness, precise flow rate, bubble tolerance and resistance to high backpressures, without contaminating the working fluid (drug).

1.6 Objectives

The outcome of this research is intended to be an advanced drug delivery microsystem for inner ear. The microsystem consists of a microreservoir and a micropump that are integrated in a single platform. A novel miniaturized, wirelessly controlled, fully implantable, and scalable phase-change peristaltic micropump that provides programmable and accurate drug delivery for inner ear applications is developed. A miniature, scalable, implantable, and refillable microreservoir is developed.

Novel direct-write printing approaches is used to fabricate the micropump around a catheter microtubing directly on top a Printed Circuit Board (PCB) to integrate the mechanical and control electronic components. The flow path is leak-free and biocompatible and is free of complex microfluidic interconnects. Stereolithography 3D-printing technology is used to build the structure of the microreservoir using a biocompatible resin to enable biocompatibility and scalability.

Background on the peristaltic micropumps is provided in Chapter 2 to provide the necessary information to understand the micropump actuation approach, presented in Chapter 30. The details of the micropump design are discussed in Chapter 3, including design concept, control electronics, heat transfer analysis, and fabrication process. Further, the characterization data for both *in vitro* and *in vivo* experiments are presented. In Chapter 4 the details of the biocompatibility of the materials used in the microsystem are presented along with *in vivo* data. The details of design, fabrication, and *in vitro* characterization of the microreservoir are provided in Chapter 5. The micropump and microreservoir are integrated and characterized *in vivo* (Chapter 6). Future work and final remarks are presented in Chapter 7.
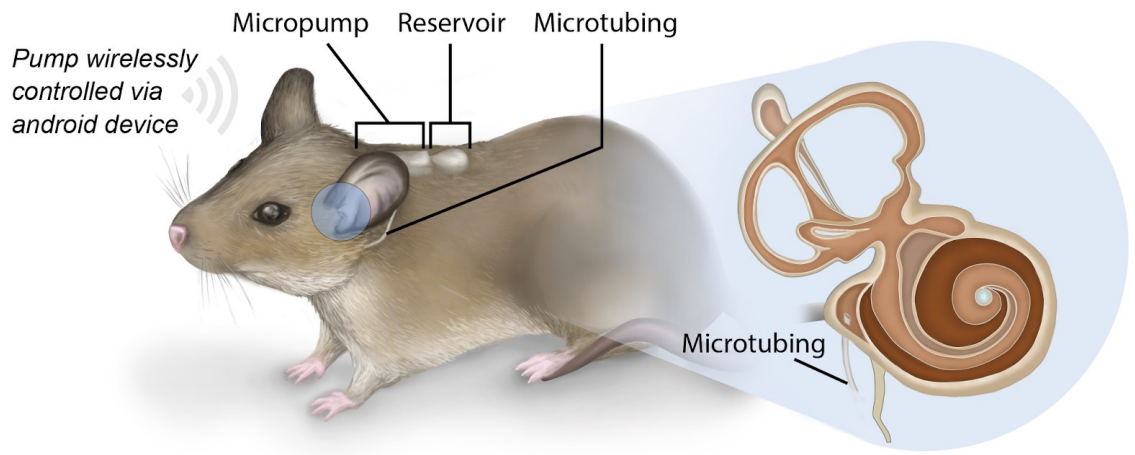
Figure 1.1. A schematic of the integrated microsystem implantation for inner ear drug delivery.

Chapter 2   A Review On Peristaltic

Micropumps

2.1 Introduction

In recent decades, microsystems technology has made significant progress, and it has made an impact on many fields such as biology, biomedical engineering, biochemistry research, among other research areas. Micropumps are the heart of microfluidics systems since they provide the necessary power for moving the working fluid in a microfluidic system. In this work, we use the definition of micropump according to [39], where the prefix 'micro' is considered to be appropriate for devices with prominent features having space dimension scale in the order of hundreds of microns or smaller. Most micropumps can be categorized into two groups: mechanical micropumps (with moving parts) and non-mechanical micropumps (with no moving parts) [39]–[41]. Mechanical micropumps employ

reciprocating pistons or oscillating diaphragms to do pressure work on the working fluid through a deformable and moving boundary in the pumping chamber, while rectification components such as active or passive check valves at the inlet and outlet control the flow direction.

Peristalsis is one of the essential physiological transport mechanisms in living organs and organisms [42], [43], enabling functions such as swallowing, urethral transport, blood flow in the circulatory system, etc. [44], [45]. This elegant transport mechanism has inspired researchers to investigate the applicability of peristaltic pumping in the realm of microfluidic devices. In the literature, peristaltic micropumps (PMPs) are often listed as a subcategory of mechanical micropumps [46], typically with three or more pumping chambers that operate in a particular sequence to push a working fluid in a desired direction within a microfluidic path [36], [39], [41], [46], [47]. The first PMP was introduced by Smits in 1990, using micro-electromechanical systems (MEMS) fabrication techniques. The device had a set of three piezoelectric actuators, which used a six-step sequence to create a peristalsis transport mechanism [48]. This micropump had a maximum flow rate (Q_{max}) of 3 µL/min and a maximum pressure (P_{max}) of 5.9 kPa.

Since the introduction of PMPs, they have been widely used in various applications such as cell sorting/counting and cytometry [49], DNA hybridization [50], gas chromatography [51], droplet microfluidics [52], microfluidic filtration [53]–[55], cell culture [50], [56], blood transportation [57], morphine detection [58], aeronautics [59], biosampling [60], implanted artificial sphincter system [61], multi-organ-chip [62]–[65] , parallel processing

of cell cultures and DNA microarrays [66], and integration to micro total analysis systems [67]. Further, PMPs have been used for drug delivery, such as implantable drug delivery systems [68], high-resolution volumetric dosing [69], size-constrained drug delivery [37], [70]–[73], and insulin delivery [74], [75]. Key features that make PMPs attractive for drug delivery applications are resistance to high backpressure [76]–[78], bubble tolerance, endurance [79], self-priming and bi-directional flow capabilities [78].

This review introduces the peristalsis transport mechanism concept using and defines the different configurations that exist in the literature. This is followed by a discussion on the most critical parameters for the functionality of PMPs. The different actuation methods that have been used to achieve such devices are presented with selected examples from the state-of-the-art of micropumps technology. Finally, the review closes with a discussion, comparison, and evaluation of the developed PMPs over the past 30 years.

2.2 Peristalsis concept

In the literature, PMPs are either frequently categorized either as a subcategory of mechanical micropumps listed as actuation methods or vaguely explained among other micropumps [39], [46], [80], [81]. However, it is important to note that peristalsis is a rectification method in which the working fluid is sequentially actuated to move from inlet to outlet. This review considers peristalsis as a rectification method for mechanical

micropumps, and not as a subcategory of mechanical micropumps [40], [41], [82]. Table 2.1 shows a categorized summary of rectification methods for mechanical micropumps.

Table 2.1. Rectification methods of reciprocating mechanical micropumps.

Dynamic Valves	Active (e.g., cantilever, diaphragm)
	Passive (e.g., flip valves, check valves)
Static Valves	Active (e.g., laser, local heating)
	Passive (e.g., nozzle/diffuser)
Peristalsis	Discrete (e.g., multiple chamber/diaphragm configuration)
	Continuous (e.g., DC motor-driven rollers on microchannels)

The PMPs can be categorized by the fluidic channel configuration either as a continuous-channel or discrete-channel PMP. A continuous-channel PMP design, has its deflecting actuators fabricated around or along a single microtubing (Figure 2.1a), while a discrete-channel PMP is composed by two or more layers to create a microfluidic channel(Figure 2.1b). Typically, discrete-channel PMPs are designed with ports to connect to other elements in a larger system. The multi-layer design approach used for the discrete-channel PMPs usually increases the complexity of the fabrication. This introduces challenges that need to be addressed for a successful device fabrication such as having a strong bond between layers to seal the microchannels and to avoid leakage within the device, layers alignment, channel clogging and addition of port interconnections. In addition, the interface with other elements in the system can increase dead volume at the port

13

connection, and sometimes even making a port connection impossible when working with microdevices with significant small dimensions (e.g., [38]).
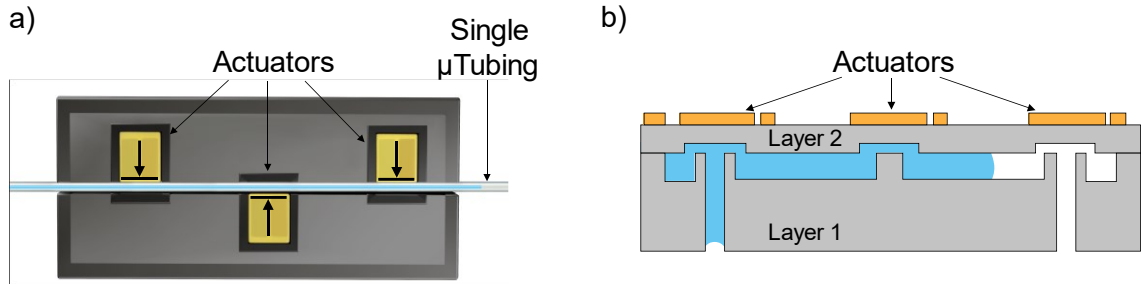
Figure 2.1. Examples of a) a discrete-channel (adapted from [37]) and b) a continuous-channel PMPs (adapted from [53]).

Actuation of the PMPs can also be classified into two general schemes regarding the transportation of the fluid: continuous and discrete. In the continuous scheme the actuator moves along the fluid path (e.g., PMPs with rollers or cams [74], [83]) while in the discrete ones the actuators move perpendicular to the fluid path (e.g., PMPs with piezoelectric or pneumatic actuators [84]–[88]), see Figure 2.2. The operation concept of continuous-scheme PMPs is usually based on the miniaturization of peristaltic pumps. Although the continuous-scheme concept of PMPs has been improved in the past two decades, most of the PMPs in the literature are discrete-scheme, which fits well with the microscale fabrication processes and actuation methods.

In the literature PMPs are usually defined as micropumps with three or more chambers [36], [39], [46], [89]] (Figure 2.2B, C), which are the most common type of the PMPs. However, PMPs with multiple actuators require complicated multiphase excitation controllers limiting their functionality in potential applications. Therefore, researchers

14
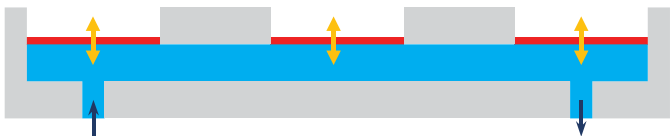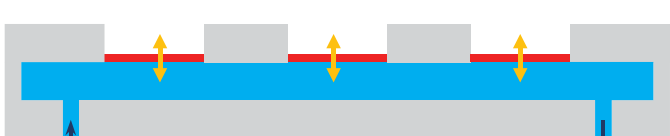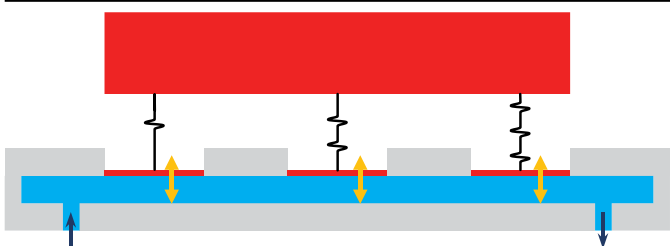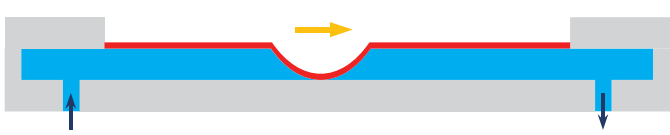
have investigated PMPs with one or two actuators [90], [91]. One of the first two-chamber PMPs was introduced by Berg et al. in 2003 [79], with a structure similar to Figure 2.2A. In this study, two PMPs were developed using two and three actuators, while other parameters remain identical. The micropump was fabricated on glass and PDMS (Polydimethylsiloxane) and used pneumatic pressure as the actuation source. The results show that a two-chamber PMP can provide up to 94% of the flow rate and 73% of the back pressure of the counterpart three-chamber PMP. The study suggests that two-stage PMPs may be a more viable choice in limited chip area conditions, or where the backpressure is low. In 2007, another group reported a backpressure-independent piezoelectric PMP designed for an optimized low flow regime range from 0.1 - 50 µL/min using two chambers[76].

In a discrete-scheme/discrete-channel PMP with a single driving diaphragm and two active valves (e.g., Figure 2.2B), an optimal phase sequence implementation of the diaphragm will induce a peristaltic motion, which can be approximated to a traveling wave. The fluid is set in motion due to the transferred momentum initiated by the diaphragm deflection, without the use of any rectification elements. Since rectification is the prime function of the chambers at the inlet and outlet ports (i.e., valves), this type of PMPs has not been considered as peristaltic devices by some research groups [43]. However, the fluid displacement contribution of these valves can be significant depending on the device design. Therefore, this PMP configuration is often referred as a "peristaltic micropump" by other groups [41], [48], [92]–[97]. All in all, the exact definition of PMPs can be

15

questionable. In this review, the micropumps with one diaphragm and two valves are also considered PMPs, due to the contribution of the valves in the pumping action.

Single-actuator PMPs (SAPMPs) have also been developed to eliminate the necessity of multiphase controllers. One type of SAPMPs have one actuator and one actuation site, where the created momentum is transferred to the fluid by a transverse motion of the diaphragm in direct contact with the fluid. The second type, have one actuator and its actuation is transferred to three or more actuation sites [98], [99](Figure 2.2D). The sequential motion can be realized either by the mechanical properties of a membrane [100]–[103] or by an actuator [104]–[106]. All the reported SAPMPs with this structure are either pneumatic-driven [98], [99], [107], [108] or vacuum-driven [90]. Peristalsis occurs in SAPMPs by using the fluidic resistance of the microfluidic path between the chambers, which enables the required phased lag ($\Delta\phi$) in the actuated system.

Discrete PMPs

Description		Schematic
Multiple actuation sources*	A. Two actuators at the inlet and outlet with a precise timing sequence.	
	B. Three or more actuators while two of them work as active avalves at the inlet and outlet.	
	C. Three or more actuators (Typical)	
Single actuation source	D. Single actuator source with multiple actuatotrs in a sequence that is usually defined by the structure of the sytem and cannot change after fabrication withouth changing parts.	

Continuos PMPs

Single actuation source	E. Usually a DC motor provides the actuation force which is transmitted to the fluid membrane through rollers, balls, magnetic fluids, etc.	

Figure 2.2. Classification of different rectification methods that have been used for PMPs in the literature. In this table, the fluid channel is shown to be discrete for simplification. However, this is not the case for all PMPs. Some pumps use a microtubing/tubing and make the structure around it.

2.3 Significant parameters in peristalsis

Many researchers explored the effect of different parameters on the operation of the PMPs, such as the actuation frequency, the number of chambers, sequence, phase difference, and the working fluid [96], [109]–[112]. One simple way to understand the effect of different parameters affecting the flow rate can be formulated by equation (2.1):

$$Q = \Delta V \times f \tag{2.1}$$

Where ΔV (net volume) stands for the net fluid volume being moved from inlet to outlet by the PMP in a single cycle, f (frequency) stands for the number of cycles in each second, and Q is the flow rate. One way of increasing the flow rate using equation (2.1) is to increase the actuation frequency. Although the equation suggests a linear relationship between the flow rate and the frequency, it is not always the case. The increase in the flow rate due to increasing the frequency depends on the operation conditions such as the response time of the pumping diaphragm, the actuation time of each pumping chamber, and the flow conditions at the inlet and the outlet of the pump, etc. The other way to increase the flow rate is to increase ΔV. The significant factors that influence the net volume are stroke volume (V_{stroke}), sequence, phase difference, and number of chambers. In this section, all these elements are discussed, along with the effect of the working fluid on the functionality of the PMPs.

2.3.1 Actuation frequency

One of the best tools to control a PMP after its fabrication is the tuning of the actuation frequency. A noticeable characteristic behavior can be observed among several variations of PMPs investigated in this study: the flow rate increases almost linearly with the increase of the actuation frequency in the relatively low-frequency range, followed by a maximum flow rate (at f_{Qmax}), and then the flow rate decreases with a further increase of the actuation frequency. Figure 2.3 shows this trend among nine different PMPs with different actuation methods (e.g., piezoelectric, DC motor, etc.). The average line clearly shows this behavior, which is consistent with the graphs reported elsewhere [80], suggesting that this is expected from all micropumps and not just for the PMPs.

This relation enables an effective and reliable way of controlling the flow rate in the linear range. This behavior can be a function of geometry, membrane material and response time of the chambers (which is a function of geometry and material of the chamber, and the actuation method). In [48], the authors discuss that the descending curvature of the flow rate-frequency curve is attributed to the viscosity of the water, as the water resists to be pushed through narrow channels. Further, the actuation amplitude of the chambers is a function of the actuation frequency, in different actuation methods such as piezoelectric and thermo-pneumatic [77]. For instance, in a thermo-pneumatic PMP, the actuation amplitude starts to decrease at frequencies higher than f_{Qmax} because of the decrease in the actuation amplitude of the membrane due to insufficient heating [113]. In some cases, the

actuation frequency is limited to the release time of the membrane. For example, in a pneumatic PMP, the maximum flow rate is constrained by the release time of the compressed air. At high frequencies, the air cannot be released properly, causing a decrease in the flow rate [99].
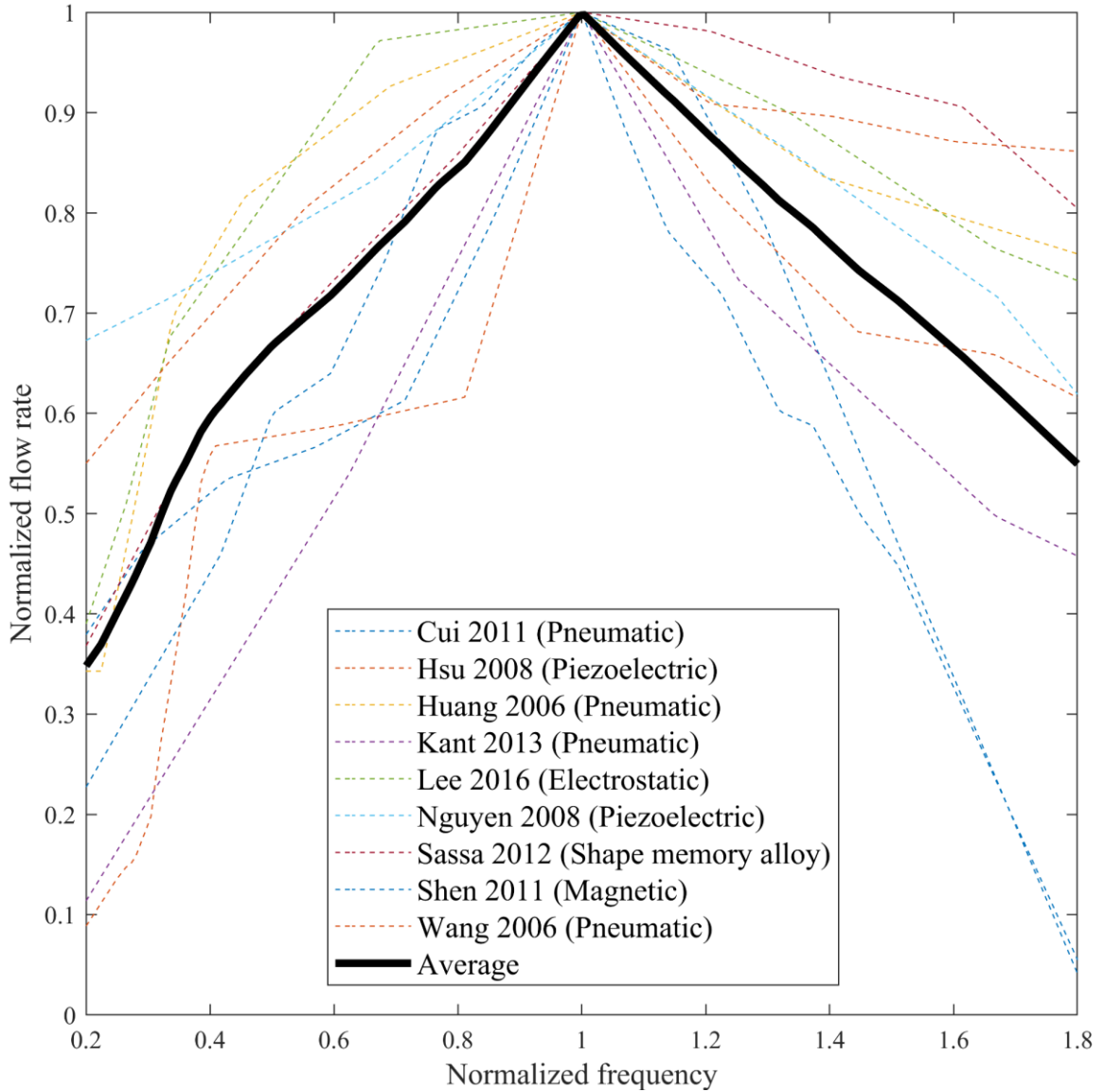
Figure 2.3. Typical Q-f curve for PMPs. The curve shows an average of Q-f curve for nine different PMPs. The flow rates and frequencies are normalized to the values at maximum flow rate. Most of the reports present the linear section of the curve.

2.3.2 Stroke volume

Optimization of the stroke volume is another way to improve the net volume (ΔV) propelled through the system in one cycle. Stroke volume is defined as the volume of the working fluid being swept by each chamber in one cycle. In other words, stroke volume is the difference between the maximum and minimum chamber volume as the membrane actuates in a peristaltic cycle. As the stroke volume increases with the increase of the membrane displacement amplitude, the dead volume decreases. The dead volume is defined as the volume in each chamber that is not swept by the membrane.

The key parameters affecting the stroke volume are the geometry of the chambers, the mechanical properties of the membrane, the working fluid, and the actuation mechanism. Geometry of the PMP structure affects stroke volume by several factors such as size and shape of pumping chambers [114], [115], diaphragm cross-section (e.g. [116], [117]) and dimensions of microchannels (e.g. [114], [118]). It is worth to mention that an optimized geometry can reduce the dead volume (e.g. [117]). Mechanical properties of the membrane such as Young's modulus, Poisson's ratio, and viscoelasticity affect the displacement amplitude and response time of the membrane (e.g. [119]). Further, the actuation mechanism defines the magnitude and frequency of force applied to the membrane, which directly impacts the stroke volume (e.g. [117]). The number of parameters impacting the stroke volume suggests that they should be optimized for each specific design depending on the application.

Several of these parameters have been considered by researchers in analytical and experimental approaches. Huang et al. analyzed the effects of geometry on an S-shaped SAPMP [118]. They changed the width and length of the pneumatic microchannel. They found that the maximum flow rate increased by increasing the actuation length up to a specific point, and then it reduced, suggesting an optimized actuation length for the system. The optimized actuation length in this particular example is due to the increase in the time needed to actuate the pneumatic pressure. Increasing the width of the chamber also has an optimized flow rate. In both cases, the flow rate follows similar curves, suggesting that the main affecting element is the fluidic resistance. Wang and Lee reported the effects of actuation pressure in a pneumatic-driven PMP [99]. In one of their experiments, they tested actuation pressures of 10, 15, and 20 psi using an S-shaped SAPMP with five intersections, at frequencies ranging from 0 to 20 Hz. They found that increasing the actuation pressure from 10 to 15 and 20 psi increases the maximum flow rate by 58% and 21% respectively due to greater membrane displacement, and therefore, larger stroke volume. Lee et al. developed a novel fabrication method to reduce the dead volume in a PMP with an electrostatic actuation mechanism for a gas chromatography application [120]. In this study, a 3D fabrication technique known as detachment lithography was employed to fabricate a stepwise chamber to minimize the dead volume.

2.3.3 Working fluid

Although working fluid is not one of the structural or functional elements of a PMP, it can affect the stroke volume significantly. Thus, it should be considered by the researchers and engineers for the design and fabrication of a PMP. Viscosity is the dominant reason for the effect of the working fluid on the volumetric flow rate. In 2005 Goldschmidtböing et al. developed a generic analytical model for micro-diaphragm pumps with active valves, in which fluidic resistance has a direct relation to fluid viscosity since they considered viscous losses to be dominant [96]. They show that modeling the behavior of PMPs by treating only the viscous forces at the valves is valid as long as the frequency is relatively low (in the order of tens of Hz) and the flow regime is laminar, which is the case for most PMPs. Goulpeau et al. considered the effect of working fluids with different viscosities on the flow rate of a PDMS-based piezoelectric PMP [121]. There is almost a linear relationship between the maximum flow rate frequency and maximum flow rate when the viscosity is increased. They found out that the viscosity of the working fluid controls the low-frequency working range ($<f_{Qmax}$).

Jeong and Konishi developed a PDMS-based pneumatically-driven PMP with three chambers, two of them in inlet and outlet [122]. They compared the effect of working fluid by testing DI water, a mix of DI water and glycerin (glycerin mix), and diffusion pump oil (oil) with viscosities of 1, 5, and 21.7 cps and densities of 998, 1035, and 939 kg/m^3. The results show that for the glycerin and oil mix, the flow rate reduces by 17% and 88%,

respectively. Note that the density of glycerin mix is higher than that of DI water, while the density of the oil is lower than the DI water, but in both cases the flow rates decreased, suggesting that viscosity is the dominant factor. Vinayakumar et al. found the effects of using different flow rates in a continuous-channel DC motor-driven PMP [74]. They found the effects of using Isopropyl Alcohol (IPA), silicone oil, and Dimethylacetamide (DMA) as the working fluid. Their results show that utilizing IPA, silicone oil, and DMA reduces the flow rate compared to DI water by 6%, 9%, and 9%, respectively.

The working fluid can also impact the deflection of the membrane. Lee et al. reported the effects of using air and DI water as working fluid on both the deflection of the membrane and the flow rate in a piezoelectric PMP [116], [123]. According to this report, when pumping air the membrane deflection of their circular diaphragm is larger, with an increase of 397% along with a 371% increase in the flow rate. In a study by Hsu et al., the authors compared the deflection of membranes and the flow rate in a piezoelectric PMP, using blood and water as the working fluid [57]. The results show that the use of blood as the working fluid causes a reduction in diaphragm deformation and flow rate by 66% and 54%, respectively. The working fluid can also affect the maximum backpressure and the maximum flow rate frequency of a PMP. Pečar et al. compared the function of their single actuator piezoelectric PMP working with water and air [104]. It has been found that using air as the working fluid increased the maximum flow rate frequency and the maximum flow rate by 100% and 277%, while reduces the maximum back pressure by 82%.

2.3.4 Sequence and phase difference

The sequence of actuation of the chambers directly affects the flow rate, since it determines the number of pumped boluses of the working fluid in each cycle. Researchers have investigated the operating sequence parameter with numerical, computational, or experimental methods. The optimization of the actuation sequence improves the control of the flow rate of the PMPs, where the sequence is not embedded as part of the device such as the PMPs that have magnets or cams on a motor shaft [124] or SAPMPs (e.g. [98], [103], [104], [106]). This section describes the effect of the sequence variation for PMPs operation with three and four chambers. Other sequences for operating PMPs with two chambers (e.g. [79]), and more than four chambers (e.g. [113]) have also been reported.

In 2008, a study compared three phase difference actuation sequences (Figure 2.4) for a piezoelectric bimorph cantilever-actuated PMP with three chambers [125]. The results show that the 120° signal provided the highest flow rates and backpressures in different actuation frequencies, followed by the case of 90° and 60° signals. The reason for this can be that for the 120° signal, at least one chamber is entirely closed in the whole cycle. In the case of 90° signal between step two and three, there is a moment in which all three chambers are open. For the case of 60° signal, the situation is worse: in step three, all three chambers are open.
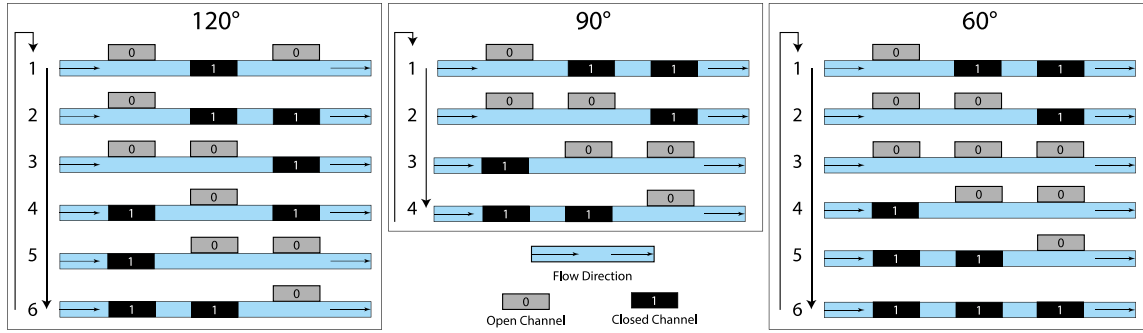
Figure 2.4 Three different sequences have been compared in. The results show that a maximum flow rate occurs in 120° case, followed by 90° and 60°. The legend represents with "1" and "0" a closed (actuated) or open (deactivated) chamber, respectively. The arrows represent the flow direction. " Adapted from [125]".

Jang et al. studied different cycles for piezoelectric-driven PMPs with three chambers in several publications [78], [126], [127]. In all these studies, 191µm thick lead-zirconate-titanate (PZT) bulks were bonded to a glass diaphragm with a diameter of 12mm and thickness of 191µm, with 200µm deep channels connecting them. The depth of the chambers was 30µm. Figure 2.5 shows the sequences that have been used in these studies. The results show that although the maximum membrane displacement is almost equal in all cases, the maximum flow rates are $Q_A > Q_B > Q_C$. It is also reported in [78] that at the maximum flow rate frequency, the same phenomenon occurs at different actuation voltages. They also show that at 100 Hz the power consumption is almost equal in all cases, suggesting that the case A and the case B are more power efficient than the case C, considering their higher flow rate. Finally, they show that the maximum backpressure at the maximum flow rate frequency, applying a maximum voltage increases by 57% and 70% in cases B and A compared to case C. The same group also published a paper in 2008, in which every other geometrical element is the same, along with the actuation sequence, but the chamber thickness is 10 µm, instead of 30 µm which is the case for their previous

26

publication [128]. They show that the maximum flow rate is $Q_B > Q_A > Q_C$. The latter,

shows that the dependency of the flow rate on the actuation sequence is subjective and

needs to be analyzed for each system.
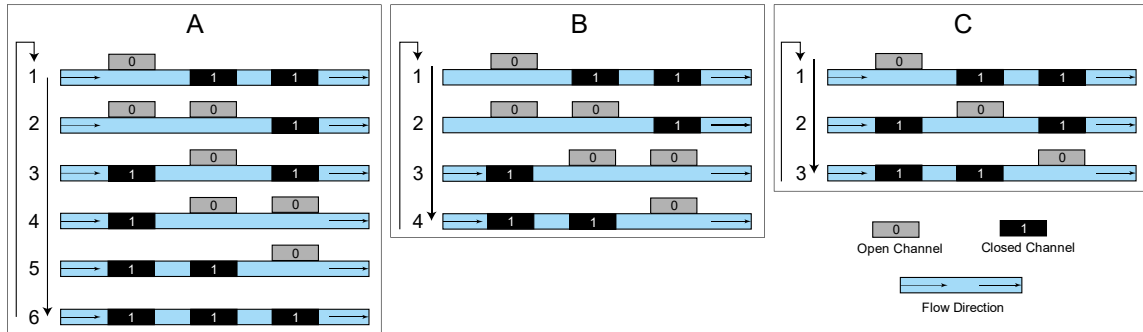
Figure 2.5 Three different sequences were compared in a PZT-driven PMP. Their results show that the maximum flow rate is for case A, followed by B and C. The legend represents with "1" and "0" a closed (actuated) or open (deactivated) chamber, respectively. The arrows represent the flow direction. "Adapted from [78], [126], [127]"

Yang and Liao investigated the effect of actuation sequence on the flow rate of thermo-

pneumatic PMP for three, five, and seven chambers [113]. For the case of three chambers,

they compared a three-phase and four-phase actuation identical to the ones described in

Figure 2.6B and C. They found that in all the frequencies, the flow rate in the case of the

three-phase is larger than the four-phase, with an approximate of 5% difference in the

maximum flow rate frequency. The maximum flow rate frequency is almost equal in both

cases. The results contradict the results found by Jang et al. suggesting a dependency

optimization of the actuation cycling on various parameters, including geometry and the

actuation method. Lee et al. investigated the effect of actuation cycles for an

electrostatically driven PMP with four actuation sites [51]. In this pump, all chambers are

connected, and four actuators are located sequentially. They compared four different

actuation sequences shown below. The results show that the maximum flow rates are Q_D > Q_C > Q_B > Q_A (Figure 2.6).
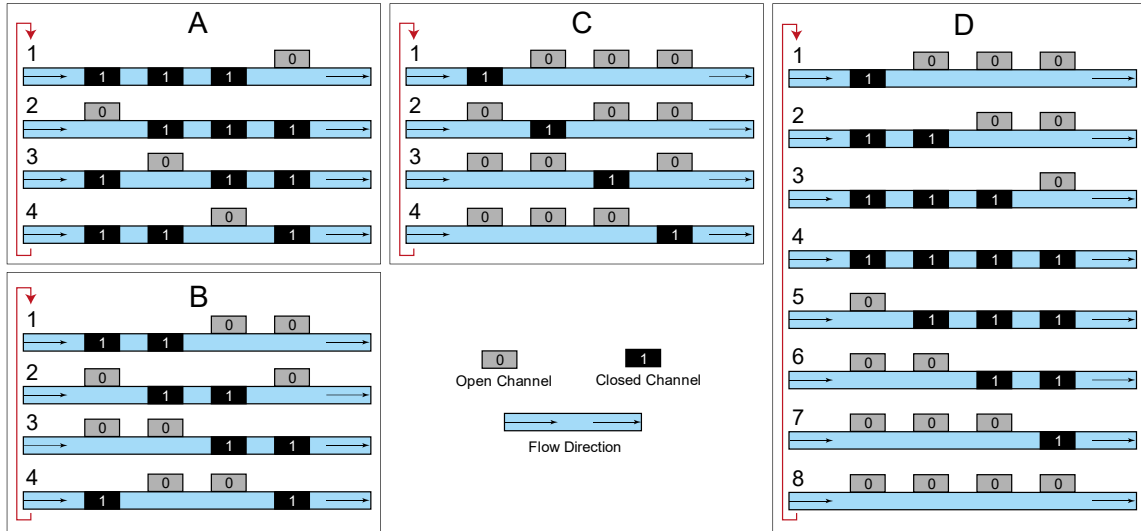
Figure 2.6. Four different sequences have been compared in an electrostatic PMP. According to their results, a larger maximum flow rate occurs in cases D, C, B, and A, respectively. The legend represents with "1" and "0" a closed (actuated) or open (deactivated) chamber, respectively. The arrows in the channel represent the flow direction. "Adapted from [51]"

Although many studies consider the effect of different sequences on the flow rate and maximum backpressure of the PMPs, only a few of them consider the effect of phase-lag, $\Delta\phi$. Leu et al. analyzed the effect of phase difference and the number of chambers on the flow rate of PMPs using both numerical and experimental approaches [47]. In this study, a simple sequence was investigated in which chambers close consequently with equal phase-lag. In both numerical and experimental studies, they changed the phase-lag from 10° to 120° and found its effect on the flow rate. They found that the optimization of the phase-lag can increase the efficiency by up to six-fold. They also found that the optimized phase-lag decrease by increasing the number of chambers. Further, the effect of optimization of

the phase-change increases by increasing the number of chambers (e.g., in the case of the three chambers optimization, the flow rate increases by 17%, while in the case of eight chambers the flow rate increase is of 233%).

2.3.5 Number of chambers

A different way of increasing the net volume is to increase the number of chambers, which can be linearly proportional to the net volume [16], [47]. It should be taken into account that the increase in the number of chambers increases the number of boluses being pumped in each cycle if a proper sequence is provided. If we have n phases for n chambers in a cycle of a sequence in which two chambers are always closed, in each cycle n-2 boluses are pumped. Also, the increase in the number of chambers increases the overall actuation time, considering a fix actuation time for each chamber (T). For example, in the case of three, four, and five chambers in a sequence in which two chambers are always closed, the number of boluses (V) in each cycle changes from $1V$ in the case of three chambers, to $2V$ and $3V$ in cases of four and five chambers. Thus, the overall time of a cycle increases from $3T$ to $4T$ and $5T$, resulting in flow rates of 1/3 Q, 1/2 Q, and 3/5 Q ($Q = V/T$) for cases of three, four, and five chambers. Therefore, the total flow rate (Q) is a function of both the number of boluses and the number of chambers (see Figure 2.7A). This analysis can be expanded to more chambers, as depicted in Figure 2.7B.

Wang and Lee developed a pneumatically-driven SAPMP with an S-shaped compressed air fluid path on top of the working fluid channel [99]. The structure enables peristalsis based on the phase-lag in closing the chambers due to the time it takes for the compressed air to travel through the S-shaped fluidic path. In this cycling scheme, the chambers close/open consecutively due to activation/deactivation of the compressed air. They studied the effect of increasing the number of intersections (chambers), while the sequence is inherently fixed. The results show that having five and seven chambers increases the flow rate by 10% and 15% respectively compared to the case of three chambers. Conversely, the maximum flow rate frequency reduces by 24% and 47% respectively, due to the increased time required to close the chambers by increasing the number of intersections.
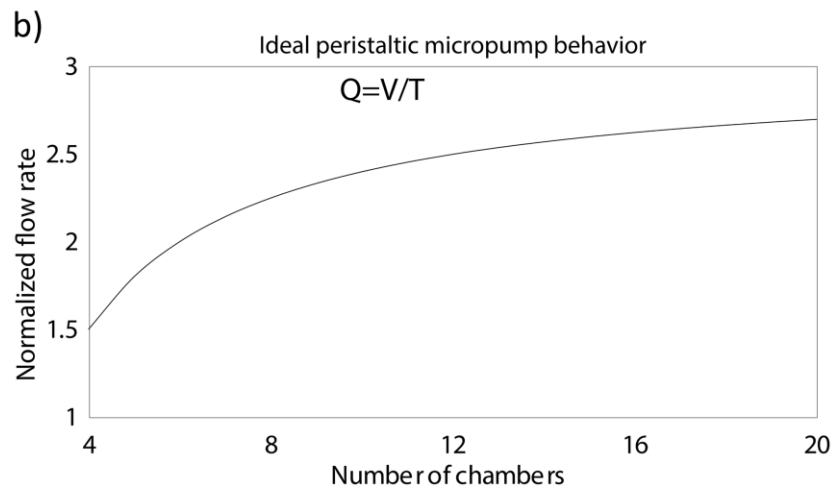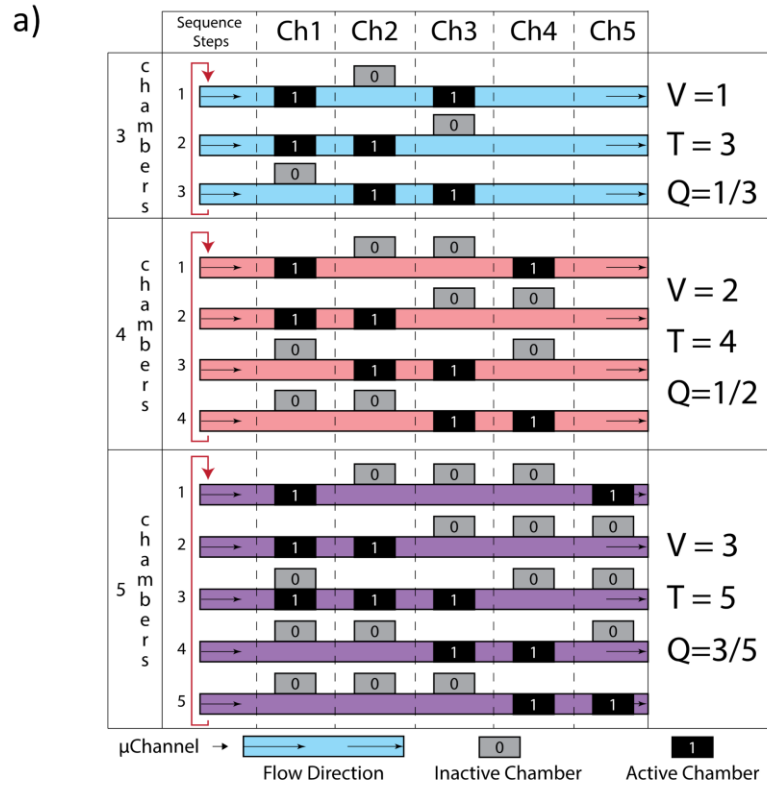
Figure 2.7. a) An ideal comparison in PMPs with three, four, and five chambers showing that for an increasing number of chambers, the flow rate increases in a nonlinear manner. The legend represents with "1" and "0" an active or inactive chamber (closed or open channel respectively), respectively. The arrows in the channel represent the flow direction. V= boluses, T= cycle time, Q= total flow rate. b) Ideal peristaltic micropump behavior, where the increase in the number of chambers increases the flow rate. Note: The flow rate is normalized to the flow rate of a 3-chamber PMP. In all cases, the actuation sequence always guarantees to have two chambers closed.

Yang and Liao investigated the effect of increasing the number of chambers from three to five and seven while a fixed number of phases, in a thermo-pneumatically-driven PDMS-glass-based PMP [113]. They found that increasing the number of chambers to five and seven, reduces the maximum flow rate by 5% and 6% respectively, under zero back pressure. On the other hand, they showed that increasing the number of chambers a significant impact on the flow rate in the presence of higher backpressure. They also showed that increasing the number of chambers increases the maximum working backpressure by 15% and 29% respectively. Their results suggest that increasing the number of chambers requires sequence optimization to achieve higher flow rates.

In another study, Lee et al. fabricated a PMP for gas pumping application with a fixed channel length and several different number of actuators (ranging from 4 to 32)[129]. They operate their PMPs using electrostatic actuation method, with a four-sequence cycle which repeats two, four, and eight times for each case of a varied number of electrodes. By increasing the number of actuators (not chambers) the actuation area decreases, since the overall length of the channel is fixed. The maximum flow rate occurs with the 16-electrodes device, suggesting that there is an optimal number of electrodes for a gas micropump. The existence of an optimal number of chambers occurs due to the compressibility of the gas [129]. Leu et al. developed numerical and experimental studies to find the effect of both the number of chambers and phase-lag between chambers [47]. In the numerical model, they simulated models with identical geometries but a different number of chambers from three to eight chambers. According to computational results, the maximum flow rate increases with the increase of the number of chambers.

2.3.6 Summary of different parameters

PMPs can be optimized based on the requirements of a specific application. Multiple parameters can affect operation of a PMP by impacting the stroke volume and the actuation frequency, as expressed in equation (2.1). The challenge is that these parameters are not independent of each other. For instance, the geometry of the actuation sites, membrane material, actuation method, and working fluid affect the response time of the actuator, which defines the minimum time required to actuate the membranes. This direct effect on the actuation frequency can influence the overall flow rate that can be addressed by adjusting the cycling and the number of chambers. In the same way, it seems evident that the stroke volume increases by an increment of diaphragm deformation amplitude, while it also increases the response time, causing a reduction in the operational frequency. As another example, the maximum flow rate of a pneumatic PMP is a function of the compression and release of the air on the membrane. The compression time is controlled by many factors such as compression pressure, microchannels geometry, etc. The release time is dependent on several elements, such as membrane diameter, membrane thickness, membrane material. Although there are multiple analytical, computational, and experimental [118] studies in the literature, they are all subject-specific. There is no comprehensive report in the literature that considers the effect of all these parameters and provide a general rule of thumb or a general formulation for all cases. It is recommended that for each specific case, the parameters be optimized with analytical, computational, or experimental methods, considering all the parameters above.

2.4 Actuation methods

The actuation method defines the energy source and the mechanism to convert this energy into a displacement of the working fluid. In this section, different actuation methods that have been used in PMPs are described, with a brief definition of the actuation method and chronological development of the method in PMPs.

2.4.1 Piezoelectric

Piezoelectric actuation mechanism works based on the internal mechanical stress due to an applied electric potential. The piezoelectric actuators are fabricated in the form of discs, bimorphs, or stacks that are bonded to the actuation membranes, or directly deposited on them or embedded in the membranes. The first PMP was a piezoelectric-driven silicon-based device fabricated using MEMS fabrication technology. The actuation was enabled with piezoelectric discs on top of glass diaphragms. This pump had a maximum flow rate of 100μL/min at 15Hz operation frequency under zero back pressure. The maximum backpressure was 5.9kPa, with a cut-off frequency of 50Hz. In 2001 a mechanical analysis of piezoelectric PMPs was developed for system design and analysis [68], which was used to fabricate a piezoelectric PMP in 2003 [130]. In the latter, the authors used PZT discs actuators to provide a maximum flow rate of 11.34 μL/min at 130 V operation voltage.

In 2003, Bu et al. provided the design and the analytical evaluation of a piezoelectric-driven micropump for lab-on-chip (LOC) applications [97], which were utilized in the fabrication and characterization of the pump [131], [132]. The pump utilized three 200μm thick PZT discs on glass membranes bonded to a silicon substrate using anodic bonding. The micropump was able to provide 500μL/min at an operational frequency of 100Hz and 200V peak to peak. In 2004, another piezoelectric PMP was fabricated with a silicon-glass structure with a simple fabrication process for controlling biological fluids [116], [123]. Shuichi Takayama's group used piezoelectric bimorphs to actuate multiple computer-controlled movable pins of a refreshable Braille display, which is a tactile device by the visually impaired to read computer text [133]. Each pin can function as a valve that can completely shut the channel by pressing on the silicone rubber medium on the working fluid. The synchronization of the pump is realized through the Braille display software. They demonstrated cell seeding and compartmentalization [133], as well as culture media recirculation [134].

Geipel et al. presented a two-chamber piezoelectric PMP, which operates based on simultaneous closing of the inlet valve and opening of the outlet valve [76], [135]. The micropump works at relatively small actuation frequencies (0.5-5Hz) for piezoelectric PMPs, which shows the idea of two-actuator PMPs can be potentially applicable for slower actuation methods. The micropump provided a maximum flow rate of 40μL/min at 4Hz of operating frequency at zero backpressure. They demonstrated a reasonably constant flow rate over a backpressure range of up to 30kPa. The cut-off backpressure was shown to be directly dependent on the closing voltage of the outlet valve with a maximum value of

100kPa at 140V. The micropump was utilized in a patient-specific drug delivery application in follow-up research [69], which provided resolutions as high as 10nL. Graf and Bowser reported a relatively large PMP using soft lithography for fabrication of PDMS membranes and piezoelectric bimorph cantilevers [125]. They were able to reach a minimum flow rate of 53 nL/min and maximum attainable backpressure of 35 kPa. Nguyen et al. developed a PMP using a lightweight piezo-composite actuator, which is a multilayer composite actuator typically composed of glass-epoxy, carbon epoxy, and PZT layer, reaching a maximum flow rate of 900 µL/min. They also found a linear relationship between the maximum back pressure (P_{max}) and its operating voltage. In 2011 Trenkle et al. fabricated a PMP with a disposable pump body and a reusable actuator, working independent backpressure up to 40 kPa [136] and normally closed up to 100 kPa backpressure.

Nakahara et al. reported the first single-actuated piezoelectric PMP using a traveling wave concept [102], [103] (Figure 2.8A). In this design, a single cantilever-type piezoelectric actuator stimulates an encapsulated incompressible fluid from the bottom, which drives the fluid in the microchannel on top of the encapsulation. A hydraulic displacement amplification mechanism is used to amplify the amplitude of the displacement waves, enabling 1500 µL/min maximum flow rate. In 2014, Pečar et al. reported a single-actuator single-chamber piezoelectric PMP with PDMS structure [104]. In this design, the inlet port is placed in the center of the chamber, while the outlet port is placed further in the chamber. During the excitation, the loosely attached glass membrane and PDMS deform in a controlled manner in which the inlet and outlet are compressed and expanded in a

peristaltic sequence (Figure 2.8B). The micropump provided a maximum flow rate of 240

µL/min and a backpressure performance of 36 kPa. Cazorla et al. employed 1.5 µm thick

Sol-gel PZT thin films for piezoelectric actuation, which reduces the driving voltage down

to 24 V [70]–[72], optimized for implantable drug delivery application.
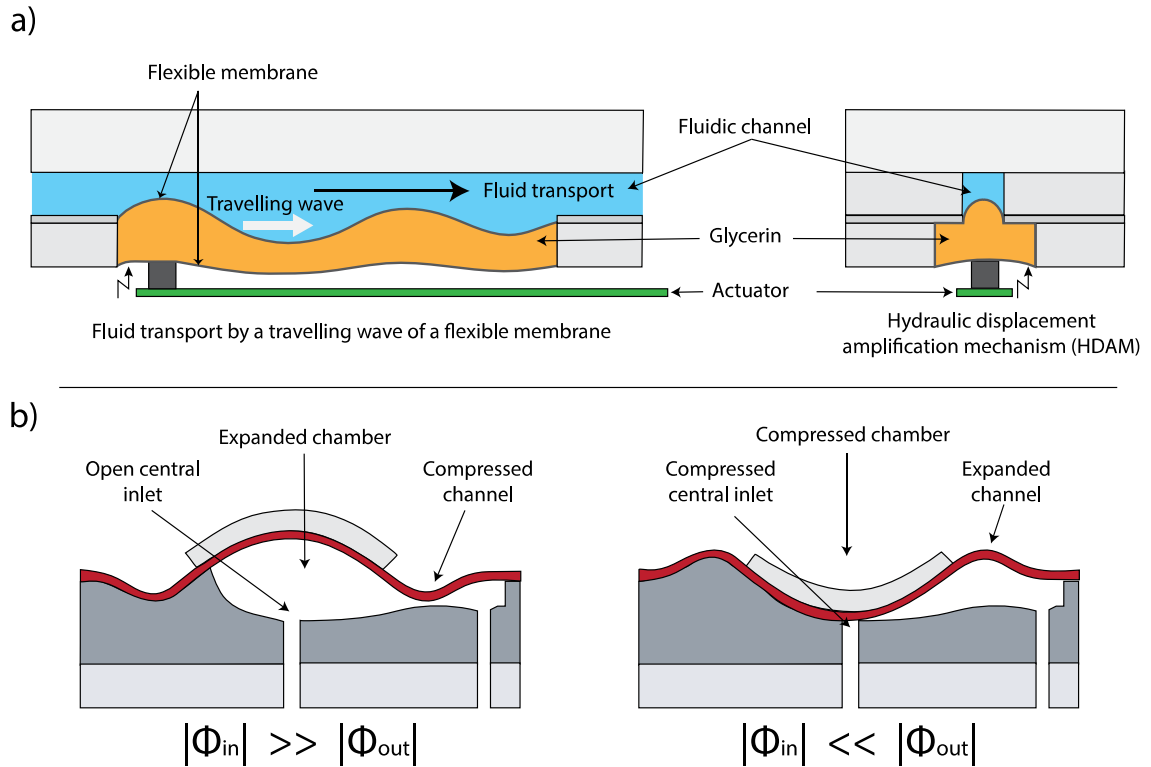
Figure 2.8. a) A Review On Peristaltic MicropumpsCross-sectional and front view of peristaltic micropump using traveling waves on a polymer membrane [102]. The bottom membrane of the hydraulic displacement amplification mechanism is vibrated by an actuator at its edge, and traveling waves are generated in one direction to drive fluid. The long and thin format of this micropump could be beneficial when it is attached to catheter-type devices. (Adapted from [102]) b) A single-actuation piezoelectric PMP developed by Pečar et al. [104]. i) suction phase ii) pumping phase. (Adapted from [104])

2.4.2 Hydrogel

Hydrogels have unique properties that are of interest to researchers due to its stimuli-sensitive characteristic and its relatively ease of fabrication. In 2008, Richter et al. presented a work on a micropump with working principle based on the swelling and shrinkage of temperature-sensitive hydrogels. Hydrogels can be used in automatic and electronically controlled systems. The authors were able to use hydrogels for the implementation of a micropump for the first time, which was capable to operate in two modes: peristaltic and pulsatile. Their PMP was able to achieve a maximum flow rate of 4.5µl/min and a back pressure of 15kPa. Their micropump is composed by a microgel based actuator that is placed in a separate actuation layer, and two active microvalves [Ritcher 2008 - Hydrogel] (see Figure 2.9).
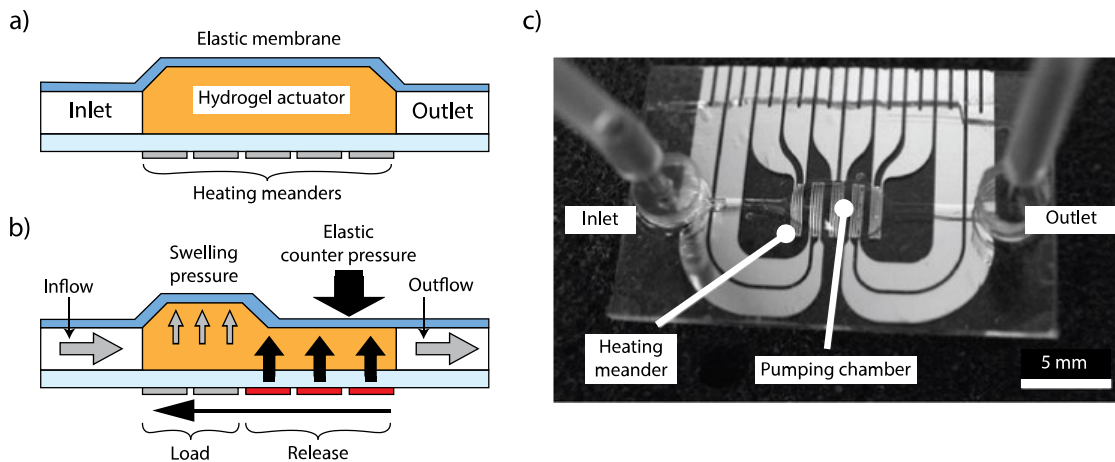
Figure 2.9. Hydrogel PMP a) Schematic set-up. b) Operating principle. (Adapted from [Ritcher 2008 - Hydrogel]) c) Photograph. (Reproduced from [137] with permission from the Royal Society of Chemistry.)

2.4.3 DC or step motor

DC motors are one of the most popular actuation mechanisms due to their simplicity, relatively low power consumption, and rotational motion which can provide peristalsis with reasonably straightforward configurations. To transfer the momentum from the motor to the working fluid, various transmission methods have been implemented, such as magnetic balls, magnets and magnetic fluid, cam-follower, and rollers, which are explained in this section.

2.4.3.1 Magnetic transmission

In this method of transmission, the rotational motion of the DC motor is transferred to the working fluid using magnetic force with either discrete or continuous scheme. In 2004, a DC-driven micropump was reported in which three permanent magnets were stagger-mounted on the shaft of a DC motor, which actuated three chambers that have embedded permanent magnetic rods within the PDMS membrane [124], [138] (see Figure 2.10). The locations of the permanent magnets on the shaft were set to provide peristalsis. The fabricated PDMS-based micropump provides flow rates up to 24 µL/min at a significant low voltage (1 V).

Magnetic fluid has also been employed as a transmission mechanism to transfer the momentum from a DC-motor to the working fluid, in a continuous scheme. In this

mechanism, plugs of the magnetic fluid that are attracted by a permanent magnet push the fluid using a DC-motor that moves the permanent magnet. The magnetic fluid plug can work as a valve when the pump is off using a stationary permanent magnet, enabling a normally closed valve. In 2001, Hatch et al. fabricated a ferrofluidic magnetic PMP in which the ferrofluid is in contact with the working fluid, but the fluids are immiscible [139](see Figure 2.10). This PMP reached a maximum flow rate of 46 µL/min and maximum backpressure of 1.2 kPa. Kim et al. improved the concept by separating the magnetic fluid and the working fluid using a silicone rubber membrane to avoid contamination [140], [141] . In 2008 Yobas et al. reported a self-priming and bubble-tolerant PMP with transmission through three spring-loaded stainless-steel ball bearings rolling on a diaphragm over the microfluidic channel, optimized for a large range of flow rate and small dead volume [117]. By optimization of the number and size of the ball bearings, they were able to reach to a maximum flow rate of ~350 µL/min at 10 rpm (0.17 Hz). Du et al. improved the design by miniaturization of the Yobas et al. work while keeping the broad range of flow rate [142].
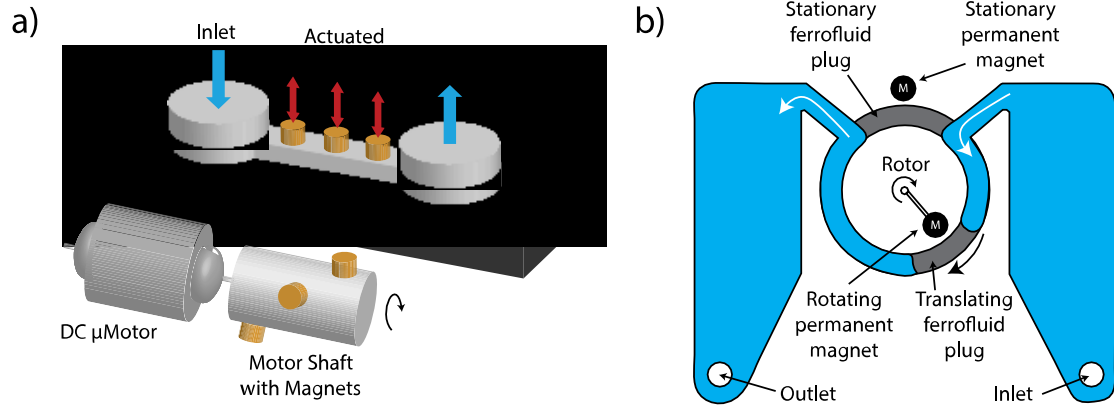
Figure 2.10. a) A DC-motor PMP with magnetic transmission (Adapted from [138]). b) A PMP with DC-motor as the actuator and magnetic fluid as the transmission medium. The magnetic fluid rotates with permanent magnets attached to the DC motor to provide a peristaltic pumping (Adapted from [139]).

2.4.3.2 Roller transmission

Roller-type DC motor mechanism provides continuous-scheme peristalsis, inspired by benchtop peristaltic pumps [114]. In 2003 Lim et al. developed a PMP using ball bearings to transmit DC stepper, enabling extremely low flow rates (3.6 to 144 nL/min) and droplets (50 pL) for microfluidic applications [143]. Koch et al. reported a normally-closed roller-type PMP with both discrete (PDMS-based) and continuous (tubing-based) channels [114] (see Figure 2.11). A PDMS-based PMP facilitates integration into microfluidic substrates, while a tubing-based structure provides an inexpensive, modular medium. The maximum flow rate for the tubing-based and PDMS-based micropumps were 41 µL/min and 27 µL/min, respectively.

Skafte-Pederson reported a relatively small (40 mm × 80 mm) roller-based PMP. The pump consisted of 12 microchannels created by computer numerical control (CNC) micromachining, actuated by eight rollers using a DC motor to promote the portability of the device [66]. In order to address the pulsatile flow rate of the micropump, they designed an offset configuration. They reached a maximum flow rate of 1.59 µL/min with a 10% maximum coefficient of variance between the 12 microchannels. The same research group improved the system and miniaturized it down to 30 mm × 40 mm in a follow-up work [50] as a component of a comprehensive microfluidic system.

Loth and Förster suggested a tubing-based disposable roller-based PMP providing nanoliter handling of the working fluid in high back pressure conditions [45], in which the tubing can be replaced into the cartridge after usage. They achieved an extremely high backpressure of 500 kPa. Vinayakumar et al. reported a cam-follower PMP by mounting a non-concentric cam on the motor shaft and placing a bearing between the cam and a silicone tubing which almost wraps around the bearing [74]. In this way the squeezing and pushing action of the cam spans over 210° of the tubing with minimal friction and wearing because of the valve, enabling normally closed flow path up to 60 kPa backpressure.
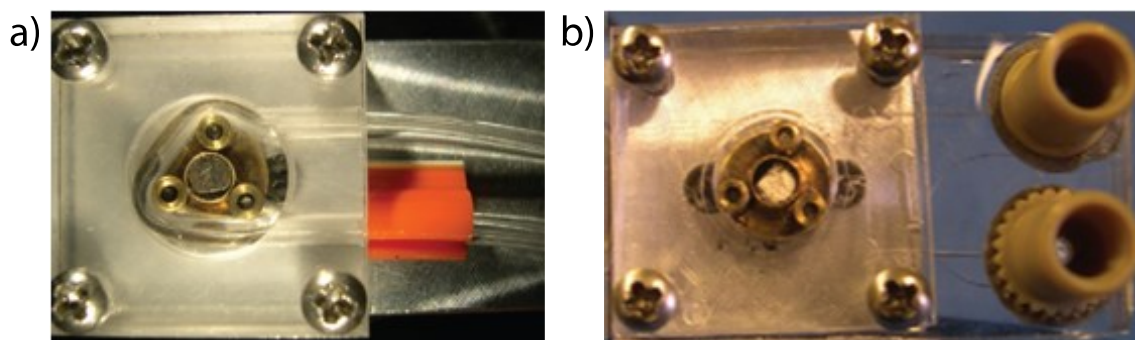
Figure 2.11. A DC motor-driven PMP with roller transmission. Left) A prototype of a tubing-based PMP. Right) a prototype of a PDMS-based PMP (Reproduced from [114] with permission from Elsevier).

2.4.3.3 Cam-follower transmission

Cam-follower mechanism translates the rotational motion of the motor to the working fluid in a peristaltic way by sequentially pushing the fluid in different locations, providing discrete-scheme peristalsis. In 2009 Shkolnikov et al. reported a novel motor-cam mechanism in which a cam drives a plunger arm that provides peristalsis by closing the inlet first, pumping the working fluid out and refilling the silicone tubing [106] (Figure 2.12). Probably the most popular PMP for implantable drug delivery is iPRECIO® [144]–[147], which is a commercially available PMP working based on a patented "Rotary Finger method™" in which a micromotor drives a cam with seven followers (pin fingers). The micropump is integrated with a microreservoir and is packaged with a battery for power supply (Figure 2.12). The micropump is programmable and implantable with a nanoliter resolution over a broad range of flow rates (0.017-1.7 µL/min) with an accuracy of +/- 5% under 0-7.8 kPa backpressure.

Zhang et al. introduced a PMP in which a motor-driven circular cam with a flat side is placed on top of a microfluidic channel which is placed on a substrate that is hooked to a spring at the inlet side of the microfluidic channel, and on a slide rail [148]. In 2016 Xiang et al. developed a cam-follower PMP using soft lithography and 3D-printing technology utilizing three different cams with 120° phase angle differences to actuate three chambers in the desired sequence [119]. They enhanced the closure of the channels by designing two cubic chambers alongside the channel at each compressing zone to reduce the stiffness of the sidewalls.
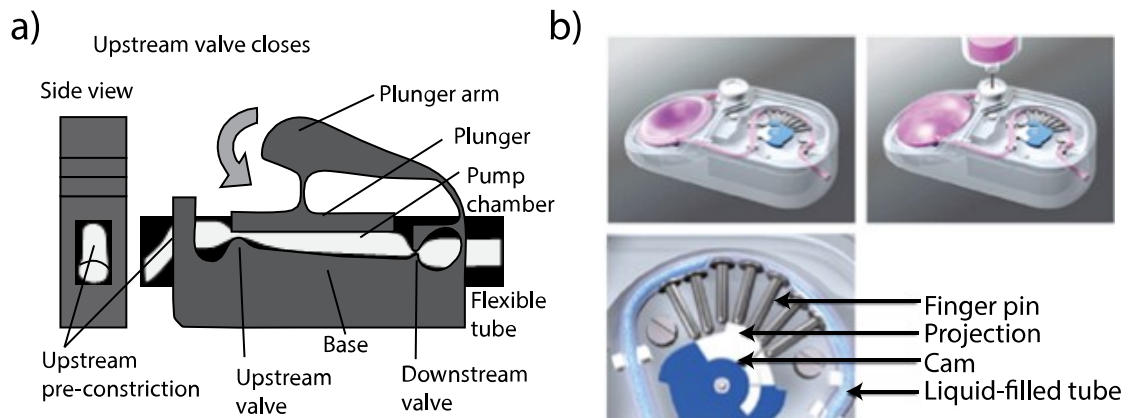
Figure 2.12. a) A novel method for transmission of DC motor rotation into a peristaltic pumping (Adapted from [106]). b) iPRECIO®-SMP300 is one of the most popular PMPs. This micropump works with a DC motor and seven followers (pin fingers) (Reproduced from [111] with permission from Elsevier).

2.4.4 Pneumatic

Pneumatic micropumps use fluctuations in the supply gas (typically compressed air or N_2) pressure to actuate the membrane exposed to it. Usually, solenoid valves are employed for

switching and cycling of the compressed gas. Grosjean et al. demonstrated a self-priming planar pneumatic PMP using acrylic for the structure and a flexible composite for the membrane [92]. They tested the micropump in different supply pressures, sequences, and frequencies to optimize it to provide 120 µL/min. In 2003 Berg et al. reported a pneumatic PMP, using PDMS as the construction and membrane material capable of pumping up to 7.2 µL/min. They showed, for the first time, that PMPs with two actuators can provide comparable flow rates to the three-chamber PMPs, comparing similar prototypes of each.

Wang and Lee presented a SAPMP featuring a serpentine-shape (S-shape) microchannel enabling single source actuation for 3, 5, and 7 actuation chambers [99] (Figure 2.13a). As the compressed air travels in the microchannels, it deflects the membrane with a phase-lag due to fluidic loss of the channels, enabling peristalsis. The same group reported another SAPMP, with time difference actuation due to the different volumes of the chambers [98], see Figure 2.13b. In this case, when the compressed air travels, it closes the smaller chambers first, which causes peristalsis from the smallest to the largest chamber. Jeong and Konishi presented a full-PDMS pneumatic PMP working in the range of tens of nL/min flow rate [122], [149]. Lai and Folch presented a PDMS-based single-stroke PMP in which different chambers have different sizes [107]. The peristalsis occurs based on the principle that the chambers get deflected at different times with a single pneumatic actuation, due to different sizes. This approach enables independence from the interconnections between the chambers. Another PDMS-based single-source pneumatic PMP was introduced using vacuum as the actuation method [90]. Three chambers are connected, and the first chamber is connected to a vacuum source and a vent source. When the vacuum is switched on three

normally-closed chambers open sequentially, and when the vacuum switches off they vent sequentially, enabling peristalsis. In this design, not only vacuum enables peristalsis; it assists debubbling of the working fluid through the gas-permeable PDMS membrane, which is highly desired in the microfluidic applications. They also tried adding valves to increase the flow rates, which enabled up to 600 µL/min flow.

One of the challenges for the operation of complex and integrated chemical and biological processes on a single microfluidic chip is the limitation of the number of pumps and valves. Typically, these challenges cause limitations in the number of pneumatic interconnects available from ancillary hardware. Cole et al. developed a multiplexing approach that significantly reduces the number of these external pneumatic interconnections [150]. In 2014, So et al. developed a novel single-source actuation pneumatic PMP. The device consists of a bilaterally symmetric teardrop shape elastomeric membrane. The membrane was asymmetrically deformed due to pneumatic pressure and then consecutively touched down to the bottom of the chamber, enabling peristalsis [100].
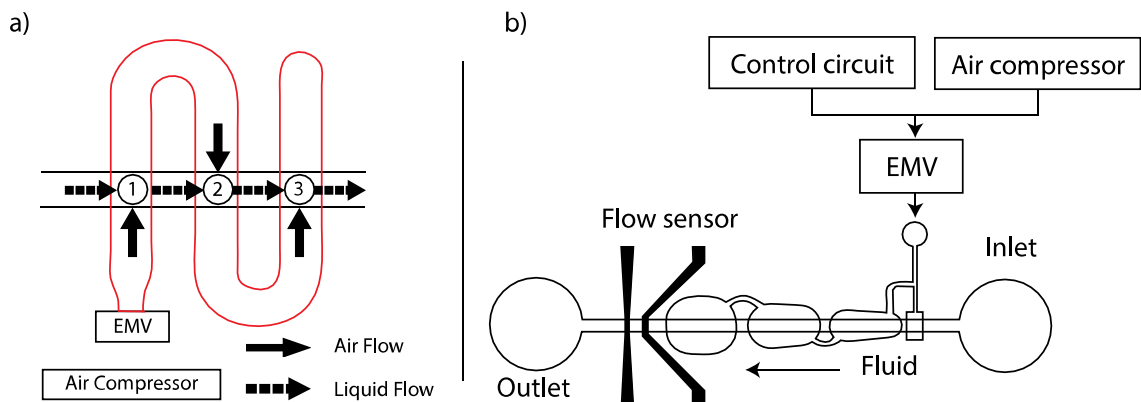
Figure 2.13 Operation mechanism for two single-actuation mechanism PMPs. a) serpentine(Adapted from [99]). b) different chamber sizes (Adapted from [98]).

2.4.5 Electrostatic

Electrostatic actuation is based on the Coulomb attraction force between two plates with opposite charges. Teymoori & Abbaspour-Sani designed and analyzed a $7\times4\times1$ mm^3 electrostatic PMP for medical applications using MEMS fabrication process [151], [152]. According to the simulation results, the threshold voltage of the micropump was 18.5 V, providing 9.1 µL/min, which is suitable for drug delivery applications such as chemotherapy. Although the micropump satisfied many drug delivery requirements such as low power consumption and small chip size, the actual fabricated device with the measured performance was not reported. Xie et al. designed and fabricated an electrostatic PMP using a multilayer technology to isolate the working fluid from the electric field to avoid electrolysis [95], [153]. Furthermore, to avoid electrolysis AC actuation signal was used. The design parameters were optimized analytically using a lumped-parameter model. This small chip size micropump (1.2×0.6 mm^2) achieved a small maximum flow rate of 1.7 nL/min and maximum backpressure of 1.6 kPa at 20 Hz operation frequency.

Patrascu et al. reported an electrostatic PMP compatible with thin film process technology [154]–[156] using Polyimide as the primary material which features thermal and chemical stability, high breakdown voltage, and biocompatibility. The effect of polar and non-polar fluids (e.g., octane) is analyzed, and it was found that polarity reduces electrostatic actuation effect, as expected. The micropump works properly with nonpolar fluids like octane and decane, providing a maximum flow rate of 1.38 µL/min with 150 V operation

voltage. Maffli et al. reported an electrostatic PMP using zipping actuation applied on a dielectric elastomer [157]. Peristaltic pumping using electrostatic actuation for gas chromatography applications was developed by Najafi's group [158]–[164]. Extremely high pressures (for gas micropumps) and low power was achieved by introducing the first multi-stage (2, 4, and 18) electrostatic PMP, using fluidic resonance and multi-stage configuration. They also introduced a honeycomb pump which allows full area utilization, enabling size reduction, and scalability [162]. Another group also employed electrostatic PMPs for gas chromatography [51], [120], [129], [165]–[167] (see Figure 2.14). The micropump has a single chamber with four (or more) electrodes (actuators). They were able to reach 136 µL/min at 90 V actuation voltage and 15 Hz operation frequency.
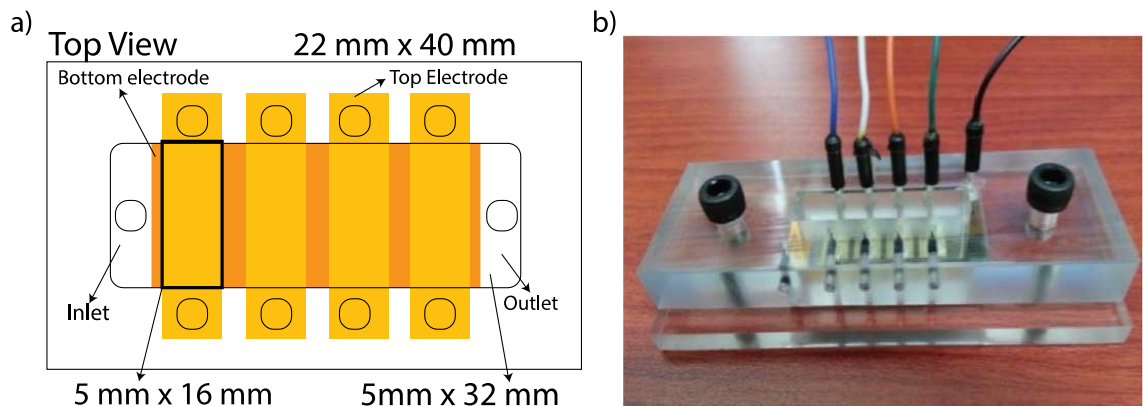
Figure 2.14. Electrostatic actuation method for gas chromatography application. a) Top view of the electrodes design (Vectorized from [51]). b) Fabricated devices (Reproduced from [51] with permission of Elsevier).

2.4.6 Thermopneumatic

A thermopneumatic actuation occurs when a fluid other than the working fluid is heated and then expands without a phase-change, causing the micropump membrane to deflect and move the fluid. Usually, the heater is a thin resistive film, using air as the expanding material. In 1992, a silicon micromachined thermopneumatic PMP was reported [168]. Later in 1999, a thermopneumatic PMP with a flexible composite membrane was introduced. This self-priming PMP uses acrylic for the body and Silicone rubber and parylene-C for the diaphragm to make three chambers for peristalsis. The micropump can provide flow rates up to 6.3 μL/min and backpressure of 3.4 kPa with 291 mW power consumption.

Knight and House provided an electrical characterization for a thermopneumatic PMP for next-generation implantable medical treatment, by considering biocompatibility, simple integration with microfluidics, and particle tolerance [169]. In 2005 Jeong et al. presented a thermopneumatic PMP providing a maximum flow rate of 0.36 μL/min at 2 Hz operation frequency [170] (see Figure 2.15 a and b). The 2.5-mm diameter diaphragm membrane was made of PDMS on top of the glass substrate on which the microheaters were realized. Tuantranont et al. reported a PDMS-based thermopneumatic PMP working in the range of 6-14 V and frequencies of 0.025-0.667 Hz providing 0.82 μL/min [171], [172].

Yang and Liao presented a broad analysis on development and characterization of the thermopneumatic PMPs by presenting three different designs (3-chamber, 5-chamber, and

7-chamber) along with equivalent circuit models and analytical solutions [113]. They fabricated the three PMPs and integrated them with a driving circuit board. A maximum flow rate of 9 µL/min with a backpressure of 0.5 kPa was achieved at 1.5 Hz operation frequency with a duty ratio of 40% using a three-phase actuation sequence. Typically, the disadvantage of the thermopneumatic PMPs is the elevated temperature that the working fluid is exposed to, for the required membrane deformation. In 2011 Chia et al. addressed this issue by designing a side chamber for each actuation site [173] (see Figure 2.15c). In this way, "fluid-squeezing zone" is separated with "air-heating zone," which significantly reduces the temperature elevation of the working fluid.
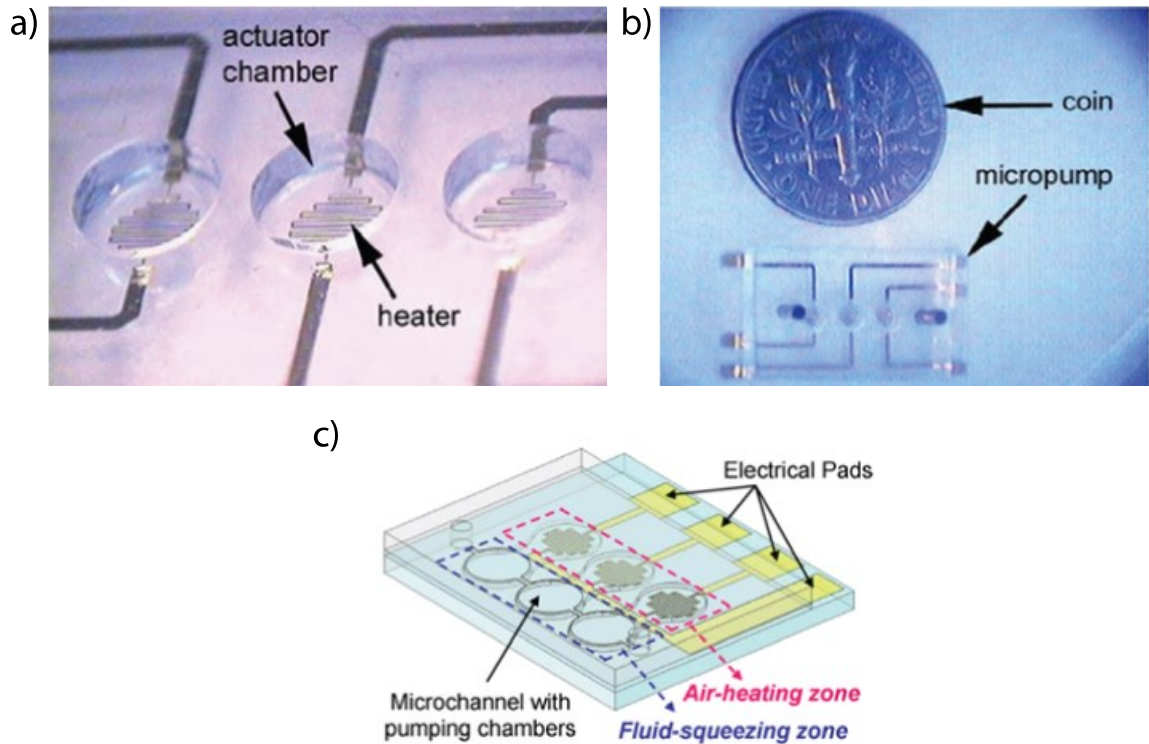
Figure 2.15. a) An image of a PDMS-based thermopneumatic PMP, chambers with the resistive heating element. b) size comparison of the fabricated micropump.(Reproduced from [170] with permission from Elsevier). c) Conceptual view of a peristaltic micropump with low-temperature elevation on working fluid (Reproduced from [173] with permission from Elsevier).

2.4.7 Phase-change

In this actuation method, a phase-change material is heated to melt and volume to deflect a membrane and actuate the working fluid. This method deflects the actuation membrane with lower temperature increase than thermopneumatic method and depending on the phase-change material it can generate higher actuation pressures compared to other actuation methods. In 2016 a normally-closed phase-change PMP was developed using

51

gallium as the actuation material [37] (Figure 2.16a). Since gallium shrinks when melted, the off-condition of the pump resulted in normally-closed chambers due to the expansion of gallium. When actuated (heated), the gallium shrinks in the chambers and opens the chambers. This miniature micropump was able to provide low flow rates of 18-104 nL/min with precision control, suitable for low-flow rate drug delivery and LOC applications. The micropump had a relatively low energy consumption per unit of flow rate (11 mJ/nL) in the class of phase-change micropumps.

In 2019, the same group developed a biocompatible, implantable, scalable, and wirelessly controlled PMP using paraffin wax as the phase-change material for inner ear drug delivery applications [73] (Figure 2.16b). The micropump was fabricated using 3D-printing technology around a catheter microtubing, providing a continuous flow channel. The mechanical components of the micropump were built directly on backside of a PCB, where the actuation control and wireless electronics embedded on its front side; allowing a significant reduction of the overall size of the device. The micropump provided flow rates in the range of 10-100 nL/min flow rate, with 2.4 nL/min resolution. This device was able to operate at ±3 °C change in the ambient temperature and up to a 5 kPa backpressure with no significant impact on the flow rate.
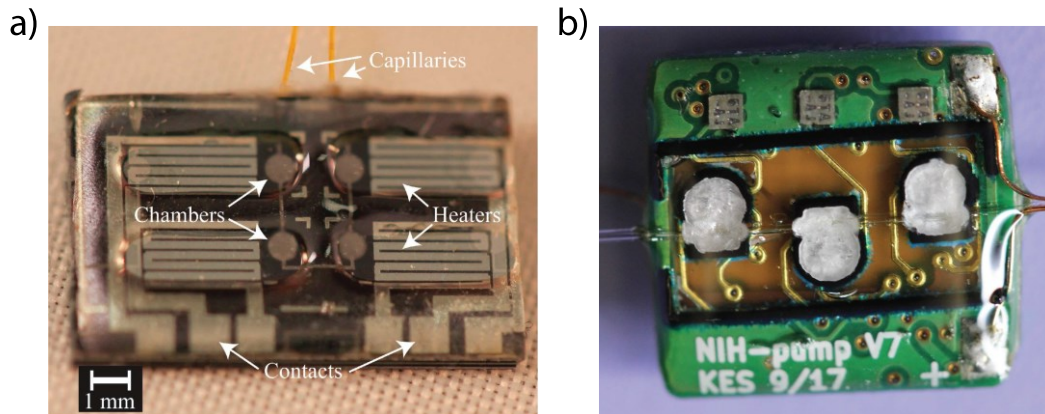
Figure 2.16. Photograph of a gallium-based PMP with plena and capillary tubing. Visible are the interconnected capillary tubes, heaters, diaphragm chambers, plena, and heater contact pads (Reproduce from [37] under CC BY 4.0). b) Photograph of a wax-based phase-change PMP 3D-printed around a commercially available catheter microtubing on the back of a printed circuit board "Reproduce from [73] with permission from Elsevier".

2.4.8 Shape memory alloy

This thermal actuation is based on shape memory effect that involves a transformation between a low-temperature martensite phase and a high-temperature austenite phase (more details in review papers such as [46]). In 2008 Guo et al. introduced a shape memory alloy (SMA) PMP for biomedical applications around a tubing, with low voltage operation (5-9 V)[174]. The rectification was improved by using a check valve. The prototype provided up to 3200 µL/min at operational frequencies of 1-50 Hz. The same group introduced another SMA PMP prototype that used actuators inside a tubing providing up to 900 µL/min flow rate [175]. Sassa et al. developed a SMA PMP by having two simple strips of Ti-Ni SMA actuators around a PDMS tubing for µTAS and LOC applications [91]. The pump provided up to 80 µL/min at ~0.15 Hz, using up to 8 W of power.

2.4.9 Summary of actuation methods

This section described seven different actuation methods along with examples of reported research efforts utilizing them for the development of PMPs. Depending on the application of the PMP, a designer needs to consider the critical characteristics of each actuation method such as size, fabrication complexity, actuation frequency, power consumption, and compatibility to the specific environment. Table 2.2 shows a qualitative comparison of all these methods.

Table 2.2. Qualitative comparison of different actuation methods for PMPs.

Actuation method	Advantages	Disadvantages
Piezoelectric	Fast (low response) High force	High voltage Complex and bulky driving circuit
DC motor	Simple Robust	Relatively large Complex external mechanism for handling rotary motion
Pneumatic	Robust Biomedical application compatible	External compressor required Noisy
Electrostatic	Small Low power large displacement Easy fab process low temperature	High voltage Electrolysis (especially at high voltage)
Thermal (thermo-pneumatic, phase-change, SMA)	Simple driving circuit Simple device structure Low voltage Small size	High power consumption Low actuation frequency

2.5 Evaluation and discussion of peristaltic micropumps

2.5.1 Advantages and disadvantages of PMPs

The majority of mechanical micropumps use static valves or dynamic valves for rectification, which both are categorized into passive and active. The dynamic passive

valves (check valves) require complicated fabrication process for realizing two valves and a diaphragm and have issues associated to clogging and sedimentation, the potential of break and foul in operation [79], and wear and fatigue for long-term application [176]. On the other hand, researchers have used static passive valves such as nozzle/diffuser [177]–[179], Tesla valves [180], [181], or a combination of both [182] to address these problems. Although these valves are robust and straightforward to fabricate, they are relatively inefficient (19-25 % efficiency), vulnerable to backpressure, and inherently unidirectional, while they take large area on the chip surface [79], [177].

Despite valve-rectified micropumps, PMPs are low-cost and straightforward to fabricate since they have similar chamber configurations, enabling easy integration between valves and channels on a single substrate. PMPs have more reliability and endurance compared to check valve micropumps. They also can provide bidirectional flow, which is unique to PMPs and can be significantly useful in LOC applications for circulating flow in microfluidic channels. Also, PMPs have general characteristics of self-priming, bubble tolerance, high backpressure tolerance [46], [76], [78], and multiple fluid channels which can be useful for high throughput LOC application for handling multiple samples at the same time. PMPs provide continuous clean and clogless flow path due to the absence of inline valves which is critical in small fluid channels, and especially to keep the samples without contamination, intact, and unclogged [82], [104], [119]. Due to this characteristic, PMPs have been used in many applications in biomedical, chemical and nutrition, and pharmaceutical industries [183]. Additionally, sensitive biological media or suspensions can be pumped with PMPs due to their gentle operation [184].

Although PMPs have several benefits, they suffer from mechanical wearing, especially the continuous-scheme PMPs. Further, low efficiency is observed in PMPs due to the absence of check valves. One other drawback of PMPs is the complexity of independent synchronized activation of multiple chambers, which is more common in the discrete-scheme PMPs. Researchers have tried to address this issue by developing SAPMPs [100], [103], [105], [106], in which the actuation sequence is embedded into the structure of the device to avoid controlling the sequence with synchronized signals.

2.5.2 Comparison of different PMPs

In this section, we review significant papers that have developed PMPs since their emergence in 1990. Various PMPs have been developed with different actuation and rectification methods, and various applications. Maximum flow rate (Q_{max}) and maximum backpressure (P_{max}) are two of the most significant merits of a micropump [39], [96]. Since many PMPs have been used for size-constrained applications, such as drug delivery, LOC, etc., the overall package size (S_p) is also considered in this report. Where S_p is not reported, the size is estimated from provided images and scales. Actuation voltage (V) is another parameter considered here, which is crucial in drug delivery PMPs (especially implantable devices) due to limitations on maximum voltage. Maximum operational frequency (f_{max}) is also considered here along with the voltage, which determines the operational electronics

and components to drive the PMP. Other parameters are important for PMPs, such as power consumption, which unfortunately are rarely reported.

PMPs have been reported in a variety of designs and structures. Key features and measured performance characteristics of different PMPs are summarized in Table 2.3. Various actuation methods have been reported in the literature: piezoelectric, DC motor, electrostatic, pneumatic, thermo-pneumatic, phase-change, and SMA. In Table 2.3, the PMPs are arranged based on their actuation methods, while other characteristics of them such as application and fluid channel continuity are mentioned. Rectification methods are mentioned, consistent with the definitions in Figure 2.2. For continuous rectification methods, the translational mechanism from DC motor (which is the actuation method for most of them) are provided. Further, the operational characteristics such as V, Q_{max}, P_{max}, f_{max}, and S_p are also provided. For all the PMPs, the working fluid is DI water (among other possible working fluids reported in some papers) unless otherwise mentioned. Figure 2.17 compares reported PMPs based on five different metrics: Flow rate, package size, actuation method, maximum backpressure, and operating voltage. The flow rate is plotted along the ordinate, and the reported or estimated package size are along the abscissa. As depicted in the legend, the actuation methods are distinguished by color, while the data point size represents the maximum backpressure range, and the marker type distinguishes the voltage range.

Table 2.3. Summary of significant PMPs with their experimental output. The data is arranged by groups in based on "actuation method" and in chronological order.

Reference	Actuation method	Rectification	Fluid channel	V (V)	ΔP_{max} (kPa)	Qmax (µL/min)	f_{max} (Hz)	S_p (µL)	Application
Hatch 2001	DC motor	cont. (DC - magnet)	disc.	14	1.2	45.8	0.13	2,401	LOC
Kai 2004	DC motor	disc. (3 chambers)	disc.	1	0.33	24	31	2,340	Drug delivery
Kim 2006	DC motor	cont. (magnet)	disc.	n/r	n/r	3.8	0.13	94	LOC
Abe 2009	DC motor	disc. (DC - cam/follower)	cont.	5		1.7	n/r	2,678	Drug delivery
Koch 2009	DC motor	cont. (DC - roller)	cont.	12	345	41	80	27,060	LOC
Skafte-Pedersen 2009	DC motor	cont. (DC - roller)	cont.	12	370	1.59	0.04	60,800	LOC
Shkolnikov 2010	DC motor	cont. (DC - cam/follower)	cont.	3	48	780	n/r	6,160	General
Shen 2011	DC motor	disc. (3 ch, DC - magnet)	disc.	0.7	7	2400	25	34,560	POC, µFluidics
Loth 2016	DC motor	cont. (DC - roller)	cont.	5.5	500	400	3	57,208	LOC, µTAS, DNA µArray
Xiang 2016	DC motor	cont. (DC - cam/follower)	disc.	12	36	274	2.83	97,628	POC, µFluidics
Vinayakumar 2017	DC motor	cont. (DC - cam)	cont.	5	120	270	n/r	18,963	insulin delivery
Xie 2004	Electrostatic	disc. (3 chambers)	disc.	140	1.6	0.0017	23	n/r	µTAS
Teymoori 2005	Electrostatic	disc. (3 chambers/in_out valve)	disc.	23	n/r	9.1	50	28	Medical
Kim 2015	Electrostatic	disc (18 chambers)	disc.	100	17.5	4000	21	479	Gas chromatography
Lee 2016	Electrostatic	disc. (4+ chambers)	disc.	90	n/r	136	30	12,320	Gas chromatography
Richter 2009	Hydrogel	disc. (5 chambers)	disc.	7	15	4.5	n/r	374	General
Johnson 2016	Phase-change	disc. (4 chambers)	disc.	n/r	n/r	0.12	0.08	36	Size-constrained drug delivery
Forouzandeh 2019	Phase-change	disc. (3 chambers)	cont.	1.8	5	0.1	0.21	192	Drug delivery
Smits 1990	Piezoelectric	disc. (3 chambers/in_out valve)	disc.	100	5.9	100	50	1,500	Insulin delivery
Cao 2001	Piezoelectric	disc. (3 chambers/in_out valve)	disc.	100	0.35	11	4	2,450	Drug delivery
Lee 2004	Piezoelectric	disc. (3 chambers)	disc.	60	3.4	12.5	10	600	µTAS, LOC, FIA
Husband 2004	Piezoelectric	disc. (3 chambers)	disc.	100	n/r	550	100	5,852	µTAS, LOC

Table 3. Summary of significant PMPs with their experimental output. The data is arranged by groups in based on "actuation method" and in chronological order. (continued)

Reference	Actuation method	Rectification	Fluid channel	V (V)	ΔPmax (kPa)	Qmax (µL/min)	fmax (Hz)	Sp (µL)	Application
Geipel 2007	Piezoelectric	disc. (3 chambers)	disc.	110	100	40	4	194	Implantable drug delivery
Nguyen 2008	Piezoelectric	disc. (3 chambers)	disc.	80	1.8	900	160	1,280	Biomedical
Graf 2008	Piezoelectric	disc. (3 chambers)	disc.	90	35	289	40	150,096	n/r
Trenkle 2011	Piezoelectric	disc. (3 chambers/in_out valve)	disc.	140	180	120	30	52,272	Medical
Nakahara 2013	Piezoelectric	disc. Single-actuator	disc.	140	n/r	1500	300	1,800	µTAS
Pečar et al. 2014	Piezoelectric	disc. Single-actuator	disc.	500	36	240	300	952	n/r
Cazorla 2016	Piezoelectric	disc. (3 chambers/in_out valve)	disc.	24	3.2	3.5	2.5	113	Drug delivery
Berg 2003	Pneumatic	disc. (2 chambers)	disc.	n/r	0.17	6.42	0.5	17,671	LOC
Huang 2006	Pneumatic	disc. Single-actuator	disc.	n/r	0.16	108	28	720	µTAS
So 2014	Pneumatic	disc. Single-actuator	disc.	n/r	0.375	18	5	990	µTAS
Cui 2011	Pneumatic (vacuum)	disc. Single-actuator	disc.	n/r	0.8	600	50	108	biological, chemical
Guo 2008	SMA	disc. (3 chambers)	cont.	9	n/r	4000	50	40,500	Biomedical
Sun 2008	SMA	disc. (3 chambers)	cont.	2.5	n/r	900	2	67200	Biomedical
Sassa 2012	SMA	disc. (2 chambers)	cont.	n/r	n/r	80	0.3	1,718	µTAS, LOC
Grosjean 1999	Thermopneumatic	disc. (3 chambers)	disc.	n/r	3.45	6.3	4	970	n/r
Jeong 2005	Thermopneumatic	disc. (3 chambers)	disc.	20	n/r	21.6	100	530	LOC
Yang 2009	Thermopneumatic	disc. (3 chambers)	disc.	5	0.5	9	10	1,584	Biomedical
Chia 2011	Thermopneumatic	disc. (3 chambers)	disc.	9	0.5	20	10	1,440	POC, µFluidics
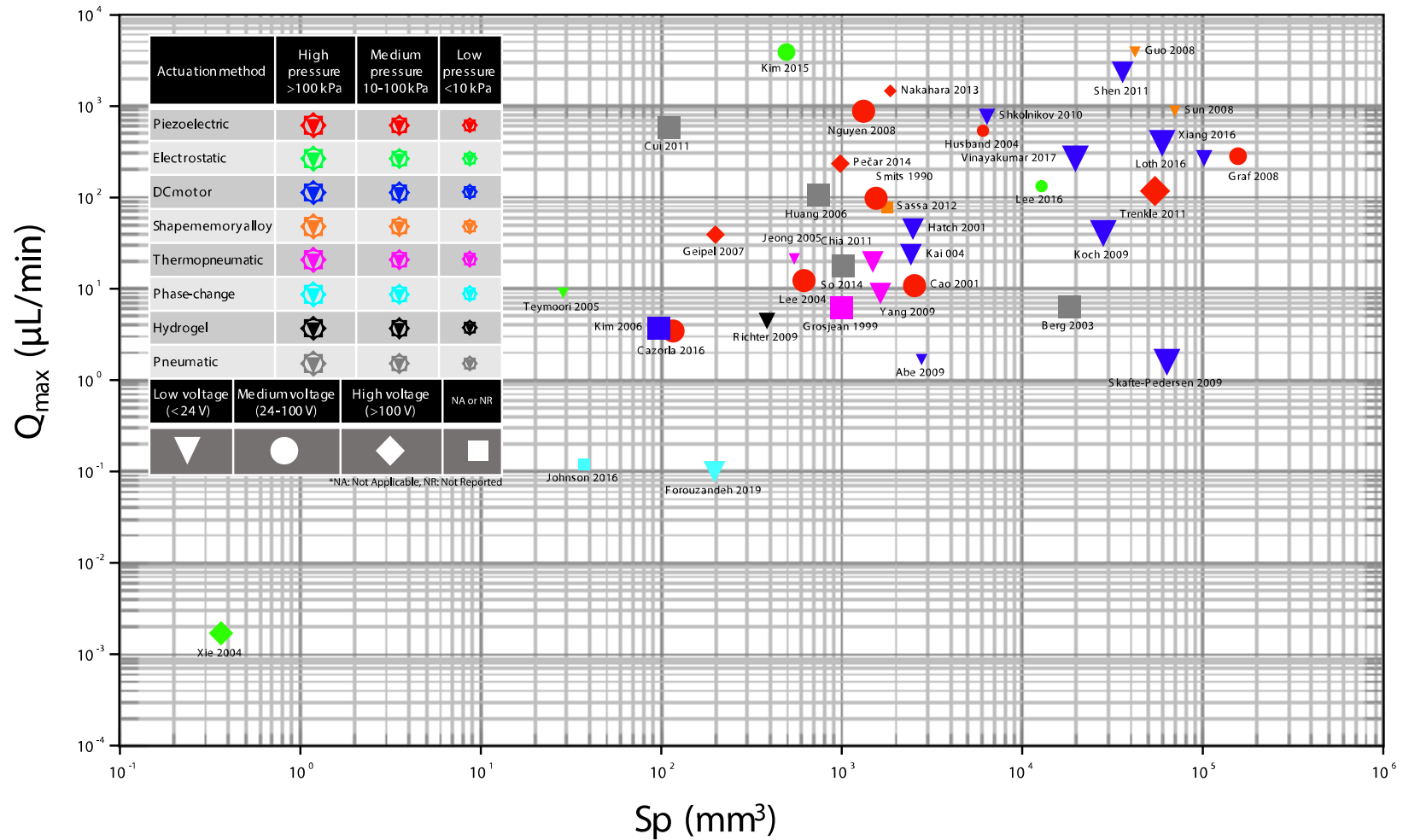
Figure 2.17. Comparison of several reported PMPs based on flow rate, package size, maximum backpressure, actuation method, and operating voltage. *Note: As illustrated in the legend, the color indicates the actuation method, the marker size indicates operating pressure range, and the shape correlates to the drive voltage range.

61

2.6 Conclusion

The brief survey given in this paper reviews a variety of PMP concepts, key parameters affecting pump operation, and actuation methods since their emergence in 1990. The peristalsis concept was explained in depth, defined as a rectification method in mechanical micropumps, and distinguishing it from other rectification methods. Various parameters that substantially impact the operation of PMPs were discussed, including actuation frequency, peristalsis sequence, and the number of chambers. There have been several research efforts in the literature to implement PMPs with various actuation methods. Among different actuation methods, the DC-motor driven ones have gained particular attention and are now available commercially [147]. For extremely size-constrained applications, the bottleneck of size reduction for DC-driven devices is the size of the commercially available DC motors. Reducing the size of reliable and well-controlled DC-motors can substantially assist the miniaturization of DC motor-driven PMPs.

Despite the several advantages of PMPs, such as self-priming, bubble tolerance, and high flow rate and backpressure capability, the actuation sequence is still a source of complexity for discrete-scheme PMPs. To address this challenge, the application of two independent chambers for peristalsis, and SAPMP concept should be considered as a future goal. PMPs with two actuators have been shown in the literature to be relatively efficient [76], [79] but did not gain fair attention afterward. Also, the SAPMP concept has been shown in the literature to be effective for pneumatic [98], [99], magnetic [101], and piezoelectric [102]–

[104] actuation methods. This concept should be considered for the development of PMPs using other actuation methods in the future.

Although the actuation sequence, phase lag, and the number of chambers have been studied subjectively in the literature, a generic model for optimization of these factors can be immensely useful for researchers as a design rule for developing new devices. The parameters discussed in this paper (section2.3) should be taken into consideration, along with the limitations and advantages of each actuation method presented in section 2.4. Optimized devices (considering all factors mentioned above) can compensate for the lack of check valve in the system and improve the efficiency of PMPs.

As mentioned in this paper, the most significant application of PMPs are LOC and biomedical fields, or to be more specific, drug delivery. For both applications, integrability of the micropumps is extremely important. For LOC applications the PMP should be integrated into other features on the chip, where integration with flow sensors assists feedback control in adjusting the flow rate by perhaps changing the actuation frequency as the most accessible post-fabrication control mechanism. For drug delivery applications, especially implanted, the driving circuit and power supply (i.e., battery) size and integration should be considered more thoughtfully, due to extremely size-constrained nature of the application especially for cochlear and ocular applications and animal studies. Miniaturization, low operating voltage, and extremely low flow rates while keeping low power consumption remain essential factors in these applications. Further, implanted PMPs (and in general, micropumps) should be able to be wirelessly programmed and controlled with a relatively simple interface for a medical expert, due to lack of post-implantation

access and reduction of 'human factor' in operation of the devices. For drug discovery applications, scalability should be taken into account to consider animal-to-human translation. This highlights the importance of micro-scale 3D-printing fabrication technology, which is inherently scalable. With these goals, the exploration of new pumping concepts and their realization with MEMS and micro-scale 3D-printing technology will be substantial scientific and engineering challenges.

Chapter 3   A Nanoliter Resolution Micropump

For Murine Inner Ear Drug

Delivery

3.1 Introduction

The cochlea of the inner ear is the specialized organ where auditory perception starts, and is one of the most challenging drug delivery target organs due to its small size and relative inaccessibility. It is surrounded by the temporal bone, which is the hardest bone in the body and the diameters of the coiled tubes within the inner ear are < 2 mm for human. The cellular machinery within the cochlea (e.g., the hair cells in the organ of Corti) are extremely sensitive to mechanical and chemical damage [2]. Successful therapy development for protecting or regenerating cochlear cells which are damaged or missing in cases of hearing loss or deafness, involve the use of transgenic, knock-in, and knock-out

65

variants of human disease in the mouse model system requires advanced microsystems. However, working with mouse models presents new and significant challenges for inner ear drug delivery due to the extremely small size of the mouse cochlea. For instance, the mouse cochlea contains approximately 620 nL of fluid (perilymph) [17] while the human cochlea contains 150-200 µL perilymph [18], [19]. This small volume of perilymph in cochlea makes it vulnerable to prolonged or high-flow rate intracochlear delivery [20], [21].

To address these challenges for safe and efficacious inner ear delivery, microsystems-based approaches have emerged [8], [26]–[29]. Such systems require precise and programmable ultra-low flow rates with a controllable profile, due to the small volume of the cochlear perilymph and high sensitivity of the auditory organ to possible damage. Further, a pumping system must be sufficiently small and lightweight, with a planar form factor [30] to be subcutaneously implanted. Also, the system must be robust enough to provide highly controlled, time-sequenced, and ultra-low flow rates over periods of months [2], with the capability of remote activation/deactivation, and programming for automated delivery [13].

These and other considerations limit the applicability of many commercially available inner ear delivery microsystems-based devices. Current osmotic pumps (e.g., Alzet® micropumps) have been used for preclinical experiments for inner ear delivery in larger mammals, including some rodents [14], [31]–[33]. However, osmotic pumps lack delivery precision and cannot be started or stopped, nor can the flow rate be changed once the infusion is started. Recently, iPrecio® SMP-300 peristaltic micropump was used for

infusion of fluorescein isothiocyanate-dextran-labeled dextran as a concentration marker into guinea pig cochlea, using a coupler to connect the tubing of the micropump tubing to a microcatheter [34]. Although these micropumps can provide controlled low flow rates, the overall size and the tubing dimensions are prohibitive for practical subcutaneous implantation in smaller rodents and mice.

Recently inner ear drug delivery microsystems have been an evolving focus of research. A team from Draper Laboratory and the Massachusetts Eye and Ear Institute developed a head-mount reciprocating delivery system for direct intracochlear delivery in guinea pigs utilizing conventional machining and UV laser cutting [13], [35]. The system works based on infusion and withdrawal of the drug through the cochlear perilymph. Although it includes a micropump and a drug reservoir, it is too large for implantation, even in the guinea pig. Microelectromechanical system technologies (MEMS) have also been used for fabrication of drug delivery microsystems [36]. In 2016, we reported the development of a miniaturized planar MEMS-based peristaltic micropump for nanoliter cochlear perfusion [37]. However, the device had to overcome significant microfluidic interconnection challenges [38] to allow integration of sub-mm scale in-plane microcatheter tubing without adding significant micropump volume.

In addition to microfluidic interconnect challenges, incorporation of control electronics to MEMS-based micropumps can be accomplished either through expensive application specific integrated circuits integrated on-chip, or via a separate PCBA that adds significant bulk to the assembled system. Scaling of MEMS-based systems also requires modification

of the fabrication processes and masks, creating challenges for scalability to human clinical translation.

Here we present a novel miniaturized, wirelessly controlled, fully implantable, and scalable peristaltic micropump that provides programmable and accurate drug delivery for inner ear applications. The actuation force of the micropump is provided by expansion/shrinkage of a thermally phase-change material due to its melting/crystallization. The micropump uses 3D-printing technology and is built directly on the backside of a PCBA around microcatheter tubing (OD=250 μm, ID=125 μm) to integrate the mechanical and control electronic components. The flow path is leak-free and biocompatible and is free of complex microfluidic interconnects. The results of our *in vitro* characterization indicated that the micropump provided nanoliter control of flow rates against ten times greater than physiological backpressures. The *in vivo* mouse model system results indicate functional round window membrane (RWM) drug delivery. Biocompatibility was explored using *in vitro* and *in vivo* experiments.

3.2 System overview and concept

The surface area of the microsystem is intended to go as small as electronic components allow, while the thickness is planned to be smaller than 4 mm, which is approximately half of the commercially available implantable micropump [147]. The commercially available programmable, implantable micropump has an overall volume of $24.8 \times 15 \times 7.2$ mm^3, while the microtubing diameter is 1.5 mm. Pump rate and backpressure requirements were

taken from those used in the literature. Mouse cochlea implantation has been done via a basal turn cochleostomy or canalostomy at flow rates of 16, 32, and 50 nL/min [8], [25], [185]. Inamoto et al. reported a 0.33 kPa to 0.53 kPa for endolymphatic pressure in guinea pigs, which is considered as an estimate for the mouse cochlear backpressure, since there is no measurement for mice [186].

At a minimum, therefore, the micropump needs to provide a maximum flow rate of 50 nL/min in presence of 0.53 kPa backpressure plus the pressure drop in the fluidic system. The micropump chamber dimensions were designed for low-flow rate pumping (10 - 60 nL/min) against backpressure of 5 kPa to have a safe margin for inner ear delivery while enabling pumping for other biological systems.

Drug delivery systems implantation require low operating voltage to protect the animal in case of failure of the insulation. Cazorla et al. suggested 24 V as the maximum allowed voltage for an implantable system [72]. Further, for implantable, programmable microsystem wireless controlling and programming is preferred. Therefore, the micropump is designed to be able to communicate with an Android device using an antenna in the range of 1 foot. Having this range, the system can be controlled and programmed from outside of a mouse cage. Table 3.1 lists the design targets that will enable the creation of this micropump. Figure 3.1 shows a conceptual drawing of the implantation of the subcutaneous microsystem in the mice.

Table 3.1. Targets for implantable microsystem design for inner drug delivery

Characteristic	Design target
Form factor	Planar
Thickness	<= 4 mm
Flow rate	10 – 60 nL /min
Backpressure	5 kPa
Maximum voltage	24 V
Wireless communication range	1 foot
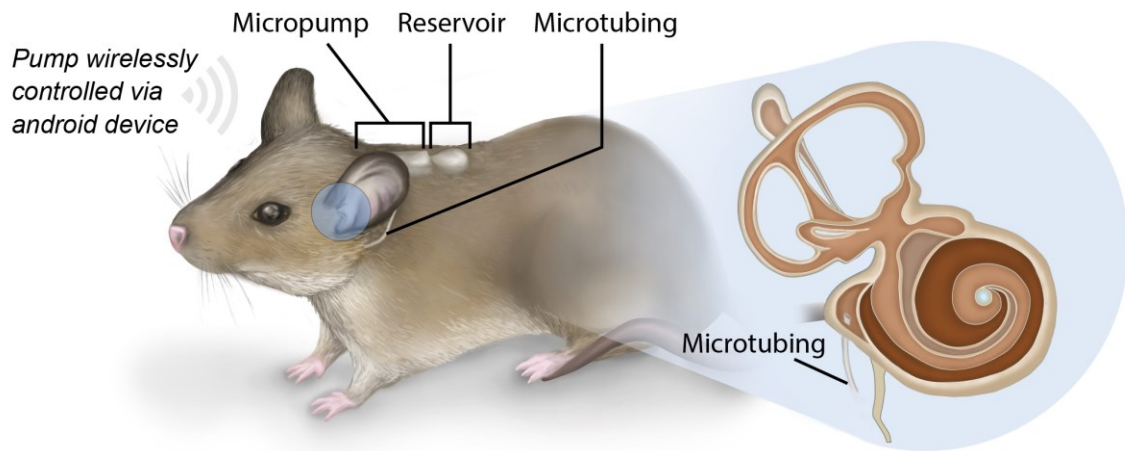
Figure 3.1. A conceptual drawing of the implantation of the subcutaneous microsystem in the mice.

Using a sub-millimeter microcatheter tubing as the fluid-carrying component limits the options for pumping approaches. Methods that require the use of in-line rectifying valves result in bulk that is unacceptable for size-constrained applications. We used peristalsis with the microcatheter tubing sequentially compressed in three locations to induce directional flow. Peristaltic micropumps that use a single tube are one the most reliable mechanisms for drug delivery because one medium is in direct contact with the working

fluid (drug) and no valves or moving components are in the flow channel, which eliminates contamination, leakage, and dead volumes, and reduces clogging and bubble generation. They also benefit from typical advantages of peristaltic micropumps such as resistance to high backpressure [77], [78], [187], bubble tolerance, endurance [79], and self-priming and bi-directional flow capability [78].

Different actuation schemes (e.g., piezoelectric [72], [104], [188], pneumatic [100], thermopneumatic [189], electrostatic [165], and phase-change [37]) are used for peristaltic micropumps. In this study, a novel phase-change actuation method has been used due to its low driving voltage, significant displacement, small size, and high actuation force enabling effective pumping against backpressure. The actuation material was encapsulated in the body of the micropump surrounded by stiff structures except for one side that is exposed to the deformable microcatheter tubing. Peristalsis occurred as a consequence of sequential melting and solidification and associated expansion and shrinking of the phase-change material which drove cyclic compression and release of the microcatheter tubing. Various phase-change materials can be used for actuating micropumps (e.g., gallium [37] and paraffin wax [190]). Paraffin wax was used as the actuation material, due to its stable phase-change behavior and high-pressure actuation [191]. In addition, the paraffin wax melting point can be chosen for a desired application by selecting the appropriate molecular weight of the wax.

The micropump was built directly on the back of a printed circuit board (PCB) employing 3D-printing technology. Three pairs of resistive heaters and thermistors were placed on the PCB to make a linear template for three chambers and a groove between them for the

microcatheter tubing. The three chambers were fabricated in the designated linear pattern adjacent to the microcatheter tubing and were separated by 1.2 mm. Paraffin wax was precisely deposited in the chambers. A peristaltic sequence was applied to the micropump, with a timing control ensuring two closed chambers at each moment. The chambers closed in a sequence of 1 and 3, 1 and 2, and 2 and 3, which pumped the fluid from left to right. Figure 3.2 shows schematic views of the actuation mechanism and the micropump.
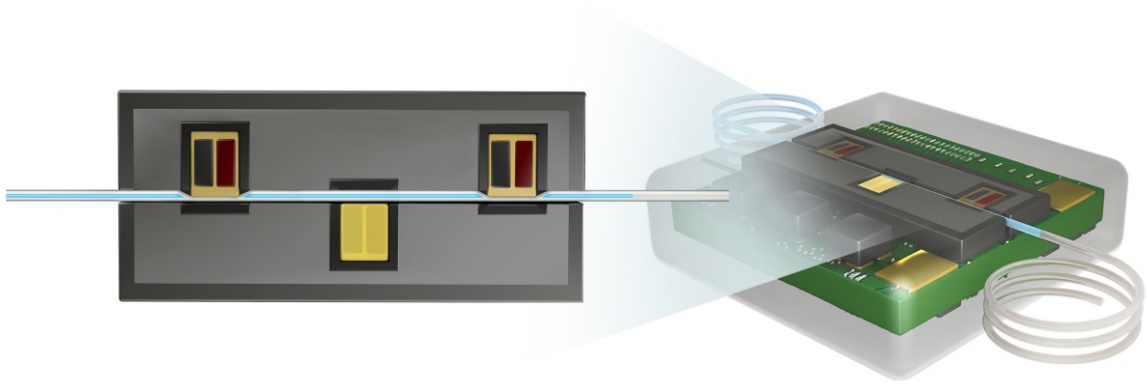
Figure 3.2. Left) Cyclic phase-change actuation of the three chambers compressed the microcatheter tubing and drove peristalsis. The left and right actuators are in the liquid state, compressing the tubing to eject fluid. Right) Schematic of the peristaltic micropump built around a commercially available microcatheter directly on the back of a PCBA using 3D-printing technology.

3.3 Electronic control

3.3.1 Electronic design

The control electronics for actuation and control were fabricated on the front of the four-layer PCB. Off-the-shelf components were used for the micropump control electronics, which were designed for ultra-low-power operation. A rechargeable lithium polymer battery provided power to the system. A step-down buck converter (TPS62743, Texas Instruments) was chosen to provide sufficient current output (300 mA maximum) during pumping, a high efficiency (up to 90% at 10 μA load), and low quiescent current (360 nA) when the system is in shutdown mode. Each pump chamber included a thermistor and a 40-ohm resistive heating element with a discrete N-type metal-oxide-semiconductor for controlling temperature. A 1.8-V power rail was used for the entire system to optimize the power consumption of the wireless microcontroller.

The system on a chip (CC2640, Texas Instruments) included an integrated Bluetooth low energy transceiver (BLE 4.2), a 32-bit ARM Cortex-M3 processor with an up to 48 MHz clock speed, and an ultralow-power sensor controller. This system was chosen for its shutdown current of 100 nA since the system will spend the majority of time in deep sleep mode when the pump is not actively delivering drugs. The system's real time clock used a 32-kHz oscillator (SiT1532, SiTime) based on silicon MEMS technology; it had the smallest footprint and lowest power consumption of commercially available oscillators. A

wire antenna with a length of 10 mm was chosen to keep the overall device footprint as small as possible. The control electronics were configured and operated using a custom Android application via BLE. Figure 3.3 shows an image and the block diagram of the fabricated electronics.
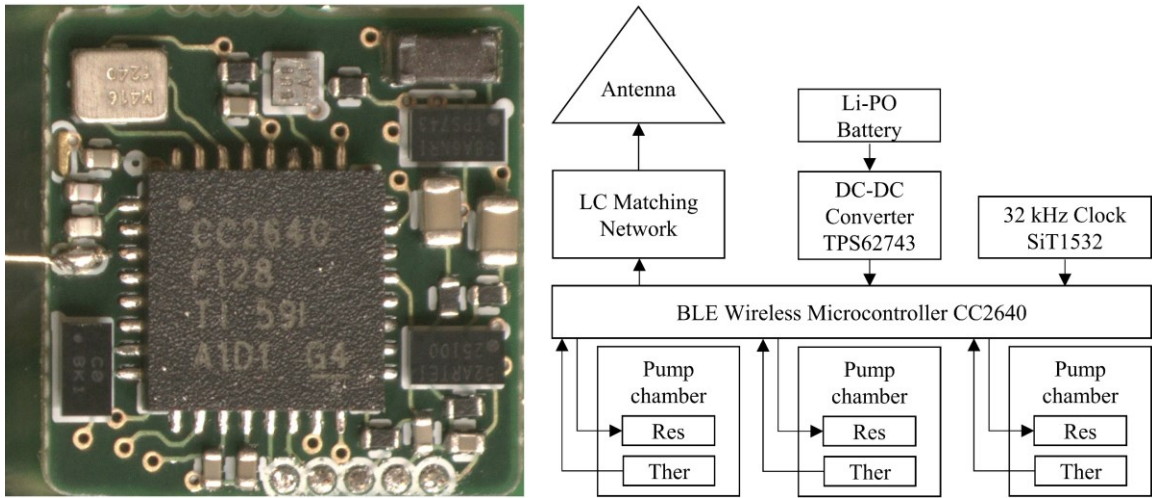
Figure 3.3. Left) Image of the fabricated electronics on front side of the printed circuit board. The electronics assembly was used for actuation, closed-loop feedback to control chamber temperatures, and wireless control. Right) Block diagram of the pump control electronics. Res, resistive heater; Ther, thermistor.

3.3.2 Android application

An Android application has been designed to connect to the micropump to provide on-line control over the flow rate and sequence. After opening the application (i.e., pump controller), it starts to scan for 'NIH Pump.' If the pump is on, it finds the pump, showing the unique pump ID at the left along with RSSI value Figure 3.4. RSSI is a measure of signal strength, with a negative value in 'dBm' in a range of -50 to -100. If the signal is stronger the RSSI value is closer to -50.
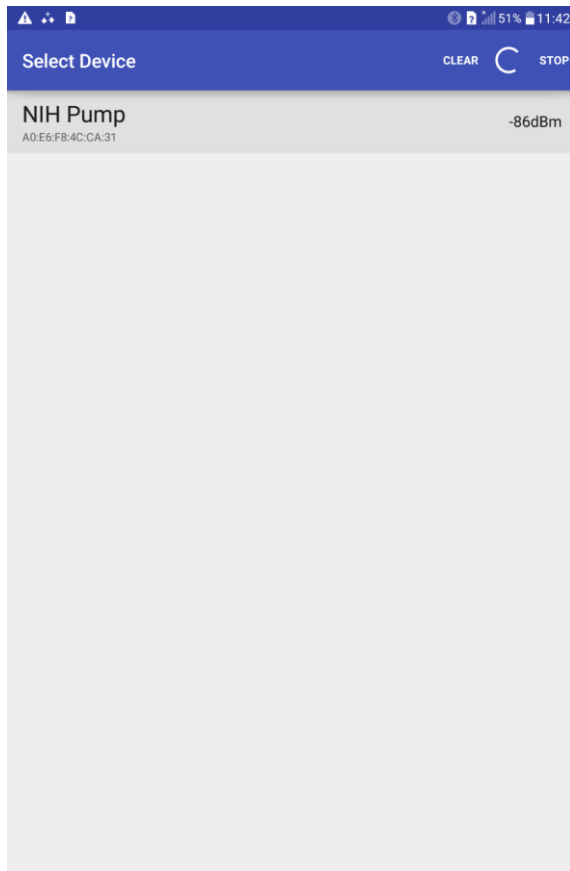
Figure 3.4. Once starting the application, it starts to look for micropumps around. If the pump is on the application finds it and shows the pump's unique ID at the left and RSSI number at the right side of the screen.

After connecting, the screen shows 'connected' if the pump is still connected. It also shows battery supply voltage as 'VBATT' and RSSI number. Further, there are 'start pumping' and 'start recording' buttons for activating/deactivating of the pump and saving the reported data in the tablet. The 'update temperature' button provides the chamber temperature at the moment. These values are based on thermistor reported temperature.
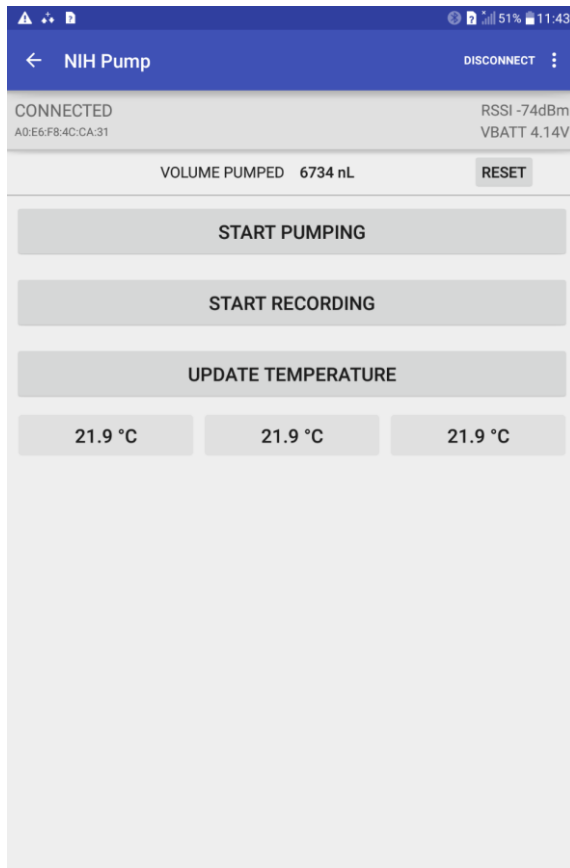
Figure 3.5. The main screen of the application for the micropump. Along with RSSI and ID number the available battery voltage is shown. Also, the 'start pumping' starts/stops the micropump and the 'start recording' saves the data in a '.txt' file. The 'update temperature' button shows the current temperature.

Before using the micropump, the thermistors need to be calibrated, using the vertical '…' button on top right. The 'low temp' and 'high temp' need to be in a range of 10-15 °C and assigned based on a temperature that is read from an external gold standard thermometer (Figure 3.6). While the calibration is linear, valid and accurate within the small imported range, it is not quite reliable off the range.

76
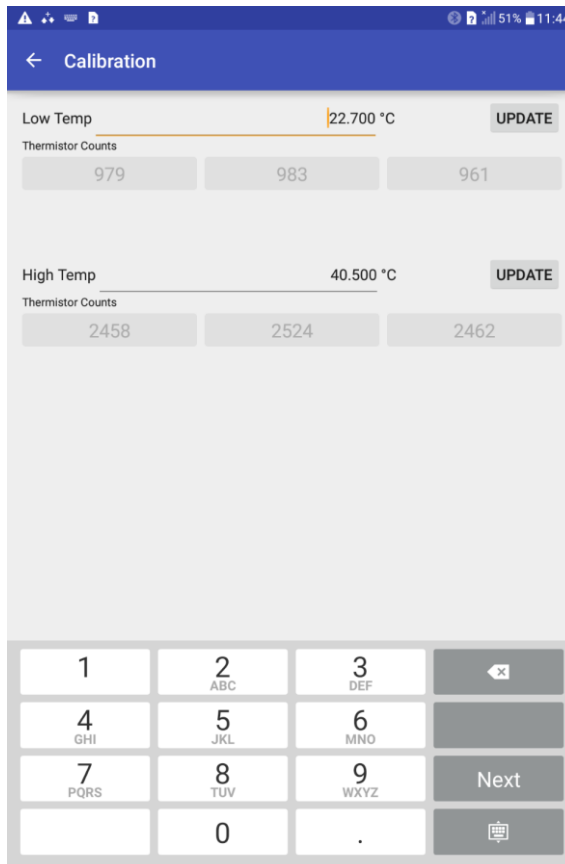
Figure 3.6. The micropump is calibrated with 'low temp' and 'high temp' linearly, based an external gold standard.

To program the pump, 'configure' button should be pushed after using vertical '…' button.

Then in the 'program' section 'edit' should be chosen (Figure 3.7 left). A new screen

displays having options for setting three fields for three chambers for the set temperature

(Figure 3.7 right). For time-related applications, which is the one we are interested in, in

the 'condition' row 'time' should be chosen, and in the 'time' row the desired activation

time of each sequence should be filled in. Multiple sequences can be assigned to the pump

by choosing 'add after' button.
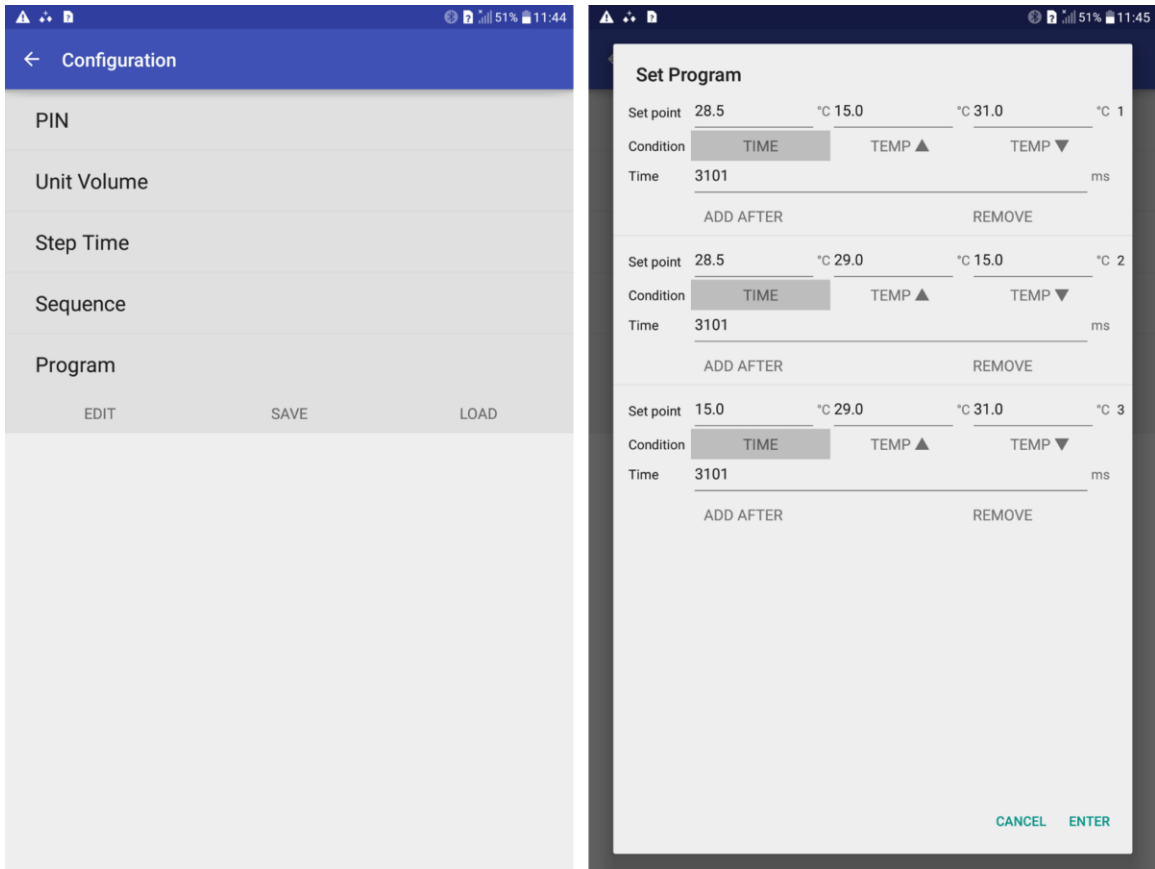
Figure 3.7. Left) the micropump can be programmed in the 'configure' section (not shown in this figure) and by choosing 'edit' under 'program'. Right) Each chamber can be set to the desired temperature (preferably in calibration range) for a specific time at each sequence. The pump can have multiple sequences using 'add after' button.

3.4 Heat transfer analysis

Thermal actuation with phase change materials requires effective transfer of heat in and out of the medium. Heat transfer rates limit actuation frequency and flow rate and affect power consumption. To optimize the micropump system design, a 3D heat transfer model was developed in COMSOL Multiphysics®. In these simulations, the wax remains solid with phase change modeled via changes in heat capacity in the melting temperature range, a common simplification for wax phase change analysis [192], [193]. The four copper layers, copper paths, PCB, resistors, thermistors, wax, and resin that covered the entire system were the elements that most affected the system heat transfer properties. The geometric details of these elements were designed using SolidWorks® and imported into COMSOL Multiphysics®.

A user-defined function (UDF) was used to model the phase-change phenomenon based on the apparent heat capacity method. In this UDF, the phase-change energy of the wax was spread over the phase-change temperature range of 4 °C [194], [195]. This model analyzed the thermal behavior of the system based on material properties, geometry, the difference between the wax melting point and the ambient temperature, and ambient heat transfer characteristics. This generic model can be used for various ambient temperatures and selected wax molecular weights (ie. melting point) to evaluate and optimize pump performance. To present generalized results, all temperatures were presented relative to the ambient temperature.

The material properties of the different elements were considered using the COMSOL library and material datasheets. Since the micropump is going be implanted under the skin, which is a moist environment, it was tested in the laboratory in a petri-dish full of water. Therefore, water was considered as the material surrounding the micropump in the numerical simulation with a free convection boundary condition applied at the micropump external surfaces. Since the water is still in the petri-dish, a free convection boundary condition was applied on the micropump external surface. A UDF enabled sequential heating of the resistive heaters in the chambers based on the desired actuation frequency. The wax temperature was fixed at the set temperature using a UDF for the heat generator to apply a closed-loop on-off controller based on the temperature reported by the thermistor. This simulated micropump heat generation and feedback control.

The results of the heat transfer analysis were first validated using a micropump model. To achieve the maximum target flow rate of 100 nL/min high actuation frequencies were required. Therefore, the design and phase-change material optimizations were i) a minimum of 10°C differential between the wax melting point and the ambient temperature, and ii) reduction from 36 µm (1 oz) to 18 µm (0.5 oz) of the thickness of the copper in the PCB. This thickness reduction increased the actuation frequency by 55% due to reduced thermal mass and heat transfer away from the chamber. The thickness reduction however is limited to PCB manufacturing. Most PCB fabrication companies do not provide thicknesses smaller than 36 µm and 18 µm for the external and internal layers, respectively. Further, the addition of a copper pad to the bottom of each chamber improved the

homogeneity of the chamber temperature distribution, reducing the standard deviation by 35%. Improving homogeneity of the temperature in the chamber enables well-distributed melting of the wax, which avoids local tensions to the chamber structure, especially on the microtubing interface. Details of model validation, geometry, material properties, boundary conditions, and geometry optimization can be found in Appendix A.

The ability of the system to operate at the required frequencies and the insulation between the chambers were studied using the model with the optimized material and geometry. Figure 3.8A shows the simulated temperature elevations when applying 0.33 Hz actuation signals, which theoretically can provide the target flow rate of 100 nL/min. Six pumping cycles were simulated, and the results indicated that the chamber temperatures could fluctuate between the wax melting point and 5 °C lower, which allowed the wax to melt and solidify during each cycle without thermal saturation. A steady state simulation with chambers 1 and 3 on and chamber 2 off simulates worst case scenario for insulation between chambers. The results indicated that the chambers were well-insulated (Figure 3.8B); while two side chambers were set at the melting point, the middle chamber maintained a temperature approximately 9 °C cooler than the melting point.

A crucial characteristic for implantable devices is that the surface temperature should not exceed 2°C above ambient temperature. The results of the sixth cycle of a 1-Hz transient simulations were examined to estimate temperature increases in the micropump exterior surface. It was found that the micropump surface temperature was never > 0.3 °C higher than the ambient temperature, due to small power dissipation of the device.
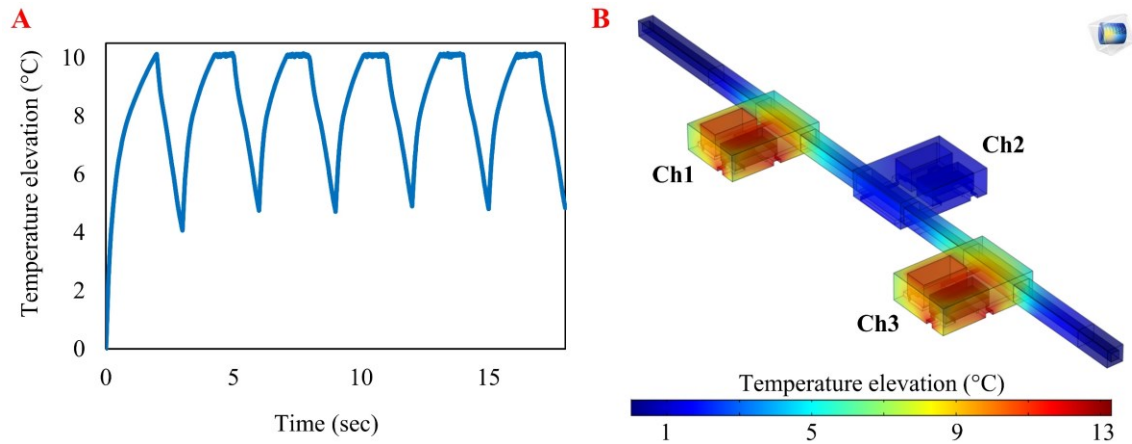
Figure 3.8. Heat transfer analysis of optimized micropump design demonstrated temperature prediction and control. A) The temperature elevation of chamber 1 during the 0.33 Hz actuation, which is sufficient to provide target flow rate of 100 nL/min. The chamber temperatures could fluctuate between the wax melting point (in this case, Nonadecane with melting of ~32 °C) and 5°C lower, which allowed the wax to melt and solidify during each cycle. This simulation shows the micropump can work at this frequency without thermal saturation. B) The design provided effective thermal insulation between the chambers. During a steady state simulation, the temperatures of chambers 1 and 3 were set at the melting point and the chamber 2 temperature remained at approximately 9°C cooler than the melting point.

3.5 Fabrication process

A new fabrication process was developed using 3D-printing technology. The mechanical structure of the micropump was direct-write printed on the back of a PCBA. The control electronics were populated on the front side using standard PCB assembly technology. Three pairs of thermistors and resistors were assembled on the back of the board in a linear offset formation to accommodate subsequent placement of the microcatheter tubing. The micropump structure was 3D-printed using a polymer inkjet printer (Roland VersaUV LEF-12, Tokyo, Japan) and an ECO-UV® resin; three chambers were placed around the resistor/thermistor pairs and a groove for the microcatheter tubing was created.

The pattern of the chambers and the groove for the microtubing (300 μm width) were designed in Solidworks® and converted to .EPS format using Adobe Illustrator®. The chamber width is 1 mm, which by taking into account the width of resistors and thermistors (300 μm each) and a 100 μm clearance between them, leaves 150 μm on the chamber sides. An alignment jig was 3D-printed to properly place the board on the Roland 3D-printer. Since each layer thickness was measured to be ~7.7 μm, 45 layers of the pattern were 3D-printed to create walls with 350 μm height. The chamber structure is taller than the resistor and thermistor (both 300 μm height), ensuring the wax can be contained.

Polyurethane-based catheter microtubing (ID=125 μm, OD=250 μm; MRE010, Micro-Renathane® Catheter Tubing, Braintree Scientific Inc., MA, USA) was placed, fixed, and sealed in the groove using thick cyanoacrylate resin on chamber sides. A 2.5 mL mixture

83

of 4:1 of Epoxy (301, EPO-TEK®, MA, USA) was mixed, and ~4 µL of it was gently poured outside of the chambers and cured for 2 hrs. The amount of epoxy is enough to leave a small space to the chamber wall top, to avoid wicking of the wax onto the epoxy during wax deposition in the molten state.

Docosane (melting point 42-46 °C, $CH_3(CH_2)_{20}CH_3$; Sigma-Aldrich, USA) is molded in a catheter microtubing (ID=305 µm, OD=635 µm; MRE025, Micro-Renathane® Catheter Tubing, Braintree Scientific Inc., MA, USA). The microtubing was placed on a 0.25-mm graded ruler and cut with a brand-new razor blade and a precise volume of wax inside it was taken apart and placed in each chamber. The volume of the wax is a crucial parameter in pump operation. If the wax is too much it can break the structure, usually by leaking from the interface of microtubing and the chamber. It also needs to be large enough to close the microtubing by 10-15 % expansion [191] due to melting.

Thin cyanoacrylate resin was used to cover and seal the structure and to provide mechanical strength to avoid deformation due to phase-change pressure. Finally, the micropump was encapsulated with an approximately 1-µm-thick layer of Parylene-C using PDS 2010 LABCOATER™ 2 (both Specialty Coating Systems, Indianapolis, IN, USA). The Parylene-C coating provided a biocompatible moisture barrier around the micropump, enabling electrical insulation for the electronics.
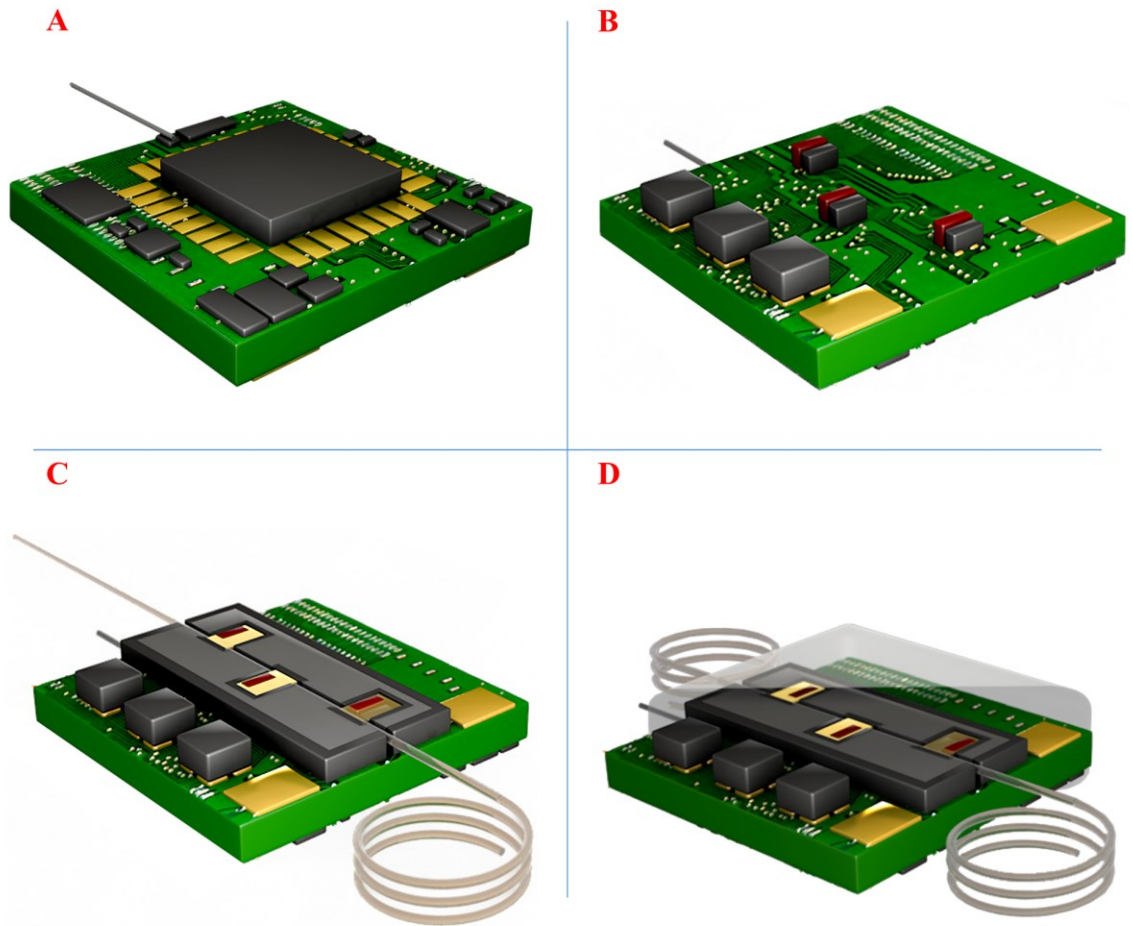
Figure 3.9. Fabrication process of the micropump. A) The electronic components for actuation, temperature control, and wireless communication were assembled on the front side of the PCB. B) The micro-heaters and thermistors were assembled on the backside of the PCB, forming a template for three linear chambers and a catheter microtubing. C) A commercially available catheter microtubing (250µm OD, 125µm ID) was placed within a printed template. A precise volume of wax was placed in each chamber in contact with the microtubing and integrated micro-heater and thermistor. D) The chambers were covered with a rigid resin.

3.6 In vitro characterization

The micropump was first characterized using *in vitro* experiments. Flow rate measurements were taken at different actuation frequencies, backpressures, and ambient temperature variations. The actuation temperature of each chamber was calibrated across the range of actuation frequencies and ambient temperatures. The micropump was submerged in deionized (DI) water in a petri dish to simulate the thermal characteristics of the pump after implantation. Nanofittings (Idex©, WA, USA) were used to connect the tubing to a Luer Lock syringe. The micropumps were specifically designed for room temperature operation.

The micropump was powered by a 3.7 V rechargeable Li-ion battery and was programmed by an Android application. Dyed DI water was used as the working fluid to provide visual observation of the fluid displacement in the microcatheter. The fluidic system was filled and visually inspected for no trapped air. The downstream microtubing was placed on a ruler with the flow rate measured by calculating fluid front advancement in the 125 μm ID microcatheter.

3.7 In vivo experiment

An *in vivo* test of the system was performed using a paradigm that induces temporary hearing loss via administration of sodium salicylate following a protocol developed at our laboratory [25]. Salicylate causes reversible disruption of outer hair cell motility because

it can act as a competitive antagonist at the anion-binding site of prestin [196]. Disruption of prestin reduces the magnitude of otoacoustic emissions [197] and can result in reduced distortion product (DP) amplitudes and reversible elevation of distortion product otoacoustic emission (DPOAE) thresholds. Thus, salicylate was delivered to the RWM and auditory function was assessed using DPOAE methodology.

3.7.1 Drug infusion system and solutions

The salicylate solution consisted of NaCl (120 mM), KCl (3.5 mM), CaCl2 (1.5 mM), glucose (5.5 mM), HEPES buffer (4-(2-hydroxyethyl)-1-piperazineethanesulfonic acid, 20 mM), and sodium salicylate (50 mM). The pH was adjusted to 7.5 using NaOH. All solutions were prepared on the day of the experiment using sterile double-distilled water. The salicylate was loaded into a 3-cc sterilized syringe and was debubbled. Using positive pressure, the salicylate was pushed until it was 1 mm from the tip of the tubing and then the micropump was placed on the same level as the mouse. After each experiment, sterile, double-distilled water, was forced through the tee, fittings, and microcatheter tubing in order to clean the fluidic elements.

3.7.2 Animal and surgical procedures

A total of six young adult (age, 2–4 months) CBA/CaJ mice bred and raised in-house were used for this study. Each animal underwent a bullaostomy surgery to prepare a site for infusion of the salicylate into the middle ear cavity. All animal procedures were approved by the University of South Florida Institutional Animal Care and Use Committee and were performed using National Institutes of Health and veterinary standards of care.

Each animal was deeply anesthetized for the bullaostomy surgery using a mixture of ketamine (120 mg/kg body weight) and xylazine (10 mg/kg body weight) injected via the intraperitoneal route. The left ventral surface of the neck was then shaved and cleaned. The animal was positioned on its back on a heated operative plane maintaining aseptic conditions.

Surgery was performed on the left (ipsilateral) ear following procedures performed by Borkholder *et al.* [25]. Briefly, the tympanic bulla was exposed using a ventral approach, and an incision was made in a longitudinal direction along the ventral surface of the neck to expose the bulla. A 300-µm diameter carbide micro drill bit modified to include insertion stops was used to bore a bullaostomy at a location approximately 1.5 mm laterally below the stapedial artery [14]. Using a micromanipulator (MM3–3, World Precision Instruments, Sarasota, FL), a fine metal probe was attached to the polyimide infusion tubing using adhesive (3M Repositionable 75 spray adhesive, St. Paul, MN). The infusion tubing assembly was inserted into the bullaostomy to a depth of approximately 300–500 µm, near the opening of the round window. Medical grade adhesive (Loctite 4206, Rocky

Hill, CT) was used to temporarily secure the infusion tubing to the bulla opening. Subsequent application of dental cement (3M ESPE Duralon) provided a more permanent and robust bond and sealed the cannula to the bullaostomy site. The surgery site was loosely sutured closed to provide strain relief for the infusion tubing. During infusions, each mouse was immobilized using anesthesia as described in this section. Supplementary doses at one-third of the initial dose were administered as needed to maintain the proper levels of general anesthesia. After each infusion, the pump was stopped, and anesthesia was maintained for an additional 40 min while additional auditory assessment data were recorded.

3.7.3 Auditory function assessment

To non-invasively assess the auditory function, the DPOAE method was employed which serve as a monitor of outer hair cells. The mechanical response of the outer hair cell causes an acoustic signal propagated back out through the auditory canal, which correspond to discrete frequencies and can be measured to non-invasively assess cochlear function [2]. This method has been vastly used in newborns and children hearing screening and scientific investigations [198]. Cochlea generates DPOAE when the ear is exposed to two simultaneous pure tones (F1 and F2), where the F2/F1 frequency ratio typically varies between 1.1 and 1.3 to generate intermodulation DPOAE component. The corresponding amplitudes for these tones are assigned as L1 and L2, where the lower tone is usually the F1. As a consequence of intermodulation the cochlea generates *distortion products*, which are long series of components that are not present in the input stimuli. The most common

distortion products in clinical practice and animal experiments is the *cubic difference distortion product*, denoted as 2F1-F2. The DPOAE protocol that uses unequal primary intensities (L1 > L2,) is called *asymmetrical*, which is used in this study. Using this protocol the intermodulation components are close to F2, which is why the DPOAE information is referenced to F2. One of the ways to present the DPOAE information is the *DP-gram* modality, where the 2F1-F2 amplitudes are measured at various F2 frequencies, with fixed stimulus intensities [199]. Although DPOAE is an effective non-invasive method for hearing assessment, there can be errors in the measurements due to calibration error, misplacement of the probe, object motion. In case of animal studies, the level of anesthesia should be enough that the animal does not wake up during the measurement.

The auditory function measures were the same as we previously reported [200]. Each mouse was anesthetized as described in section 3.7.3. Supplementary doses of anesthetic were administered as needed. Auditory function was assessed via automated DPOAE threshold measurements at F2 frequencies of 8.9 kHz, 13.5 kHz, 17.9 kHz, 24.6 kHz, 35.8 kHz, and 51.4 kHz. Measurements performed before surgery were used for a baseline to compare subsequent DPOAE threshold shifts.

Stimuli (F1 and F2) were generated using Tucker Davis hardware (TDT; Alachua, FL) controlled via ActiveX from a custom Matlab r13 (Mathworks; Natick, MA) graphical user interface. A Tucker Davis RP2.1 processor at a sample rate of 200 kHz was used to generate the sound stimuli and acquire the signals. All acoustic signals were emitted through electrostatic speakers (TDT EC1) connected to a probe via 4-cm tubes. The probe contained an ER10B+ microphone (Etymotic; Elk Grove Village, IL). Waveforms from

each presentation were windowed using a Hamming window, and high-resolution 390625-point fast Fourier transforms (FFTs) (2× sample rate) were calculated. The resulting FFTs had a bin size of 0.5 Hz, which allowed for accurate measurement of signal level as a function of frequency. Frequency-domain averaging was used to minimize artifacts. Before subsequent analysis, the mean FFT values for multiple repetitions of the same stimulus were calculated. The probe microphone was calibrated relative to a 0.25" B&K microphone (Type 4938, Bruel & Kjaer; Naerum, Denmark) using a 0.1 cc coupler (simulating the mouse ear canal).

DPOAE amplitudes were measured by generating F1 and F2 primaries at 65 and 50 dB SPLs, respectively (ratio of the two frequencies = 1.25). The output waveforms of the ER10B+ probe microphone were input to a TDT RP2.1 processor. The FFT values for each presentation were averaged and signal levels at five frequencies were sampled (F1, F2, DP (2F1-F2), as well as two noise bins above and below the DP frequency). After FFT sampling, the dBV was converted to SPL based on the ER10B+ microphone calibration. DPOAE thresholds were defined as the F1 level required to produce a DP of 0 dB SPL (+/−1 dB). We developed an automatic threshold search algorithm implemented in Matlab r13 using TDT hardware and the Etymotic ER10B+ probe microphone.

3.8 In vitro results and discussion

The completed micropump is illustrated in Figure 3.10A. The overall pump size is $8 \times 8 \times 3$ mm^3 (L $\times$ W $\times$ H). *In vitro* experiments were performed to assess the capacity of the micropump to provide required flow rates for inner ear drug delivery in the presence of physiological backpressure. The consistency of the micropump to provide a 50 nL/min delivery flow rate during a 20-min period was also examined. This flow rate was required for the *in vivo* experiments. Finally, the micropump performance was tested at different ambient temperature conditions because after subcutaneous implantation the micropump may be exposed to variations in ambient temperature. *In vivo* experiments test three micropumps in six mice with the microcatheter tubing implanted at the RWM niche delivering salicylate at 50 nL/min for 20 min, replicating a previous drug delivery system utilizing syringe pump instead of micropumps [25]. Auditory function was assessed using the DPOAE method.

3.8.1 Micropump performance characterization at physiological backpressures

Flow rates were measured at actuation frequencies from 0.015 Hz to 0.21 Hz (i.e., 0.015 Hz, 0.05 Hz, 0.1 Hz, 0.15 Hz, 0.21 Hz) to provide 10-100 nL/min, which covers two times above the maximum reported drug delivery infusion flow rate [8], [25], [29], [185]. The

backpressures were 0 and 5 kPa, which covered one order of magnitude larger than the endolymphatic physiological backpressures of 0.33–0.53 kPa in the guinea pig [186] (no measurements were available for the mice). The results (Figure 3.10B) indicated that the micropump can provide almost linear results ($R^2 = 0.98$) through the 10–100 nL/min range, suggesting wax melting / crystallization kinetics are not a limiting factor in micropump performance across the actuation frequencies explored. The results also indicated that applying 5 kPa backpressure did not significantly affect the flow rate. Further, a pulsatile flow was observed; actuation of each chamber causes a forward pulse, while filling/loading of chamber 3 results in a backward flow. This can reduce pump efficiency.

3.8.2 Pump performance at different ambient temperatures

Pump performance was characterized at different ambient temperatures to evaluate functionality after implantation, considering the possible variation in the body temperature and ambient temperature. The experiments were performed at 0.015 Hz, 0.1 Hz, and 0.21 Hz actuation frequencies, which represented the minimum, middle, and maximum frequencies, respectively. The ambient temperature was changed to T_{amb}-3, T_{amb}, and T_{amb}+3 to assess the functionality of the micropump at a ±3˚C variation from the ambient temperature. The results indicated that the ambient temperature had a minor effect on the micropump flow rate (i.e., < 5% change) (Figure 3.10C).

3.8.3 Pump assessment for in vivo acute experiment

The micropump was set to provide 50 nL/min for 20 min to assess its capacity for replicating the acute *in vivo* experiment. In the acute *in vivo* experiment the micropump was tested using a mouse model system inner ear drug delivery paradigm [25] in which salicylate was delivered to the RWM niche for 20 min at 50 nL/min using a syringe pump. To test the capacity of the micropump to replicate the same experiment, it was set to provide 50 nL/min for 20 min. The results (Figure 3.10D) indicated that the micropump provided an average flow rate of 50.2 nL/min (standard deviation = 0.96 nL/min). The flow rate fluctuation was approximately ±2%, and 1,004 nL drug was delivered over the 20 min period (0.4% error).

3.8.4 Flow rate resolution

Characterization of micropump resolution at different flow rates included the entire suggested range of 10–100 nL/min. Experiments were performed at 10, 50, and 100 nL/min to test the minimum, *in vivo* infusion, and maximum flow rates, respectively (Figure 3.10E). For the 10 nL/min rate, the actuation frequencies were changed by 0.00075 Hz until the flow rate was statistically different compared with the reference flow rate of 9.94 nL/min. The lowest resolution for this flow rate was 1.24 nL/min. For the 50 and 100 nL/min rates, the actuation frequencies were changed by 0.0025 Hz until the differences were statistically significant. The lowest resolutions for the 50 and 100 nL/min rates were

2.35 and 2.39 nL/min, respectively. Therefore, the worst-case flow rate resolution was 2.39
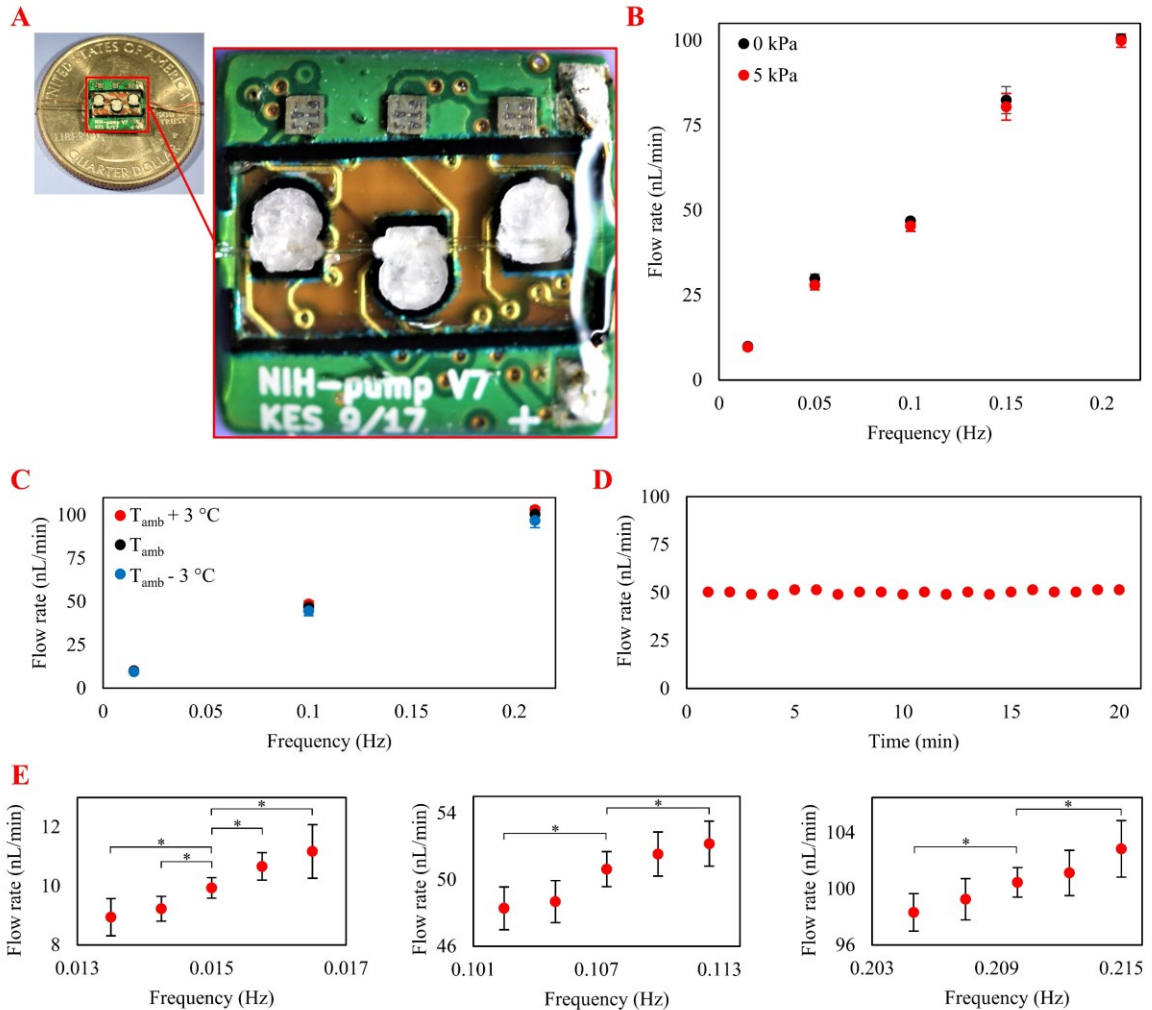
nL/min.

Figure 3.10. A) Photograph of the peristaltic micropump with a commercially available microcatheter and a 3D-printed structure around it on the back of a printed circuit board. B) The pump was characterized at 10–100 nl/min flow rates and 0–5 kPa back pressures optimized for the target intracochlear drug delivery application. Each data point is the mean value of five trials; error bars represent one standard deviation. C) Performance of the pump at 50 nL/min (required for the *in vivo* test) for 20 min indicated precise flow rate control. D) Characterization of micropump resolution at flow rates of 10, 50, and 100 nL/min; the greatest resolution was 2.39 nL/min. Each point is the mean value of five trials; error bars represent one standard deviation. E) Pump performance at different frequencies and ambient temperatures. The variation in flow rate was not statistically significant by changing the ambient temperature by ±3°C. Each point is the mean value of five one-min trials; error bars represent one standard deviation.

3.9 In vivo results and discussion

In vivo experiments were performed using three mice. A cannula connected to the same micropump was placed near the RWM. Figure 3.11 shows the effect of RWM perfusion of sodium salicylate delivered at a 50 nL/min flow rate. The effects on the DPOAE threshold shifts were recorded from three different mice over the course of 20-min. The results for the mean threshold shifts are presented in panel A and compare the changes in DPOAE thresholds to baseline at four time points (i.e., post-surgery (PS) in which DPOAE values were acquired immediately before the pump was turned on, 0 min, the time at which the pump was turned on, and 10 and 20 min following the onset of salicylate perfusion. A baseline measurement was acquired approximately 10–15 min before the cannula placement surgery was performed. There was a systematic increase in threshold shift during the 20-min perfusion; there was a mean shift of 15 dB for the most basal region. In this case, the same pump was used for the three different mice. Panel B presents the results for the period for a mean threshold shift at 51 kHz. The perfusion was stopped at 20 min and DPOAE values were continuously recorded.

Figure 3.12 shows the DP threshold shift for three different pumps implanted in three mice in which sodium salicylate was perfused. The actual threshold shift was referenced to the baseline condition. The time course of the threshold shift or the loss of outer hair cell motility due to dysfunction in prestin was consistent across the three micropumps. The maximum shift was between 15 to 29 dB and was observed in the most basal (51 kHz) cochlear location consistent with salicylate delivery to the RWM niche.
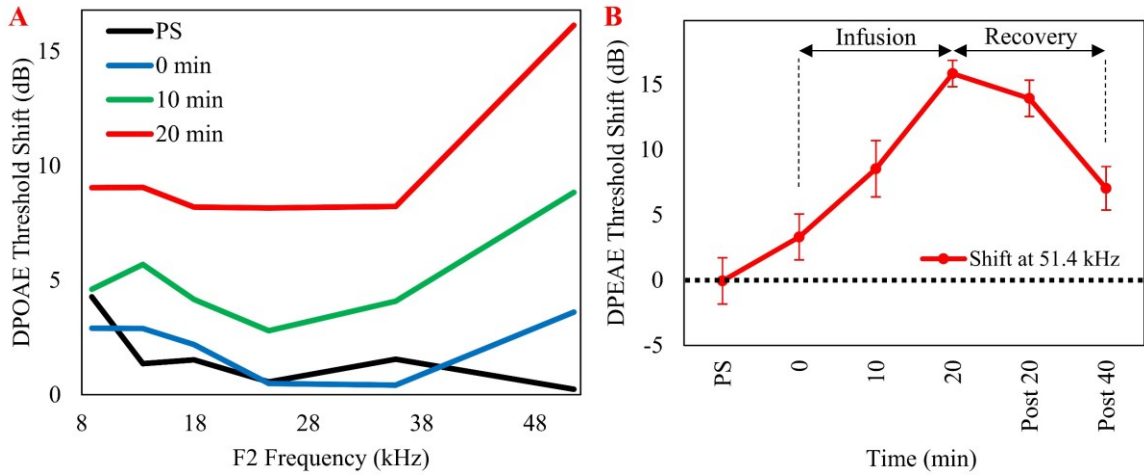
Figure 3.11. *In vivo* intracochlear delivery of sodium salicylate elevated otoacoustic emission thresholds from 8 to 51 kHz in three mice. In each mouse, the cannula was implanted near the round window via a bullaostomy. A) Mean DPOAE threshold shifts from three mice recorded during 20 min after the start of a salicylate infusion. DPOAE thresholds systematically increased as a function of perfusion time from the start of the perfusion (0 min) to 20 min. B) The mean DPOAE threshold shift for the most basal cochlear region, 51 kHz plotted as a function of time following the start of the sodium salicylate infusion. Post 20 and post 40 min denote the measurement times after turning off the pump. PS = post surgery; post 20 = 20 min after stopping infusion; post 40 = 40 min after stopping infusion.
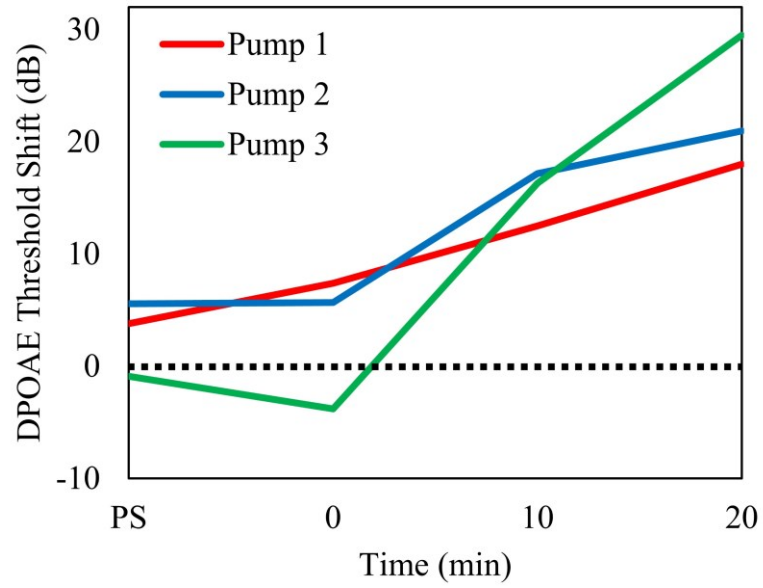
Figure 3.12. DPOAE threshold shift (51 kHz) for the most basal cochlear region, following sodium salicylate infusion, plotted as a function of time for three micropumps. The time points refer to DPOAE acquired at PS-post surgery, 0 min – start of pumping, and 10 and 20 min following the onset of pumping.

3.10 Conclusion

We developed a novel miniature, fully implantable, and scalable phase-change peristaltic micropump with wireless control. The micro- pump was realized using 3D-printing technology to build the mechanical components around catheter microtubing on the back of a PCB. On the front side of the PCB, the electronic components were assembled to actuate and control the micropump, along with enabling wireless control. *In vitro* characterization results indicated the micropump achieved nanoliter-level resolution of delivery in the specified range of 10–100 nL/min in the presence of up to 10× larger than physiological backpressures. Small variations in ambient temperature were found to not significantly affect the results. An *in vivo* experiment was performed by implantation of the catheter microtubing of three different micropumps in the RWM of six mice for delivery of sodium salicylate. The results indicated that the DPOAE response was consistent across different micropumps and different animals. This proof of concept *in vivo* success of our advanced micropump technology used in the mouse (cochlea volume ~ 620 nL) indicates translational opportunities. Using appropriate scaling of the microtubing size and actuator volume, the micropump is inherently scalable for use in larger species and clinical applications in children and adults. Our results indicated that this advanced micropump can provide organ-targeted drug delivery to avoid systemic side effects and maximal control of drug concentration and timing parameters.

Chapter 4   Biocompatibility Of Microsystem

Materials

4.1 Introduction

The biocompatibility experiments on the materials used to make the pump structure and a pump prototype are described in this section. These experiments were done prior to subcutaneous implantation tests. Details of *in vitro* experiments on pump materials along with quantitative results are presented. Finally, qualitative assessment on a pump prototype that was implanted for a long time is demonstrated.

4.2 Materials and methods

Biocompatibility of all materials in contact with the drug or tissue was assessed before chronic subcutaneous implantation tests. The biocompatibility experiments were performed on key micropump components: the micropump tubing, parylene-coated tubing, and Polydimethylsiloxane (PDMS). PDMS will be used for the subcutaneous implantation tests. An early step in this process involved performing a cell growth curve to set a baseline for normal cellular growth. The key micropump components were then added to assess effects on cell health and viability. Biocompatibility of the material was evaluated by comparing the cell viability assay results when using the micropump materials with the control baseline cell growth viability results (i.e., without use of the pump materials).

The first experiment established the health and viability of the control cells. The growth of random samples of human mammary epithelial cells (ATCC-HMEC cell line) was recorded. Each day for 11 days, ten random samples of human mammary epithelial cells were removed from a 75 cm^2 flask. Cell numbers were assessed in a cross-sectional area of 0.5 mm by 0.5 mm, or 700 pixels by 700 pixels, using the cell counter program NIH-ImageJ. Five cross-sectional areas were chosen for each sample (Figure 4.1). The first area was taken from the top left, the second from the top right, the third from the center, the fourth from the bottom left, and the fifth from the bottom right of the photograph (Figure 4.1). The cells that were on the boundaries of the top and left sides of the boxes were counted, and the cells that were on the boundaries of the bottom and right sides of the box were not counted. The results were recorded in a Microsoft Excel spreadsheet, the mean

values for the five cross-sectional areas for each sample were calculated, and the mean results for each day were estimated. The days and mean cell numbers were graphed to display a cell growth curve that showed the growth of the cells over time.
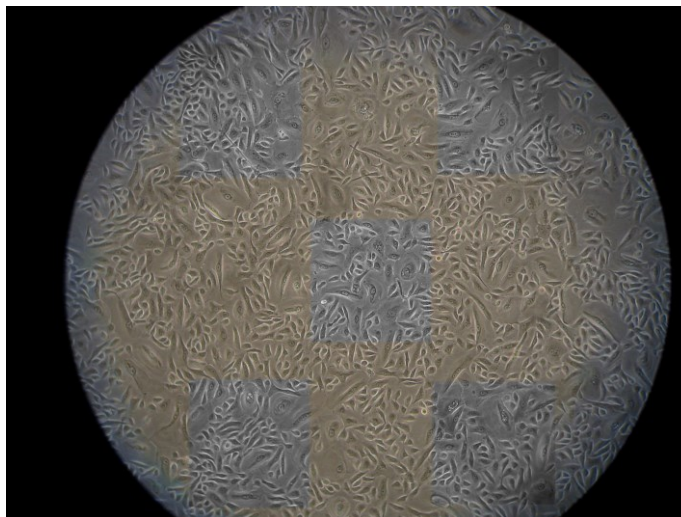
Figure 4.1. One representative sample from the last day of an 11-day cell growth period. The five areas indicating where cells were counted are illustrated. The mean values from five areas were calculated, and then the total cell counts among the 10 samples from Day 11 were averaged to obtain one cell count value for Day 11. Similar analyses were performed on Days 1–10. The data were plotted to obtain the cell growth curves

The second experiment was performed for quantitative assessment of the cell viability of the control cells (no pump parts) versus the cells grown in the presence of key pump components. The cell viability assays used included the XTT, MTT, and BDRU tests of cell health and viability. These *in vitro* assays are a first step towards ISO 10993 biocompatibility tests, which are more involved *in vivo* tests of toxicity, irritation and hemocompatibility. If the *in vitro* assays of the present report show biocompatibility of the pump parts, then the more extensive ISO 10993 tests should be undertaken. The ATCC-HEMC human epidermal epithelial cell line was used for the biocompatibility and viability tests here. The cells were seeded into 96-well culture plates, the groups were set up as non-

treated and treated (e.g., parylene, PDMS, pump tubing, or a combination) groups for 2 or 7 days. Each experiment was repeated three times.

For the MTT assay [201], the cells were seeded in 96-well culture plates and exposed to different conditions. Then, 20 µL MTT (5 mg/mL stock solution) was added to each well, and the plates were incubated at 37 ˚C for 5 hrs. Thereafter, the medium was gently removed from each well, and 200 µl DMSO was added to each well to dissolve the purple formazan crystals. The absorbance at 570 nm wavelength was recorded using the Dynatech MR5000 spectrophotometer (Dynatech Laboratories, Inc., Chantilly, VA).

For the XTT assay [202], the electron coupling solution was added to XTT reagent (1:50 volume ratio) to make an XTT detection solution (Cell Signaling, #9095). Five ml XTT solution and 0.1 ml electron coupling solution were added to each well. Then 50 µL XTT detection solution was added to each well that contained the 100–200 µl/well culture medium and the plate was returned to the incubator. Absorbance at a 450-nm wavelength was recorded. The optimal incubation time for this assay depended on the experimental setup (e.g., cell type, cell number, and treatment). Optimization of incubation time was determined by reading one plate at various time points after addition of the XTT detection solution.

The BRDU-test was performed according to the manufacturer's instructions (Cell Signal kit #6813). Cells were seeded in each well of a 96-well plate, then 100 µL/well Fixing/Denaturing Solution was added to each well. The solution was removed after a 30-min incubation at room temperature. Prepared 1X detection antibody solution (100 µL/well) was then added, and the plate was incubated at room temperature for 1 hr. The

solution was discarded, and the plate was washed three times with the 1× Wash Buffer. Prepared 1× HRP-conjugated secondary antibody solution (100 µL/well) was then added and the plate was incubated at room temperature for 30 min. The solution was removed, and the plate was washed three times with the 1× Wash Buffer. TMB Substrate (100 µL/well) was then added, the plate was incubated for 30 min at room temperature, the STOP Solution (100 µL) was added. Absorbance (450-nm wavelength) was then measured. To obtain the most accurate result, the absorbance was recorded within 30 min after adding the STOP Solution.

4.3 Biocompatibility results

The results of the control cell line growth experiment indicated that the numbers of cells increased each day and cell morphology became more developed over time (Figure 4.2A). The results for the cell growth function for the cell culture used and the predicted theoretical exponential cell growth curve are presented in Figure 4.2B. The close correspondence between the two functions indicated normal, healthy cell growth and healthy and viable cell cultures. Based on the results of the cell growth curve, during the subsequent experiments cell growth was measured on days 2 through 7 because during this period cell growth approached linearity and was the most substantial.

For the second experiment, key pump components were added separately or combined to the cell culture dishes. Cell viability assays were performed on Days 2 and 7. A representative micrograph of a cell culture dish with the tubing placed within the growing cells is presented in Figure 4.2C. The quantitative results for the three-cell health and viability assays, compatible with the ISO 10993 standard tests for implantable medical device biocompatibility, for Day 7 are presented in Figure 4.2D. In each case, the assays were performed with the materials alone as a comparison condition, then with the pump component materials in the cell culture dishes with the growing cells. The control condition (far right bar on the histograms) provided the cell viability measurements for the cells alone (i.e., no pump components in the cell culture dish). The main finding was that there were no statistically significant between-group differences for cell health, biocompatibility and viability for any of the pump component conditions compared with the control condition.

After successful completion of *in vitro* biocompatibility testing of the pump materials, we implanted a subcutaneous prototype pump on the back of a young adult CBA/CaJ mouse (Figure 4.3). The power supply connector was exposed on the top of the skull. The mouse recovered, and no morbidity was observed following the implantation. Post-implantation, the mouse was monitored daily and the results indicated that the overall health was excellent. There were no statistically significant body weight changes; any signs of inflammatory or immune responses, or any indications of infection, such as swelling, redness, fever or presence of discolored fluid. Future studies will examine the tissue surrounding the implanted pump systematically for histological signs of inflammation *in vivo*.
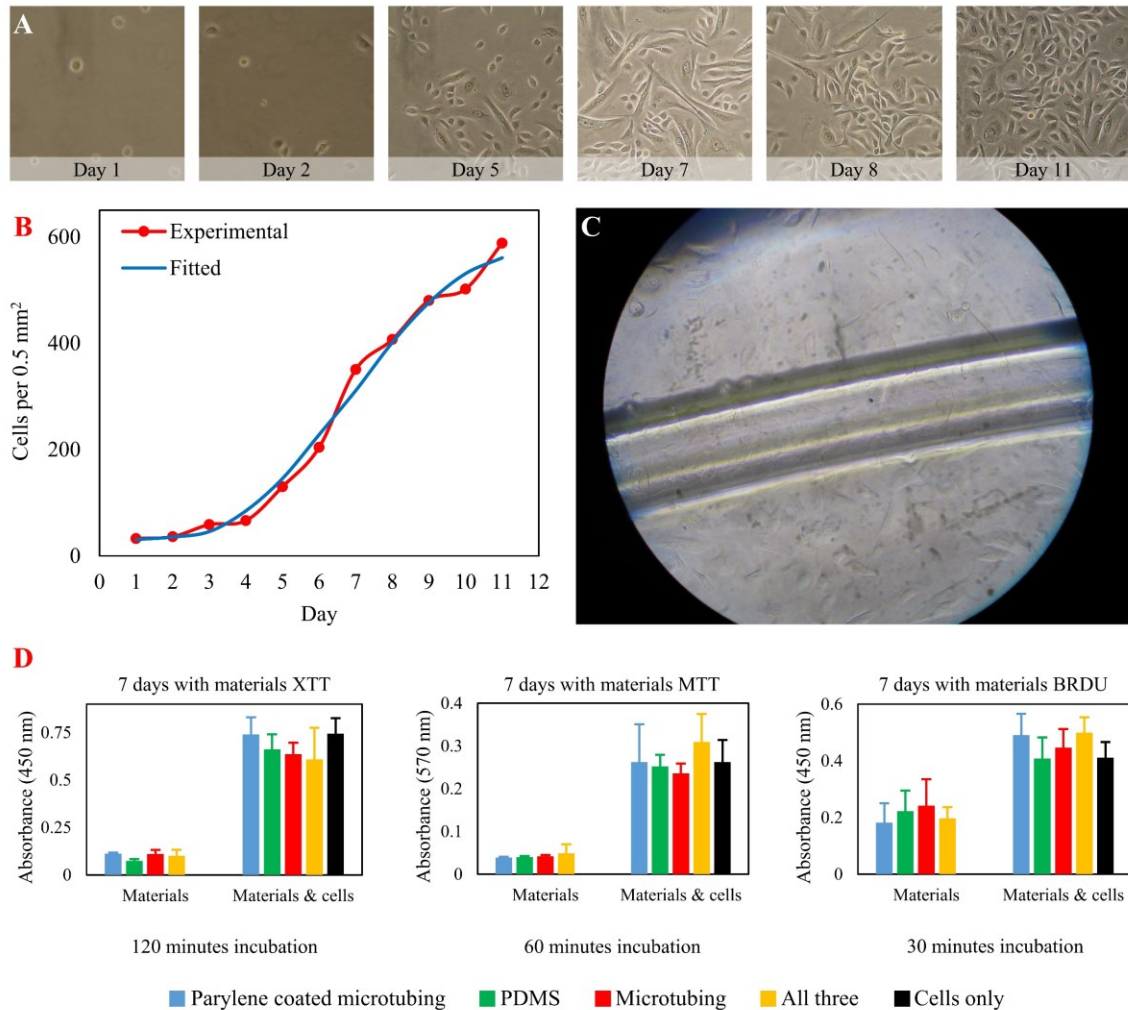
Figure 4.2. A) Micrographs taken from the center of a sample (Section 3 in Figure 4.1) at Day 1, Day 2, Day 5, Day 7, Day 8, and Day 11. The photographs illustrate how the numbers of cells increased each day, and that cell morphology became more developed over time. B) Cell growth curve of the human mammary epithelial cells. The curve was similar to the expected exponential growth curve. This result indicated that the cell line used for the cell viability biocompatibility assays met the healthy growth metrics requirement. The curve followed the trend line (blue line, y= 23.322 e$^{0.3262x}$) exponential curve, residual value = 0.95. C) Micrograph illustrates the polyurethane-based catheter tubing placed in the well containing human mammary epithelial cells. Under experimental biocompatibility conditions, cells were harvested from the regions directly around the tubing and cell viability assays were performed. The results were quantitatively compared to the cells in the control dishes, which were presented in Figure 4.1, Figure 4.2A, and B. D) Histogram results indicate there is no statistically significant difference in the cell health and viability quantitative measurements for the human mammary epithelial cells, with and without the pump components. The "materials" measurements represent a comparison condition where only the components were in the dish, with no cells. Under the "materials & cells" conditions, the components were placed in the cell culture dishes on Day 0; the components were in the dishes as the cell size and number increased over a period of 7 days. The far-right bar on the three histograms is the "Cells only" Control condition (i.e., no pump components were present in the dish during cell growth).

107
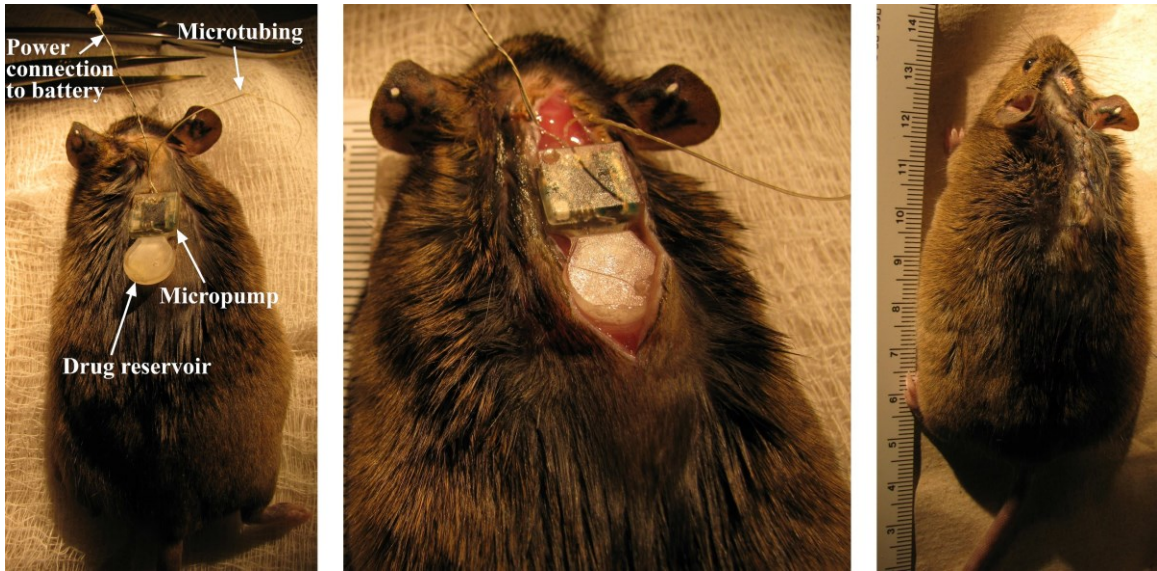
Figure 4.3. Photos showing the system following subcutaneous implantation in a CBA mouse following one month of implantation. Note the lack of inflammation or infection in the skin surrounding the implant area, and the mouse health and behavior was normal.

4.4 Conclusion

Implantability of the micropump was assessed using a biocompatibility evaluation of the micropump components and a system prototype. Our findings showed that the micropump components passed key biocompatibility tests, which indicated that they were suitable for translational applications, including subcutaneous implantation in humans and animal models.

Chapter 5   A Modular Microreservoir For

Active Implantable Drug Delivery

5.1 Introduction

Drug delivery systems have become of interest to researchers in the past decades for improving therapeutic response by providing more consistent blood level compared to immediate release or sustained release parenteral depot, enabling less frequent and more efficient dosing, and improving patient comfort, safety, and compliance. Microscale reservoir-based delivery systems result in miniaturization of the delivery systems while allowing more precise control of the delivery rate for both systemic and site-directed delivery [203]. Specifically, these systems assist site-directed delivery by enabling access to relatively inaccessible sites or a specific tissue type, along with limiting side effects of systemic exposure. Microscale reservoir-based delivery systems can be categorized into

three types: oral, dermal, and implantable delivery, which the latter is the focus of this work.

Implantable microscale reservoir-based drug delivery systems enabled novel and effective drug delivery concepts for both systemic and targeted drug delivery applications[203]. Implantable drug delivery systems have been classified into two categories [36], [204]–[207]: (i) passive, where post-implantation drug release control is not feasible since it is pre-determined by the fabrication methods, materials, and drug formulation, and (ii) active, where post-implantation drug release control is enabled using electrical, mechanical, magnetic or other actuation methods. Passive implantable drug delivery systems are driven by osmotic potential or diffusion. These microsystems were employed in various applications such as ophthalmology [208]–[214], oncology [215]–[217], interventional cardiology [218]–[221], precocious puberty [208], acromegaly[222], Hepatitis C [222]–[224], prostate cancer [225]–[227], pain indications [228], type 2 diabetes and Hepatitis [229]–[233]. In contrast, active implantable drug delivery systems are driven by mechanical pumping [144], [145], electrolysis[234], and other actuation methods, which enable patient or physician to start/modify/stop drug release interactively. These systems have been used for emergency care [235], [236], treatment of ocular diseases [237], [238] and cancer [239], and general application in small animals [240]. Active implantable drug delivery systems generally consist of a drug reservoir and a micropump for precise delivery of small volumes of a drug from the reservoir to the target organ. These systems are often normally-closed or have a check valve in the reservoir downstream.

The drug reservoir is an often overlooked component of the active implantable drug delivery microsystems. Depending on the application, drug reservoirs can be refillable or non-refillable. Non-refillable microsystems are usually disposable; they are filled with the drug, implanted, and actuated to discharge the drug. These microsystems have been used in insulin delivery [241], [242], ophthalmology [243], and emergency care [235], [236]. In most of the active implantable drug delivery systems, the drug reservoir is refillable, enabling physicians to transcutaneously refill the reservoir via injections through sharp, thin, non-coring needles into septa in a designated refill port in the system housing [244], [245]. The septa are usually made of silicone rubber[244] with self-healing[246] capabilities due to high resilience[247] and high deformability and self-adherence[248], [249]. The ports typically have a base plate for penetration depth limitation and a cavity between the septum and base plate with an exit channel to provide a fluidic connection to the cavity membrane[147], [250], [251]. In some cases, a raised ridge[147], [252] or a ring with different color[238] is incorporated to assist palpation or visual identification for the surgeon.

Although there are several microsystems in the literature or commercially available that use a septum for refilling[147], [253], only a few of them report the number of punctures they can withstand without leakage. The first refillable microelectromechanical (MEMS) drug delivery device was developed by Lo et al. for the treatment of ocular diseases [237], [238], [254], [255]. Refilling could take place through the top surface of the microsystem, made of polydimethylsiloxane (PDMS), while a Polyether ether ketone baseplate was embedded to control the penetration depth. The refilling port prevented leakage until up to

24 punctures under ~5 and ~30 kPa backpressures for membrane thicknesses of 250 μm and 673 μm, respectively. PROMETRA® programmable pumps (InSet Technologies Incorporation, NJ, USA) use silicone rubber for the septum, rated for withstanding an average of 1000 punctures. Hamilton® GC Septa are rated for a maximum of 100 injections using a 26s Ga needle, with a minimum thickness and diameter of 3 and 5 mm.

The dynamics between the fluid stored in the reservoir and the downstream environment when the pump is deactivated is an important feature in the design of the reservoirs. Since the reservoir membrane material is typically made of rubber-like or metal materials, extraction of the drug causes a restoring force. This restoring force can result in a potential backflow, which in the literature were compensated by either external compression of the membrane[256] or replacement of the drug with electrolysis gases[255]. If not compensated in the cavity area, the backflow is usually prevented with normally-closed micropumps between the reservoir and the downstream system [147], or check valves [238], [240]. To the best of our knowledge, there is no reported microsystem utilizing a cavity membrane with negligible restoring force to integrate to micropumps.

Laboratory animal models play an important role in understanding and treating human diseases. The most common animal models (approximately 95%) in research are rats and mice[257]. However, mice are preferred since they are easier to be genetically manipulated [258]. Further, for subcutaneous implantation to be a minor procedure, the surgery should involve less than 10% of the animal's surface area [259]. These considerations necessitate the need for both miniaturization and scalability of a microsystem for experiments in small animal models (e.g., mice), and later translation to humans. Most of the reported studies

and commercially available drug delivery microsystems have the reservoir and pumping mechanism integrated [240], [253]. Due to limitations for scalability of pumping mechanism, especially for MEMS-based devices, scalability of these devices is challenging. This necessitates the development of a stand-alone implantable microreservoir with different capacities for integration to different micropumps with different flow rates.

Here we present a stand-alone, refillable, scalable, and fully implantable microreservoir platform to be integrated with micropumps as the storing component of an active implantable drug delivery microsystem. This microreservoir platform is intended to have a small footprint and a planar form factor for subcutaneous implantation, especially in small animals (e.g., mouse), while being readily scalable for larger animals and human translation. Using 3D-printing technology to fabricate the microreservoir structure, three different capacities of the microreservoir are demonstrated and characterized (1 µL, 10 µL, and 100 µL). The cavity membrane is fabricated with thin Parylene-C layers using polyethylene glycol (PEG) sacrificial layer and optimized for minimal restoring force as fluid is discharged. The septum thickness is minimized by a novel pre-compression concept enabling thinning of the overall system, while capable of thousands of refills without leakage. To demonstrate integrability of the microreservoir design, it was integrated into a micropump reported in our previous work [73] and implanted in mouse models for inner ear drug delivery. Results indicate functional round window membrane (RWM) drug delivery. Long-term biocompatibility was assessed *in vivo* over six months.

5.2 System overview and concept

To build a microscale, yet scalable structure, stereolithography (SLA) fabrication approach was employed. Formlabs SLA 3D-printer (Form 2, Formlabs Inc., MA, USA) was used to fabricate a rigid biocompatible structure comprising a refill port, cavity area, an outlet port, microchannels to connect them, and a baseplate. This rigid baseplate controls the penetration depth of the refill needle while provides a surface to form the cavity membrane. The rigid frame protects the enclosure and ensures sufficient rigidity for handling.

To provide a completely inert and biocompatible environment for therapeutic compounds, the stored drug was designed to be encapsulated with parylene, which is a USP Class VI material suitable for implant construction. Furthermore, parylene has less permeability to liquid compared to other common materials used in the literature for reservoir membrane, such as PDMS [237] and MDX-4-4210 [240]. After the first layer of parylene deposition, Molten PEG was deposited on the cavity area and solidified to build a biocompatible sacrificial layer, a technique that has been used to form parylene-made cavities [240]. A second parylene layer was deposited on the PEG sacrificial layer to build a thin pre-formed dome-shape cavity membrane. The pre-formed shape and thinness of the cavity membrane enable discharge of the fluid and collapse of the cavity membrane without having a significant restoring force that would result in original shape recovery and undesirable backflow from the outlet. The seal between two parylene layers is enhanced using a compressed biocompatible silicone-made gasket on the cavity edge. The thicknesses of the cavity membranes for three different capacities (1, 10, and 100 μL) were optimized for 100

kPa backpressure, which is four times larger than maximum physiological backpressure in human [260]. This backpressure was used as a criterion for both cavity membrane and septum characterization. For all the cavity sizes, the overall thickness of the microreservoir is set to 3 mm, which was shown to be suitable for long-term subcutaneous implantation in mice. An overview of the microreservoir concept is illustrated in Figure 5.1.

The refill port has a 2.5 mm hole for the septum and a built-in septum stopper to ensure space between the septum and the baseplate, allowing fluid flow to the cavity area. The 2.5-mm septum is micro-molded in cylindrical shape using a biocompatible silicone rubber followed by parylene deposition, to provide complete encapsulation of the drug by the parylene. A cap with a raised compression ring was placed and fixed on the septum to provide vertical compression which improves sealing and facilitates fixation of the septum in the port during injection, which was a challenge in previous reports [261], [262]. The compression cap also causes the septum to laterally push the port wall, inducing lateral compression in the septum, enhancing its self-healing and therefore, increasing its endurance to punctures without leakage. This feature facilitates a significant reduction of the septum thickness, enabling septum down to 1mm thickness to be successfully used. A raised ridge is designed on top of the septum cap to enable subcutaneous palpation and visual access over shaved skin, for performing refills.
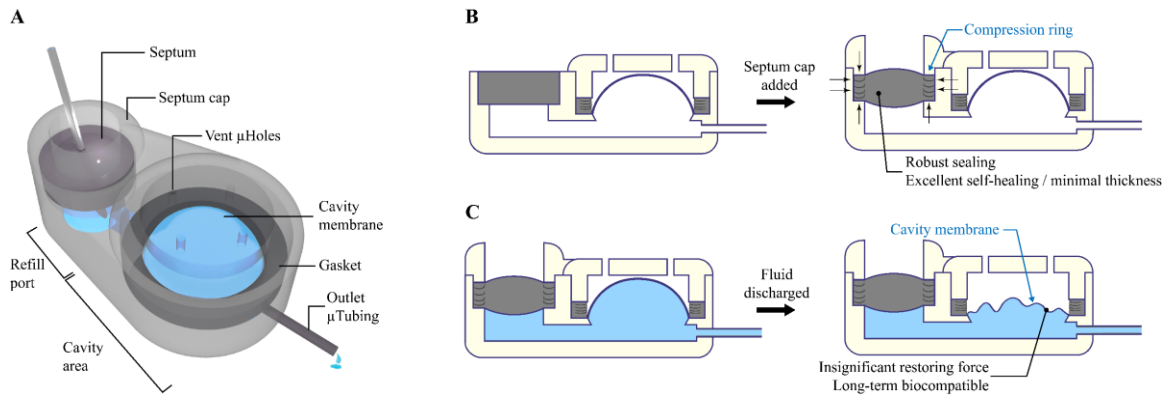
Figure 5.1. A) Conceptual schematic of the microreservoir. The structure of the microreservoir is made of two main sections: the refill port for refilling the microreservoir by injections through a septum, and the cavity area for storing the drug. The structure is made with 3D-printing technology using a biocompatible resin, enabling printing micro-scale features that are readily scalable, enabling applications from mice to humans. B) The septum cap incorporates a compression ring that causes the septum to be compressed both vertically and laterally. The vertical compression ensures sealing from the bottom and holds the septum during multiple injections. The lateral compression induces internal stress in the septum to improve its performance with numerous injections without leakage. This feature enables reduction of the septum thickness while maintaining high resistance to numerous punctures. C) The cavity membrane is made of a pre-formed dome-shape thin parylene layer, enabling negligible restoring force after partial/full discharge of the cavity when the pumping mechanism is switched off. This feature facilitates the integration of the microreservoir to normally-open micropumps and eliminates the necessity of using check valves for low-backpressure environments. Further, when integrated to normally-close micropumps, the constant backpressure on the check valves are eliminated and the pumping efficiency increases. Finally, since the entire internal surface of the microreservoir, including the septum and the cavity membrane, is coated with a parylene layer, long-term biocompatibility for drug storing is ensured.

5.3 Fabrication process

The microreservoir substrate was 3D-printed (Form 2, Formlabs Inc., MA, USA) using a rigid biocompatible material (Dental SG resin, Formlabs Inc., MA, USA) creating a hole of 2.5-mm diameter and 1-mm depth for the septum, cavity area, outlet port, fluidic interconnections between them, and a baseplate. In the cavity area, a raised circle-shaped ring was considered for placing the gasket, with an angled wall to the baseplate to reduce the cavity dead volume. In the refill port, a septum stopper with a diameter of 1.8 mm was designed, providing a seat for the septum. A polyurethane-based catheter microtubing (ID=125 μm, OD=250 μm; Micro-Renathane® Catheter Tubing, Braintree Scientific Inc., MA, USA) was fixed and sealed to the output port, using cyanoacrylate. The structure was coated with a 1-μm-thick layer of parylene using PDS 2010 LABCOATER™ 2 (both Specialty Coating Systems, Indianapolis, IN, USA).

Cavities with three different capacities (1, 10, and 100 μL) were fabricated, where the diameters of the cavity area for each of them were empirically found to be 1.5, 3.1, and 10 mm, considering 3 mm objective for the overall thickness. To build the cavity membrane with parylene-C, a sacrificial layer is required, which defines the capacity of the cavity after release. PEG (1,500 Mn, melting point: 37 °C, Sigma- Aldrich, MO, USA) was chosen for the sacrificial layer due to its biocompatibility and solubility in water. PEG was melted at 70 °C on a hotplate and mixed with a dye (McCormick & CO., MD, USA) for visual confirmation of its release. Using a heated micropipette (70 °C), PEG was deposited on the cavity area which was held at room temperature and treated with hydrophobic spray

(Scotchgard™ Fabric & Upholstery Protector, 3M Co, MN, USA) for quick solidification of PEG and avoiding its flow into the space under the septum and the gasket raised ring. It was empirically found that keeping the substrate at room temperature can result in smooth PEG surfaces, while providing a sufficiently fast cooling rate to avoid the flow of the PEG in the channel regions. The full volume of required PEG (1, 10, and 100 µL, considering phase-change expansion of PEG) were deposited with a single micropipette dispense.

To make the cavity membrane on top of the PEG sacrificial layer, the required thickness of the second parylene layer for different capacities was estimated based on thin-walled spherical pressure:

$$\sigma = pr / 2t \tag{5.1}$$

where σ, p, r, and t represent tensile stress on the membrane, internal pressure, cavity radius, and membrane thickness, respectively. The membrane is designed for 100 kPa backpressure or refilling pressure (p= 100 kPa), while the radius was determined based on overall thickness and capacity. The thicknesses of the parylene membrane for each cavity size was calculated to achieve membrane stresses smaller than the tensile strength of parylene (69 MPa [263]) by a factor of 5. The thicknesses of deposited parylene membranes were 2.7, 5.6, and 18.1 µm for 1, 10, and 100 µL capacities.

Silicone rubber (MED-6215, NuSil™ Technology LLC, CA, USA) gaskets with 0.5 mm width and height with inner diameters of 1.5, 3.1, and 10 mm for capacities of 1, 10, and 100 µL, respectively, were micro-molded using a parylene-coated aluminum mold fabricated with conventional machining. The gaskets were cured at 150 °C for 15 min. The

gaskets were placed on the cavity area and was fixed and compressed using a cavity cap which was 3D-printed (Form 2, Formlabs Inc., MA, USA) and parylene coated, to provide mechanical compression on the touching surface of two parylene layers for a tight seal. The cavity cap also covers the cavity membrane to protect it from external mechanical stress. Vent holes with 0.2-mm diameter were made in the cavity cap to allow ingress and egress of air or liquid from the space between the cap and the cavity membrane during filling and discharging. These holes are smaller than the smallest needle size for this microreservoir (30 Ga, 311 um OD) to avoid inadvertent puncture of the membrane during subcutaneously refilling. The use of class VI biocompatible silicone rubber for the gasket and parylene deposition of the cavity caps minimizes the risk of inflammation with direct contact to body tissues.

Under visual observation using a microscope (Motic SMZ-168), the substrate was heated on a hotplate at 70 °C to melt the PEG, allowing it to be rinsed away with 100 mL 70°C deionized (DI) water. A silicone septum with 2.5 mm diameter and 1 mm thickness was micro-molded using parylene-coated 3D-printed molds and cured at 150 °C for 15 min and were coated with 1 μm parylene layer. The septum was placed in the refill port followed by placing and affixing a 3D-printed septum cap using cyanoacrylate. The septum cap incorporates a 0.2-mm-thick compression ring (1.8 mm ID, 2.5 mm OD) to compress the septum to provide internal stress for improving its self-healing properties. A raised ridge (1.8 mm ID, 3 mm OD, 0.5 mm thickness) was considered for top of septum cap to facilitate palpation for subcutaneous refilling. All the surfaces were filleted to minimize potential

mechanical inflammation after implantation. The full fabrication process is illustrated in Figure 5.2.
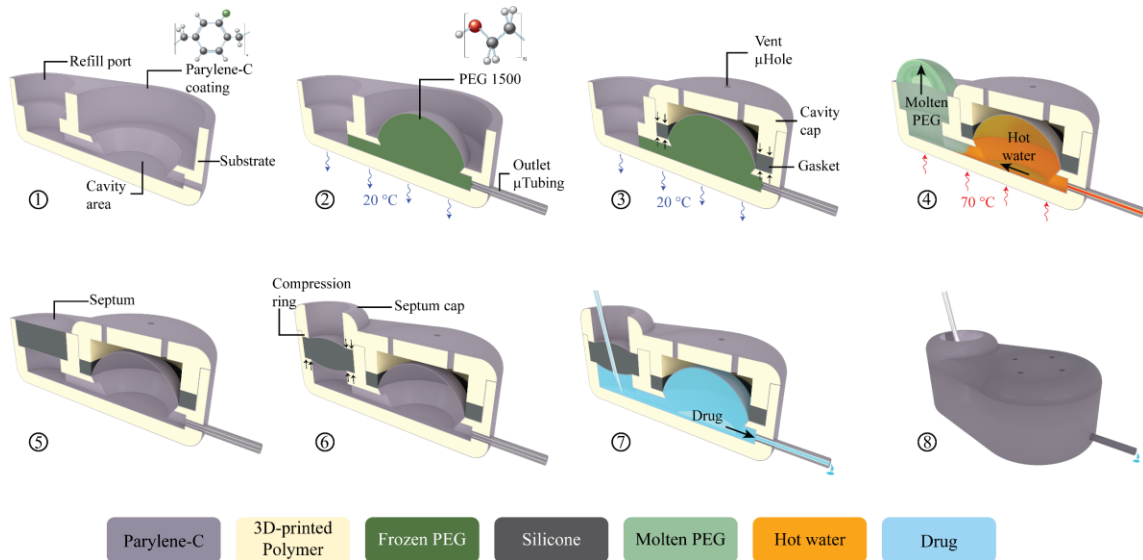
Figure 5.2. A cut-view schematic of the microreservoir fabrication process. 1) The substrate of the microreservoir was 3D-printed using a biocompatible resin, followed by 1 μm parylene-C deposition. 2)A microtubing (250 μm OD, 125 μm ID) was inserted into the substrate outlet port and sealed in place with cyanoacrylate. The substrate was placed on a cold plate at room temperature and molten PEG at 70 °C was deposited on the cavity area to solidify and create the microreservoir volume. This was followed by another Parylene-C deposition to create the deformable microreservoir membrane capable of withstanding 100 kPa backpressure. 3) A silicone gasket was fabricated using a micro-molding technique and was placed within the cavity around the PEG dome. A 3D-printed Parylene-C coated cap was affixed on top of the cavity area with cyanoacrylate, compressing the O-ring to reinforce sealing between the two Parylene-C layers, and to protect the cavity from mechanical stress. The cap has vents to allow egress/ingress of air or fluid between the membrane and the cap during filling/discharging. 4) The substrate was placed on a hotplate at 70 °C to melt the PEG and wash it by gentle injection of 100 mL of DI water at 70 °C 5) A 2.5-mm diameter, 1-mm-thick septum made of long-term implantable silicone rubber was micro-molded and coated with parylene-C. The septum was placed in the refilling port (2.5 mm diameter). 6) A 3D-printed, Parylene-C coated septum cap with an extruded compression (2.5 mm OD, 1.8 mm ID) was affixed on top of the septum with cyanoacrylate to compress the septum providing a sealing force on the bottom and sides while enhancing the self-healing properties when punctured with refilling needles. 7) schematic cut view of the fabricated microreservoir being filled by a refilling needle. 8) A schematic full-body view of the microreservoir.

5.4 Benchtop experimental method

To assess the functionality of the septum and the cavity membrane, these two parts were decoupled and tested separately. Two separate sets of test rigs were designed, fabricated, and tested on samples fabricated following the same fabrication process described in section 0.

5.4.1 Septum test

The septum was tested utilizing separately fabricated septum samples, consisting of a 3D-printed refill port with septum stopper and space beneath it along with the outlet coupled to a Tygon tubing (0.508 mm ID, 1.52 mm OD). The septum and septum cap were then placed and fixed in the refill port. Although in some studies the septum leakage test is performed using N_2 as the working fluid [261], here we tested the septum using dyed DI water since it simulates the *in situ* condition where the septum is in contact with a liquid drug.

A pneumatic puncture device was designed and fabricated to hold the septum sample and automatically puncture through the septum in a single location, to test the worst-case scenario [238], [261]. The structure of the pneumatic puncture device was 3D-printed using Grey Pro resin (Formlabs Inc., MA, USA), having a groove for the test sample to be placed and fixed with a set screw beneath the pneumatic puncture mechanism. A miniature

cylinder (SM-3-1, Clippard Co., OH, USA) was placed and fixed on top of the sample. An electronic pressure regulator (ITV2030-31N2BL4, SMC Co., Tokyo, Japan) was connected to the cylinder which was fed with sine waves of 0.2 Hz frequency by a signal generator, to simulate a realistic manual puncture speed. A needle was affixed to a 3D-printed needle holder which was press-fit to the piston of the cylinder.

Commercially available 27 and 30 Ga (413 and 311 µm OD) needles were used for the puncture tests. These sizes were selected as a trade-off between maximizing needle and septum lifetime: the needles need to be large enough to puncture through the skin and the septum without bending the tip, while small enough to minimize septum damage. Furthermore, the opening diameter of the septum cap is 1.8 mm, making needle sizes larger than 27 Ga impractical. The needles were machined to non-coring shape to minimize damage to the septum structure [237], [238], [254]. The needle tip was beveled to a point with a 12° angle recommended for animal injections [264]. Figure 5.3A shows the pneumatic puncture device with a 30 Ga needle.

Septum samples were prepared for puncture experiments with 27 and 30 Ga needles, where the septum cap incorporated the compression ring to compress the septum vertically and laterally for enhanced self-healing. To investigate the effect of the compression ring on the self-healing characteristics of the septum, one batch of samples (N=4) were fabricated without the septum cap. Instead, they were fixed and sealed in the refill port using cyanoacrylate, causing no compression to the septum. 30 Ga needles were used for this experiment, and the results were compared with the samples with the septum cap incorporating compression ring, punctured with 27 and 30 Ga needles (N=4 for each).

To test septum function, the space beneath the septum and 5 cm of the outlet tubing were filled with dyed DI water using the sharp (12°) non-coring needles, and the septum samples were fixed in the pneumatic puncture device. The outlet tubing was placed on a ruler. The signal generator was switched on, and the septum was punctured until switched off after each step, following a logarithmic scale $10^{0.2}$ step size. Backpressure of 100 kPa (with gradual increments) was applied to the outlet tubing for 1 min. The fluid displacement in the tubing was observed/recorded with a digital microscope (USB-MICRO-250X, Plugable®, WA, USA) and analyzed with NIH-ImageJ, resulting in a resolution of 2.4 nL/min. Leakage was detected if a backward displacement of the fluid in the tubing was observed. If no leakage was observed the test continued by switching on the signal generator until the next step. The number of punctures before leakage was found for each case based on the last value with no leakage (Figure 5.3B). A manual puncture experiment was performed to explore septum operation at more practical conditions where a surgeon/medical doctor refills an implanted device numerous times.

5.4.2 Cavity membrane test

Microreservoir cavity volume, backflow due to membrane restoring force, and total fluid extraction percentage for three different cavity sizes were characterized. The cavity samples were fabricated and tested separately, consisting of the cavity membrane (described in section 5.3), but with modifications to facilitate the test. The cavity inlet was directly connected to an inlet tubing, a three-way stopcock, and syringes for cavity filling,

124

with an outlet tubing aligned over a ruler to quantify fluid movement due to pneumatic pressure applied to the region above the cavity membrane.

To fill the cavity, the pneumatic pressure was set to zero, and a syringe was connected to the inlet port and pulled to remove air from the cavity and pull the membrane down to its minimum volume. The syringe was replaced with a three-way stopcock connecting to the inlet tubing. Dyed DI water was injected to fill the inlet tube up to the entrance of the cavity via visual observation under a microscope. A small volume syringe was then connected via the stopcock to accurately quantify injected volume, with a 25 µL syringe (1702 LT SYR, Hamilton Co., NV, USA) used for the 1 and 10 µL cavities, and a 250 µL syringe (1725 TLL, Hamilton Co., NV, USA) used for the 100 µL cavity. With the outlet tubing open, the syringe was discharged until the fluid was observed to reach the microreservoir exit. The outlet tubing was clamped closed, and the syringe discharged to fill the cavity, confirmed by visual observation under a microscope. The three-way stopcock was switched to block flow on the inlet side, the outlet tubing clamp released, and the fluid volume in the outlet tubing quantified. The cavity volume was calculated by subtraction of the fluid volume in the outlet tubing from the injected fluid volume from the syringe.

The backflow due to restoring force of the cavity membrane was characterized for cavity fill volumes of ~ 80%, 60%, 40%, 20%, and 0%. Pneumatic pressure was applied above the cavity membrane for 1 min to induce forward fluid movement, as shown in Figure 5.3D. After discharge of ~20% of the volume, the pneumatic pressure was released, and the fluid front displacement in the outlet tubing was observed under a microscope for 4 min (Figure 5.3E). For three different cavity sizes, three different outlet tubing sizes were used

to have a minimum resolution of 0.1% of the full capacity using a 0.5-mm graded ruler. The backflow of the fluid front is recorded, and the experiment is repeated for the next 20% of the overall volume. The total fluid in the outlet tubing after the fifth step indicates the total extraction percentage. Three samples for each of three different cavity sizes of 1, 10, and 100 µL were tested with three replications (N=9 for each size, total N= 27).
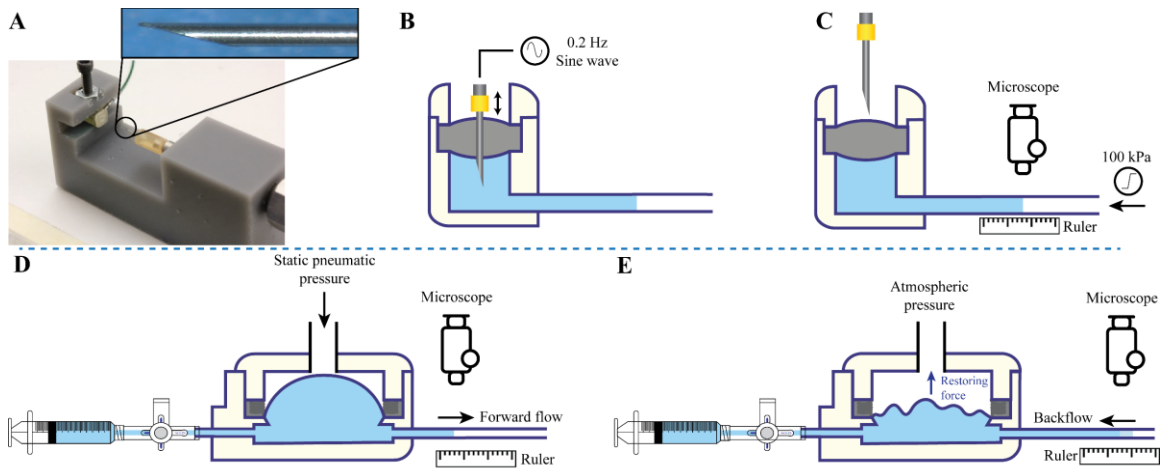
Figure 5.3. Benchtop characterization test setup for septum (Top) and cavity membrane (Bottom) characterization. Septum characterization: A) A custom-made 3D-printed pneumatic puncture device. Inset: a 30 Ga non-coring 12° beveled needle used for puncture test. B) The septum test samples were punctured in a single point following a logarithmic number of punctures with the puncture device fed by a 0.2 Hz sine wave signal. C) With the needle extracted, backpressure was gradually increased to 100 kPa while the fluid front displacement was quantified by visual observation under a microscope. Cavity characterization: D) Following the filling of the microreservoir cavity and fluidically blocking the inlet, the fluid in the cavity membrane was pumped out via a static pneumatic pressure on the membrane to provide forward flow. E) The pneumatic pressure was released, and the backflow in the tubing due to the restoring force of the membrane was quantified under a microscope. Different tubing sizes were used for the three different cavity capacities (1, 10, 100 µL) to maintain a minimum resolution of 0.1% of the full microreservoir capacity.

5.5 In vitro results and discussion

The completed microreservoirs are shown in Figure 5.4A. The overall footprints of the microreservoirs are 4.5×3 (1 µL), 7.6×4.6 (10 µL), and 14.5×11.5 mm^2 (100 µL) with a thickness of 3 mm for all. *In vitro* experiments were performed to optimize the septum design and thickness for thousands of refilling injections without leakage and quantify backflow due to restoring force after extraction of liquid. Further, the total volume of the cavities and total extraction percentage of them were assessed. The cavity membrane experiments were performed on all three capacities of 1, 10, and 100 µL to demonstrate the scalability of the design.

5.5.1 Septum characterization

The results (Figure 5.4B) indicated that the samples without the compression ring could not withstand one puncture and leaked at backpressures as low as 5 kPa. In contrast, the samples with the compression ring withstood up to ~65,000 punctures without any leakage at 100 kPa backpressure using the 30 Ga needle. However, using the 27 Ga needle reduced the number of punctures without leakage to 55. Comparison between the results of 30 Ga needle puncture with and without the compression ring indicates its significance in increasing the septum lifetime. Further, the results of 27 Ga punctures demonstrate the high endurance of this septum in taking up to 55 punctures, which is sufficient for many therapeutic development and clinical applications (e.g., [242], [265]).

Use of a 33 Ga needle (210 μm OD) dramatically enhances the robustness of this ultrathin septum to levels that far exceed any practical use case. This smaller gauge needle was successfully used in our *in vivo* experiments (section 6.4) with multiple successful subcutaneous injections in mice. The results of manual punctures of the septum show ~500 punctures without leakage at up to 100 kPa backpressure. The experiment was stopped after 500 punctures, so the failure point with manual punctures is not known. However, considering one refill per day, this test indicates that the septum can operate leak-free for more than one year.

All septum puncture experiments were performed on 1-mm thick septa. Testing on 0.5-mm thick septa showed poor functionality at low backpressures even with the compression ring. This could have been due to fabrication limitations for controlling the thickness of the compression ring and the buckling of the septum due to the lateral force of the compression. This novel septum design can be employed in any refillable system, independent of the cavity membrane design.

5.5.2 Cavity membrane characterization

The results indicated that the overall capacities of the cavities were 1.5 ± 0.09, 9.63 ± 0.12, and 100.04 ± 9.43 (mean $\pm$ SD) for target volumes of 1, 10, and 100 μL, see Figure 5.4C. Figure 5.4D shows the average of extracted volume during pumping and resting for three different nominal capacities of 1, 10, and 100 μL, normalized by the total volume of each cavity. Each data point is an average of three sizes, each with three samples and three

replications (N = 27). The results show that for all steps the backflow was not significant compared to the overall size (2% average). The backflow at each step occurs relatively quickly after deactivation of pumping (< 2 min for all cases), ensuring stable behavior of the cavity membrane for long-term applications. Further, no significant difference in the backflow was observed across different extraction percentage, except for the last step, which defines the total extraction percentage of the cavities. The average total extraction percentage was 95%.

Experiments on samples with twice thicker membranes for all three sizes (N=27) showed significant more backflow due to restoring force (3.8% average). This significant difference ($p < 0.001$) is directly related to the thickness of the membranes. As the membrane becomes thicker, its resistance to deformation increases, which results in a higher restoring force and greater backflow when the pneumatic pressure is released. We hypothesize that the total extraction percentage is a function of the discrepancy between the surface area of the membrane and the substrate. If the membrane surface area is larger than the substrate, when fully pushed down by the pneumatic pressure the membrane wrinkles on the substrate and resists against further pressure. When the pneumatic pressure is released these areas induce restoring force and backflow. On the other hand, if the membrane surface area is smaller than the substrate, there is space between the membrane and the substrate that cannot be swept by the membrane unless with further pressure, which restores when the pressure is released and causes backflow. The fluid loss due to evaporation were not explored here because the *in situ* application of the device is subcutaneously implanted, which is a moisture-saturated environment.
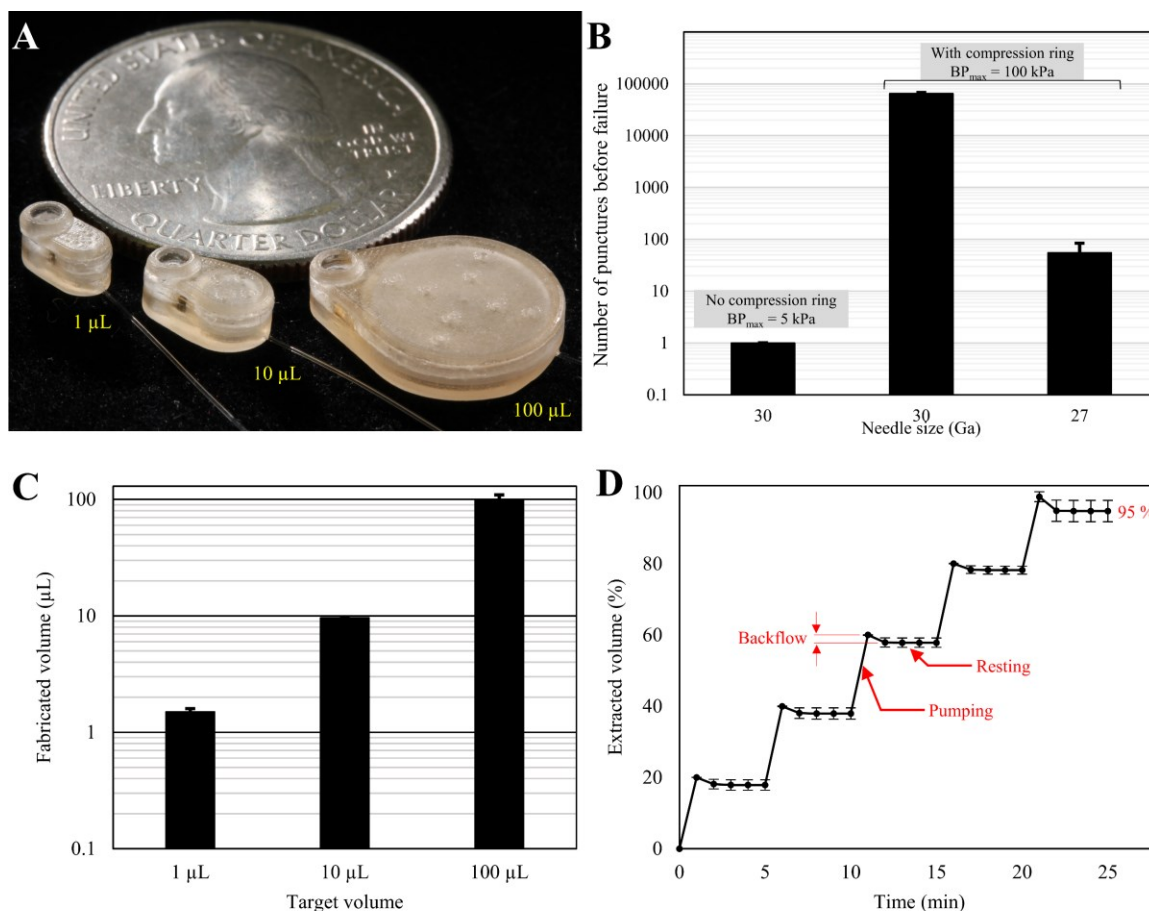
Figure 5.4. A) Photograph of completed microreservoirs with capacities of 1, 10, 100 μL, showing the scalability of the design and fabrication process. **B)** Septum characterization results show that the samples without the compression ring leaked at less than 5 kPa backpressure with just one puncture with a 30 Ga needle. Adding a compression ring to the septum cap increased the number of punctures before failure to ~65,000 at 100 kPa backpressure when puncturing with a 30 Ga needle. This design can provide no leakage up to 55 injections at 100 kPa backpressure when punctured by a 27 Ga needle. N=4, mean ± SD. **C)** Comparison between the fabricated volume and the target volume shows 1.5 ± 0.09, 9.63 ± 0.12, and 100.04 ± 9.43 for target volumes of 1, 10, and 100 μL. N=4, mean ± SD. **D)** The average results of the backflow due to restoring force for three different capacities of 1, 10, and 100 μL normalized by the total volume of each cavity. The results show that the overall backflow is not significant (2% average) and occurs quickly (< 2 min) after pneumatic pressure release, suggesting stable behavior of the cavity membrane in long-term. The last step of the experiment shows the total extraction percentage. N=27, mean ± SD.

5.6 Conclusion

We developed a stand-alone refillable, scalable microreservoir designed for integration to an active pumping mechanism, optimized for subcutaneously implanted microsystems. The microreservoir structure has two main components: the refill port for refilling with subcutaneous injection through a septum, and the cavity area to store the drug for long-term applications. The microreservoir was built upon a 3D-printed biocompatible structure, providing mechanical protection and strength for handling, a stiff baseplate for the needle at the bottom of refill port, and a baseplate for the cavity area. Further, 3D-printing technology enables readily scalability of the design, indicating translational opportunities. The cavity membrane was fabricated with parylene-C using PEG as the sacrificial layer, over the parylene-C-coated substrate. The septum was fabricated using long-term biocompatible silicone rubber and coated with parylene-C. The biocompatibility of the system was reinforced by ensuring that all the materials are biocompatible, even for the sacrificial layer.

The durability of the septum was significantly improved by adding a compression ring to the septum cap to induce internal compression in the septum. *In vitro* characterization results demonstrate no leakage after up to ~65,000 injections with 30 Ga needle at up to 100 kPa backpressure, which is significantly higher than the maximum backpressure in human and mice. The suitability of the needle size was verified by *in vivo* experiments which showed that needles as small as 33 Ga are sufficient for subcutaneous refills. This novel septum design can be used in different refillable microreservoirs. Scalability of the

design and fabrication process was demonstrated by the fabrication of three different cavity sizes (1, 10, 100 µL) while keeping the overall thickness 3 mm. *In vivo* experiments demonstrated the suitability of this thickness for long-term (6 months) subcutaneous implantation in mice. The thickness of the cavity membrane was optimized to have near-zero restoring force to avoid backflow after pumping the fluid out of the cavity. *In vitro* characterization results show that the optimized membrane reduces the backflow as low as 2% of the overall volume of the cavity. This feature permits integration of the microreservoir to normally-open micropumps for applications with low backpressure (e.g., RWM in the inner ear). Further, it eliminates the long-term backpressure on check valves when integrated to normally-closed micropumps, and improves pumping efficiency.

The presented microreservoir was shown to be able to be refillable for thousands of injections with minimal backflow due to the extraction of the fluid, when the pumping mechanism is off. Scalability of the design and fabrication process was demonstrated by the fabrication of three different cavity sizes (1, 10 100 µL), indicating translational opportunities. It was also shown that this microreservoir could be integrated with a pumping mechanism that either sucks the fluid from the outlet tubing (the integrated microsystem) or pushes the fluid directly from the top surface of membrane using pneumatic pressure (the cavity membrane test). Future work will incorporate a pumping mechanism from the membrane top surface for LOC or drug delivery applications.

Chapter 6 Fully Implantable Microsystem For Inner Ear Drug Delivery

6.1 Introduction

The micropump presented in Chapter 3 and the 10 µL microreservoir demonstrated in Chapter 5 were integrated, making an implantable microsystem for inner ear drug delivery. In this chapter the fabrication process of the microsystem for integration of these two devices are presented along with details of implantation surgery. Inner ear drug delivery using this microsystem is briefly described here, while more details can be found in section 3.7. Details of a long-term biocompatibility experiment is presented along with details of histology methods. Results of acute delivery of Salicylate into RWM matched with syringe pump. Further, the long-term biocompatibility experiment showed that the microsystem can be subcutaneously implanted for long-term without significant inflammation or infection.

133

6.2 Fabrication process

To demonstrate integrability of the microreservoir to a micropump, a 10 µL microreservoir was integrated with an implantable micropump for inner ear drug delivery, recently developed in our group [73]. A miniature container was 3D-printed for the micropump right beside the microreservoir, while the overall thickness was kept at 3 mm. Fillets with 1 mm radius were applied to the container walls to provide curved surfaces to improve long-term subcutaneous implantability. The microreservoir was built following the fabrication process outlined in Figure 5.2. The micropump was placed in the container, and its microtubing was placed and sealed to the microreservoir outlet using cyanoacrylate. The micropump was then fixed in the container using cyanoacrylate, and the silicone rubber (MED-6215, NuSil™ Technology LLC, CA, USA) was poured in the container and cured at room temperature for 48 hrs. To soften the device surface, the entire microsystem except the cavity cap was covered with a thin layer of silicone by manually applying droplets of silicone to evenly coat the outer surface and cured at room temperature for 48 hrs.

6.3 Experimental methods

The integrated microsystem (microreservoir + micropump) was tested *in vivo* to show its suitability of subcutaneous implantation, functionality for acute drug delivery to the mouse inner ear, and capability for long-term implantation. The drug delivery test was performed following a protocol developed by our laboratory [25], for the administration of sodium salicylate, leading to temporary hearing loss – reversible shifts of otoacoustic emissions thresholds and levels. Salicylate can act as a competitive antagonist at the anion-binding site of prestin [196], which causes reversible disruption of outer hair cell motility. Specifically, this disruption of prestin causes a reduction in distortion product otoacoustic emission (DPOAE) amplitudes and thresholds. Therefore, salicylate was delivered to the round window membrane (RWM) and auditory function was evaluated using DPOAE measurements. To evaluate long-term biocompatibility, the microreservoir was implanted for six months with frozen sections of surrounding tissue analyzed histologically for signs of inflammation. Finally, to explore capability of the micropump for self-priming was explored.

6.3.1 Subcutaneous implantation and biocompatibility

The anesthetic used was ketamine (120mg/kg body weight), xylazine (10 mg/kg body weight) in combination with topical application of 4% lidocaine for analgesia for the implant surgery. Specifically, a young adult CBA/CaJ mouse was positioned on a servo-

controlled heating pad maintaining aseptic conditions, and when the proper plane of anesthetic was achieved (toe pinch, heart rate, respiratory rate), the upper back was then shaved and cleaned, and the microsystem was inserted subcutaneously in the center of the upper back via a small incision. Supplementary doses at one-third of the initial dose were administered as needed to maintain the proper levels of general anesthesia. Following insertion ventral to the dermis, Medical grade adhesive (Loctite 4206, Rocky Hill, CT) was used to secure the wound closure, along with several stitches to close the incision over the microsystem.

After survival for six months, the mouse was sacrificed by an overdose of anesthetic via intracardial perfusion with 4% paraformaldehyde fixative. Next, tissue samples were dissected from around the microsystem and prepared for standard frozen sectioning followed by hematoxylin + eosin (H&E) tissue staining to visualize cellular locations and structure around the microsystem. All animal procedures were approved by the University of South Florida Institutional Animal Care and Use Committee and were performed using the National Institutes of Health and veterinary standards of care.

6.3.2 Inner ear drug delivery

Two young adult (2-4 months of age) CBA/CaJ mice bred and raised in-house were used for this study. After subcutaneous implantation of the microsystems in the center of the upper back (section 0), a bullaostomy surgery was performed to prepare a site for infusion of the salicylate into the middle ear cavity. A mixture of ketamine (120 mg/kg body weight)

and xylazine (10 mg/kg body weight) injected via the intraperitoneal route to deeply anesthetize the mice for the bullaostomy surgery. The left ventral surface of the neck was then shaved and cleaned. Surgery was performed on the left (ipsilateral) ear following procedures described by Borkholder et al. [25]. During infusions, each mouse was immobilized using anesthesia with supplementary doses at one-third of the initial dose administered as needed to maintain the proper levels of general anesthesia.

Auditory function was assessed via automated DPOAE threshold measurements at F2 frequencies of 8.9 kHz, 13.5 kHz, 17.9 kHz, 24.6 kHz, 35.8 kHz, and 51.4 kHz. Measurements performed before the surgery were used for a baseline to compare subsequent DPOAE threshold shifts. Further details of auditory function assessment are presented in our previous work [73], [200].

The salicylate solution consisted of NaCl (120 mM), KCl (3.5 mM), $CaCl_2$ (1.5 mM), glucose (5.5 mM), HEPES buffer (4-(2-hydroxyethyl)- 1-piperazineethanesulfonic acid, 20 mM), and sodium salicylate (50 mM). The pH was adjusted to 7.5 using NaOH. All solutions were prepared on the day of the experiment using sterile double-distilled water. The salicylate was loaded into a 25 µL sterilized syringe (1702 LT SYR, Hamilton Co., NV, USA) with a needle (33 Ga, 7747-01, point style 4, 12°, 1", Hamilton Co., NV, USA) and was debubbled. The microreservoir was filled by injection through refill port using the needle and the salicylate was pushed through the tubing using positive syringe pressure until it was 1 mm from the microtubing tip.

The infusion of the salicylate was enabled by a novel biocompatible, implantable, scalable, and wirelessly controlled peristaltic micropump recently developed at our laboratory [73].

The mechanical components of the micropump were fabricated using direct-write 3D-printing technology on back of a printed circuit board assembly (PCBA), around the catheter microtubing outlet of the microreservoir to provide a biocompatible leak-free flow path while avoiding complicated microfluidic interconnects. The peristalsis is enabled by phase-change actuation of three chambers made adjacent to the microtubing. The actuation, control, and Bluetooth communication electronics were fabricated on the front side of the PCBA, effectively integrating mechanical and electronic components in a thin structure. The micropump operation is completely controlled through Bluetooth communication using a custom-made Android application. The micropump *in vitro* characterization results showed by tuning the actuation frequency of the micropump, nanoliter resolution flow rate across the range of 10-100 nL/min is generated, in the presence of $10\times$ physiological inner ear backpressures and ± 3 °C fluctuation in ambient temperature. It was also shown that the micropump could provide 50 nL/min for 20 min with 0.4% error in overall delivered drug volume, which was shown to temporarily impact the DPOAE threshold shift [73]. The integrated micropump operation was optimized for working in the subcutaneous temperature of mice (~33 °C) in a liquid environment (glycerin) with similar thermal characteristics to subcutaneous tissues to provide a flow rate of 50 nL/min for long-term performance.

6.3.3 Micropump air bubble-tolerance experiment

Bubbles are one of the sources of inaccuracy and defection in microfluidic systems. In this device also bubbles can be introduced during refills, when the needle punctures the septum and enters the microfluidic system. The maximum bubble size that could be trapped between the fluid in a 12° beveled non-coring 30 Ga needle and the septum was calculated using Solidworks® to be ~7.5 nL (Figure 6.1). It should be noted that since the microtubing end of this device is implanted at the RWM which is open to atmospheric pressure, air bubbles do not induce challenges for the organ. In addition, it has been shown in the literature that bubbles as small as 10 nL do not have any disruptive effect on auditory function even when injected directly into the basal turn of scala tympani [29].

Figure 6.1. Fluid in a 12° beveled non-coring 30 Ga needle and trapped air between it and the septum. The trapped air can introduce air bubbles to the system as big as 7.5 nL.

To explore micropump capability of propelling the fluid in presence of air bubbles an air bubble of ~60 nL was introduced to the microsystem and the micropump was switched on. This bubble is ~8 times larger than the practical air bubbles that can be introduced to the system during refills.

6.4 Results and discussion

The completed integrated microsystem is depicted in Figure 6.2A. The overall microsystem size measures $19 \times 13 \times 3$ mm^3 (L × W × H) which is significantly smaller than a typical mouse and can be subcutaneously implanted due to its planar form factor (Figure 6.2B). To evaluate the functionality of the microsystem, the outlet microtubing of the microsystem was implanted at the RWM niche to deliver salicylate at 50 nL/min for 20 min, replicating a previous drug delivery system utilizing a syringe pump [25]. Auditory function was measured during the infusion using the DPOAE method. Finally, the capability of the microsystem for long-term implantation was tested via standard frozen sectioning analysis of the tissue around it.

6.4.1 Inner ear drug delivery

The accessibility of the refill port of the microreservoir was explored by palpation and observation of the raised ridge of the refill port when the shaved skin of the mouse is

stretched (Figure 6.2C). Subcutaneous injections through the mouse skin were successfully performed by a 33 Ga (210 μm OD) non-coring needle (7747-01, point style 4, 12°, 1", Hamilton Co., NV, USA), demonstrating *in vivo* validity of the larger 27 and 30 Ga syringe needles used for the septum characterization test.

Drug delivery experiments were performed using the integrated microsystem to show the performance of the system while implanted (two microsystems in two mice). Acute deliveries were run to deliver salicylate at the RWM niche at 50 nL/min for 20 min, while the DPOAE threshold shifts were recorded during the infusion, to replicate a previous experiment that was performed using a syringe pump [25]. The Android application enabled readily control of the device for staring/stopping the infusion. The results of the mean threshold shift of the most basal region (F2 = 51.4 kHz) for microsystems and the syringe pump are presented in Figure 6.2D. A baseline measurement was acquired approximately 10–15 min before the cannula placement surgery. The results compare the changes in DPOAE thresholds to baseline at four time-points: post-surgery (PS) in which DPOAE values were acquired immediately before the micropump was turned on, 0 min, the time at which the micropump was turned on, and 10 and 20 min after the onset of salicylate perfusion. There were mean shifts of 6.8 and 22.1 dB after 10 min and 20 min infusion for the implanted microsystems, in consistency with the syringe pump results, suggesting the successful performance of the implanted microsystem.

6.4.2 Long-term biocompatibility

The mouse recovered well from the surgery, and over the six-month survival period, was in good health. Post-implantation, the mouse was monitored daily and the results indicated that the overall health was excellent. This included no signs of fever or infection, no significant swelling, no redness or lumps around the micropump location or incision, nor presence of discolored fluid, and no weight loss. Cage behaviors, including feeding, grooming, and drinking were normal. The mouse was photographed on a weekly basis during the six months period.

The histological processing of the tissue surrounding the microsystem revealed a significant fibrotic layer around it, along with some ingrown hair follicles associated with the incision site. Otherwise, there were no cellular indications of infections or additional inflammatory responses, or abnormal cellular structures or responses.

A typical section of the skin surrounding the microsystem is shown in Figure 6.2E. The skin surface is on the bottom, showing the normal dermal layers, with no sign of any active, inflammatory cells. The microsystem was in the cavity on the upper surface; here a fibrotic layer is seen (pink) which fully encapsulated the microsystem. This was the only abnormal features of the tissue surrounding the microsystem after six months survival, other than the dark hair follicles (upper right of the Figure 6.2E) associated with the incision site.
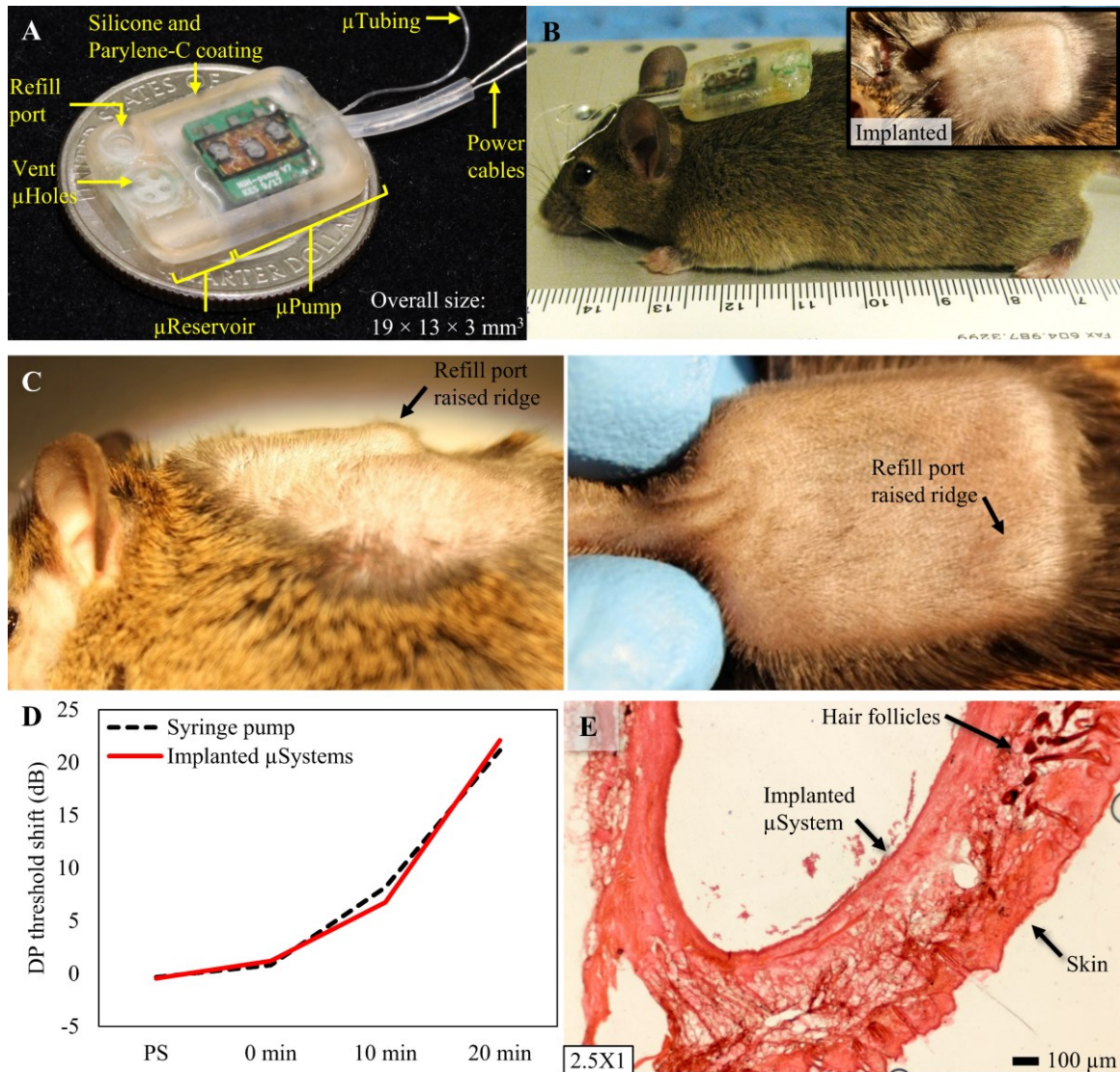
Figure 6.2. A) Photograph of the microreservoir integrated with a micropump for inner ear drug delivery that was recently reported [60]. The microsystem is optimized for subcutaneous implantation in mice with an overall thickness of 3 mm. B) Photograph of a microsystem before implantation demonstrates thinness of the microsystem, which makes it optimized for subcutaneous implantation in mice. Inset: An image of the microsystem after implantation via insertion of the microsystem in a small incision made in the center of the upper back of a mouse. C) Side view and top view of a microsystem implanted showing the visibility of the refilling port. D) Results of the mean threshold shift of the most basal region (F2 = 51.4 kHz) for implanted microsystems and the syringe pump show perfect consistency, demonstrating successful performance of the microsystem (N=6 for syringe pumps, N=2 for microsystems). E) A typical 60 µm-thick section of the skin surrounding the microsystem shows no sign of any active inflammatory cells. A fibrotic layer (pink) fully encapsulated the microsystem.

143

6.4.3 Bubble-tolerance capability

Figure 6.3 shows the capability of micropump to propel the fluid in existence of a 60 nL air bubble in the fluid path. In existence of a large bubble, the micropump sucks the liquid (Figure 6.3A and Figure 6.3B) and pumps it out of the device to downstream (Figure 6.3C and Figure 6.3D). This indicates that the micropump can operate in presence of air bubbles introduced by refills.
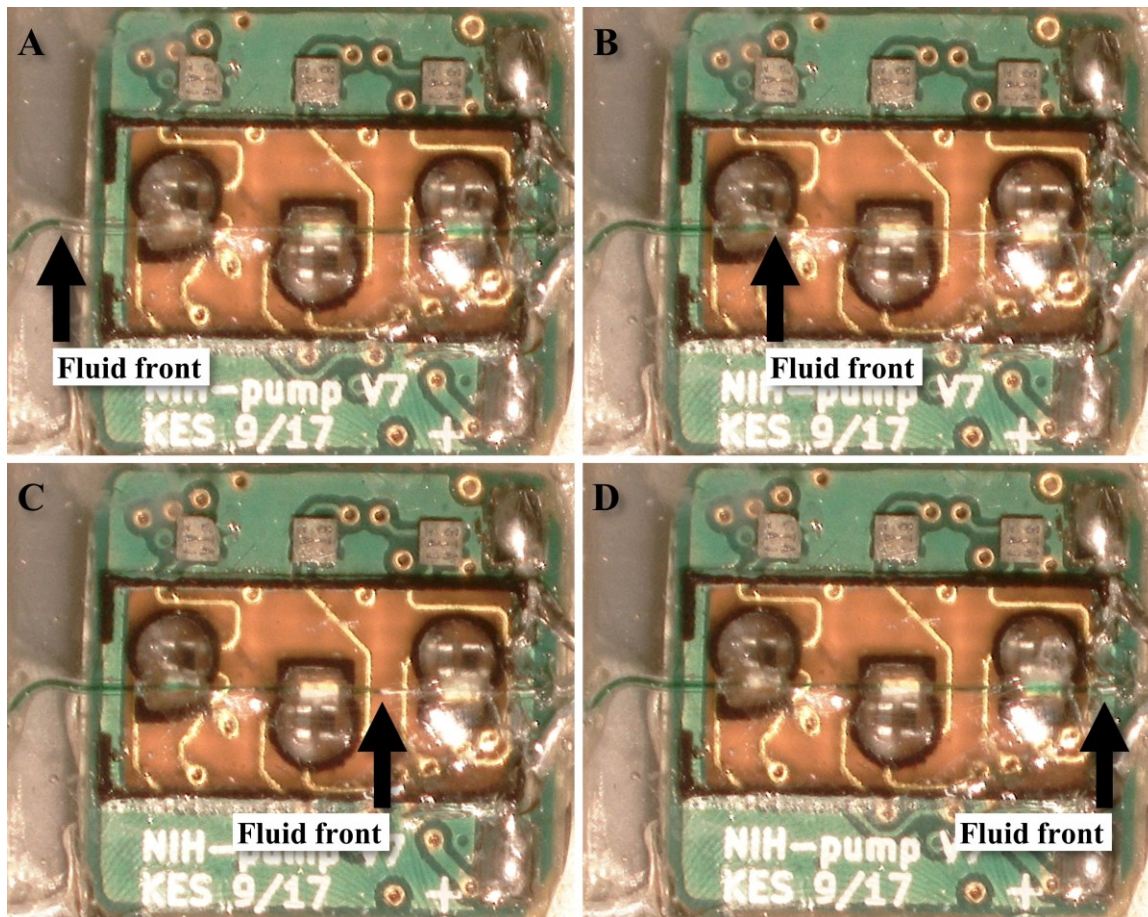
Figure 6.3. Self-priming of the micropump at 50 nL/min in presence of ~60 nL air bubble. A) t = 0, the bubble is introduced to the micropump. B) t = 20 s, the micropump sucks in the liquid. C) t = 40 s, the micropump pushes the fluid further toward downstream. D) t = 60 s, the micropump pushed the bubble toward the downstream completely.

6.5 Conclusion

The integrability of the microreservoir was demonstrated by building a microsystem consisted of the microreservoir and a recently developed micropump, designed and optimized for inner ear drug delivery. Two microsystems were implanted in the center of the upper back of two mice, and the outlet microtubing was implanted at the RWM niche. The drug delivery was performed following a protocol previously developed in our laboratory for infusion of salicylate using a syringe pump, while the auditory function was assessed using the DPOAE method. The *in vivo* results show that the mean value of changes in the DP threshold shift for the implanted microsystems matches the shifts caused by infusion with a syringe pump, demonstrating the suitability of the microreservoir to be integrated to a pumping mechanism for subcutaneously implanted active drug delivery systems. Further, long-term biocompatibility of an implanted microsystem in a mouse was tested, showing very favorable signs of biocompatibility for long-term implantation, along with the development of the fibrotic layer surrounding the microsystem. Finally, the ability of the micropump to drive the liquid in presence of bubbles much larger than maximum bubble size introduced during refills was explored. The results show successful pumping, demonstrating device capacity to operate in existence of bubbles that could be introduced to system during practical applications.

Chapter 7 Future work and final remarks

7.1 Introduction

The present work details design, fabrication, characterization, and implantation of an implantable microsystem for inner ear drug delivery. The microsystem consists a refillable microreservoir to store a drug and a micropump to deliver the drug from the reservoir to the target. The microreservoir was shown to provide near-zero backflow when the pumping mechanism is switched off, while it can operate with zero leakage after thousands of injections. The micropump was demonstrated to provide flow rates in the range of 10-100 nL/min in the presence of up to 10 times physiological backpressure and ± 3 °C fluctuation in the ambient temperature. The microsystem has been proven to be a robust drug delivery mechanism with *in vivo* experiments. As this work lays the foundation for many future studies that can build upon the success of the present work. This chapter provides detailed

146

future studies for technology enhancement and application extension of the microsystem or individual components, along with concluding remarks.

7.2 Technology enhancement

7.2.1 Normally-closed pumping mechanism

The current microsystem was intended to deliver the drug to RWM, which is a moist environment with atmospheric pressure. Therefore, the fluid in the microtubing does not experience backflow due to diffusion or advection. However, to avoid backflow and mixing the fluid in the microtubing for broader inner ear applications (e.g., cochleostomy) having a normally-closed fluidic path is substantially beneficial. To do so, a phase-change material can be developed that shrinks due to melting at a melting point higher than 37 °C. Using this material, as the micropump is working it propels the fluid similar to the current device, while after switching the pump off it will block the microtubing because of expansion due to solidification of the phase-change material. Therefore, it avoids advection when the pump is off.

Another way to achieve this goal is to develop a check valve or a normally-closed external valve in the downstream of the micropump. In microfluidics, usually, these normally-closed valves are designed to withstand high backpressures. In this application however

the valve requires to be leak-free at very low backpressures since the maximum physiological backpressures for mouse models are smaller than 0.53 kPa [186].

7.2.2 A single actuator micropump with check valves

The diameter of current microtubing (Micro-Renathane® Catheter Tubing, Braintree Scientific Inc., MA, USA) can be significantly modified by simultaneous heating and pulling [266]. This facilitates the implantation of the microtubing for RWM niche surgery. Besides, this feature enables using larger tubings at the micropump end, while in the pump downstream, the tubing diameter can be engineered. Having larger tubing at the micropump end enables tight-fitting of in-line check valves with larger diameters (e.g. 0.5-1 mm) in the microtubings.

Using a modified microtubing where the larger diameter is at the micropump end, and the smaller diameter is at the target delivery organ enables development of a micropump with a single phase-change actuator similar to the presented one in this work. Two in-line check valves on the sides rectify the flow. This proposed micropump reduces the power consumption per pumped fluid by reduction of number of actuators from three to one and implementing check valves in the fluidic path. Further, since there are check valves in the system there would be no backflow when the pump is switched off (see section 7.2.1). To reduce the chance of infection due to refill process, a filter between the refill port and the cavity area can be added. A port at the outlet plugs the micropump to a microtubing with

modified diameter in downstream. Primitive experiments demonstrated that a fitting without leakage at 200 kPa for 48 hrs is achievable.

Primitive experiments in our laboratory showed that dimensions of a tubing of 1.02 mm ID × 1.27 mm OD (MRE-050, Micro-Renathane® Catheter Tubing, Braintree Scientific Inc., MA, USA) can be reduced to as small as 40 µm ID × 50 µm OD. Utilizing Hagen–Poiseuille equation, for a flow rate of water at 100 nL/min (maximum flow rate for inner ear application) in a tubing of 40 µm ID and 10 cm length at 37 °C a pressure drop of ~1.9 kPa is expected. This pressure drop is smaller than the backpressure the presented peristaltic micropump can pump against with insignificant change in flow rate. This demonstrates demonstrating capability of the presented micropump to overcome this pressure, especially considering two check valves in the system. Figure 7.1 shows a schematic view of the proposed micropump.
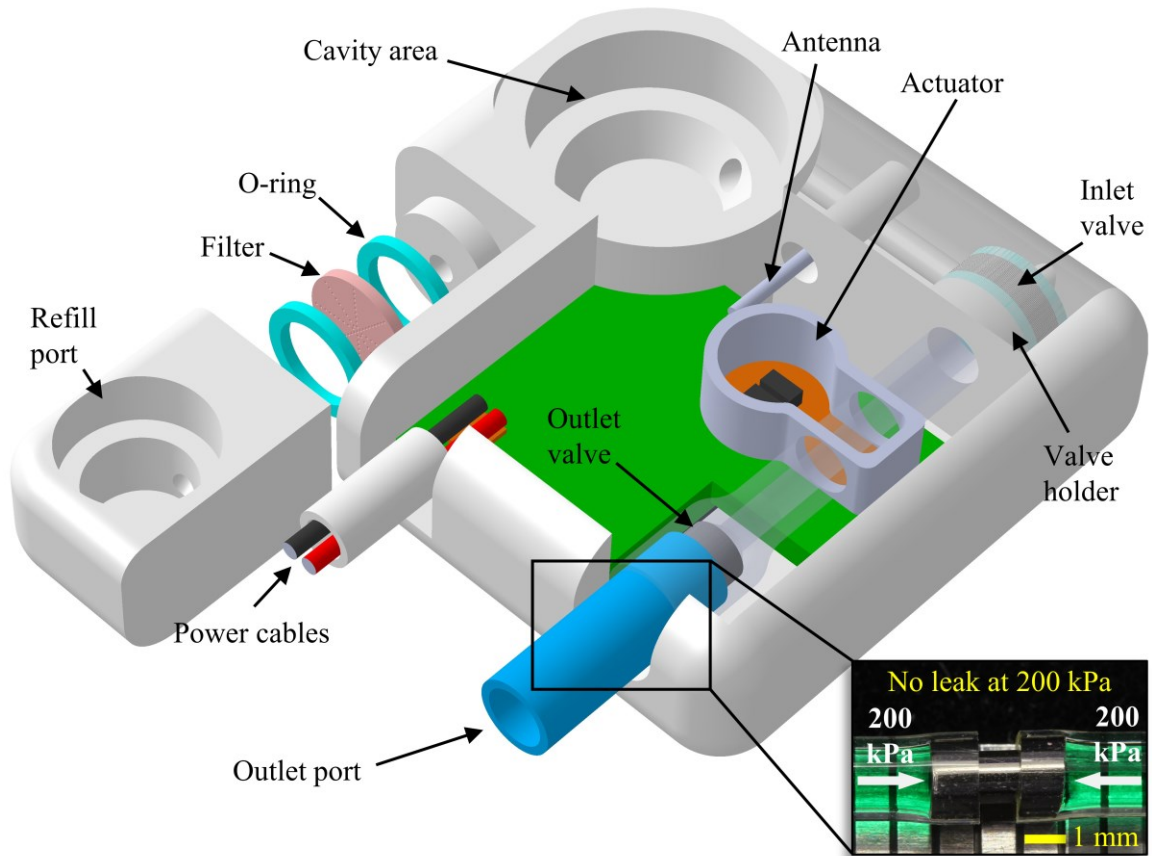
Figure 7.1. A schematic view of the proposed single actuator micropump with check valves. A filter between the refill port and the cavity area reduces possibilities of infections due to refills. One phase-change actuator pushes the microtubing and moves the working fluid, while two in-line check valves rectify the fluid flow in the microtubing. An outlet port connects the pump to a microtubing with a larger diameter in the micropump end and orders of magnitude smaller diameter in the downstream. Inset) A photograph of the fitting at the outlet port, which has been tested at 200 kPa for 48 hrs without leakage.

7.3 Application extension

7.3.1 Chronic drug delivery of Salicylate to the inner ear

The microsystem was shown to successfully deliver salicylate to RWM in acute experiments (see section 6.4.1). However, after one or two days of implantation, fibrosis occurs around the microsystem and the microtubing. To address this issue a mixture of dexamethasone and salicylate can reduce the possibility of microtubing clogging due to anti-fibrosis characteristics of dexamethasone [267]–[270]. Since fibrosis can occur in one day, delivery of small doses (0.5 µL) of the mixture once or twice a day may avoid the clogging at the tubing end. By resolving the fibrosis at the microtubing tip, the micropump can run for multiple days in a long-term application with different therapeutic compounds.

7.3.2 Pneumatic-driven pump for LOC applications

The cavity membrane of the microreservoir has been shown to induce near-zero backflow (and forward flow) when the pumping mechanism is switched off (see section 5.5.2). This feature enables precise control of the flow by applying certain pneumatic pressure on top of the membrane. This can be used for developing a pump for LOC applications, where a pneumatic force on top of the membrane drives the fluid ahead. A bubble trapper and a fluidic resistor can be used to assist in removing potential bubbles introduced to the system,

and controlling the flow rate, respectively [271], [272]. Figure 7.2 shows a schematic view of this pneumatic-driven pump.
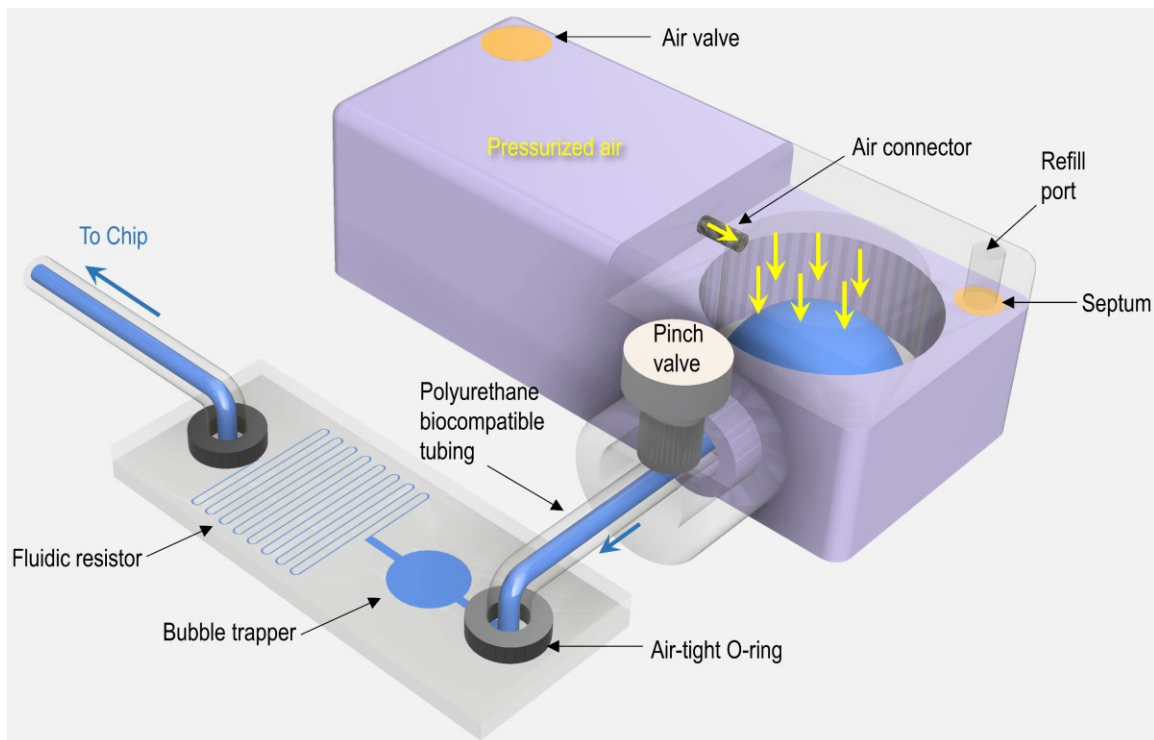
Figure 7.2. A schematic view of a Pneumatic-driven pump for LOC applications.

7.3.3 Pulse-free flow

Pulsatile flow has been described as 'intrinsic' property of peristaltic micropumps [273]. In the presented micropump actuation of each chamber results in a forward pulse, while the filling/loading phase of chamber 3 causes a backward pulse. Although the pulsatile flow of peristaltic micropumps have been shown to be beneficial in some LOC applications [274], in a case when the pump is desired to run continuously, it is impractical to modify the working mechanism to address it [273]. Therefore, the pulse can be minimized by adding a pulse dampener in the downstream of the micropump [273].

Pulse dampeners typically have a compliance element in the fluidic system that expands during a forward pulse and compress during a backward pulse, keeping the fluid flow at a near-constant rate. The compliance element can be a micromachined component [275] or deformable walls in microchannels [276]. A more widely used approach is to utilize compressible gasses such as air or Nitrogen, including the MASTERFLEX® L/S® pulse dampener (Cole-Parmer Instrument Company, USA), the pulse dampeners made with elastomer or plastomer membranes (Pulse- Guard Inc., USA), the ACCU-PULSE (Primary Fluid Systems Inc., Canada), stainless steel pulsation dampers (OLAER Fawcett Christie Ltd., UK), the bladder type made from different materials (Flowguard Ltd., UK), etc.

Although pulse-dampeners reduce the flow fluctuations they do not eliminate backflow, thus, they do not improve the pumping efficiency. Adding a check valve at the pump downstream, however, removes the backflow and consequently enhances the efficiency.

Since check valves do not eliminate forward pulse, integration of check valve and a pulse dampener at the pump downstream enables high-efficiency flow with minimized pulsation.

7.4 Conclusion

A fully implantable, scalable microsystem for inner drug delivery has been presented. The microsystem consists of a micropump and a microreservoir. The micropump is fabricated directly on top of a PCB, around a miniature microtubing (125 µm ID × 250 µm OD) providing a leak-free flow channel for the drug. The refillable microreservoir is capable of thousands of injections without leakage. Further the microreservoir is optimized to be integrated to a normally-open micropump by having near-zero backflow due to restoring force of the membrane.

Table 7.1 compares the presented microsystem with state of the art and commercially available microsystems for inner ear drug delivery. Compared to iPrecio® SMP-300 the presented microsystem has slightly less resolution in drug delivery, smaller reservoir capacity, and is normally-open. However, the presented device can be wirelessly controlled and programmed after implantation, with thousands of leak-free injections. Further, the presented microsystem is thin and light, with small footprint and tubing size, optimized for size-constrained applications such as mice inner ear drug delivery. Although presented here on the small murine cochlea, this low-cost design and fabrication methodology is scalable for use in larger animals and for clinical applications in children and adults. This device can potentially have other implantable biomedical applications, such as ocular drug delivery.

Table 7.1. Comparison of current microsystem with other state of the art and commercially available microsystems for inner ear drug delivery.

	Current device	iPrecio® SMP-300	Tandon et al. 2016 [13]
Flow rate range (nL/min)	10-100	0-166	4500-5500
Flow rate resolution (nL/min)	2.37	1.66	N/R
Wireless control	✓	✓	✗
Wireless programming	✓	✗	✗
Tubing OD (µm)	250	1500	360
Normally-closed	✗	✓	✓
Reservoir capacity (µL)	10	130	238
Max number of refills	~ 65000	N/R	N/A
Footprint (mm^3)	19 × 11	24.8 × 15	39.5 × 28.3
Thickness (mm)	3	7.2	7
Weight (g)	0.8	3.3	N/R
Mouse implantation	✓	✗	✗

References

[1]   "Deafness and hearing loss." [Online]. Available: http://www.who.int/mediacentre/factsheets/fs300/en/.

[2]   E. E. L. Pararas, D. A. Borkholder, and J. T. Borenstein, "Microsystems technologies for drug delivery to the inner ear," *Adv. Drug Deliv. Rev.*, vol. 64, no. 14, pp. 1650–1660, 2012.

[3]   M. C. Holley, "Keynote review: The auditory system, hearing loss and potential targets for drug development," *Drug Discovery Today*, vol. 10, no. 19. Elsevier Current Trends, pp. 1269–1282, 01-Oct-2005.

[4]   S. K. Juhn *et al.*, "The role of inflammatory mediators in the pathogenesis of otitis media and sequelae.," *Clin. Exp. Otorhinolaryngol.*, vol. 1, no. 3, pp. 117–38, Sep. 2008.

[5]   S. K. Juhn, B. A. Hunter, and R. M. Odland, "Blood-labyrinth barrier and fluid dynamics of the inner ear," in *International Tinnitus Journal*, 2001, vol. 7, no. 2, pp. 72–83.

[6]   D. S. Haynes, M. O'Malley, S. Cohen, K. Watford, and R. F. Labadie, "Intratympanic dexamethasone for sudden sensorineural hearing loss after failure of systemic therapy," *Laryngoscope*, vol. 117, no. 1, pp. 3–15, 2007.

[7]   E. Nuxoll and R. Siegel, "BioMEMS devices for drug delivery," *IEEE Eng. Med. Biol. Mag.*, vol. 28, no. 1, pp. 31–39, 2009.

[8]   D. A. Borkholder, "State-of-the-art mechanisms of intracochlear drug delivery," *Current Opinion in Otolaryngology and Head and Neck Surgery*, vol. 16, no. 5. pp. 472–477, Oct-2008.

[9]   O. Akil *et al.*, "Restoration of Hearing in the VGLUT3 Knockout Mouse Using Virally Mediated Gene Therapy," *Neuron*, vol. 75, no. 2, pp. 283–293, Jul. 2012.

[10]   M. Izumikawa *et al.*, "Auditory hair cell replacement and hearing improvement by Atoh1 gene therapy in deaf mammals," *Nat. Med.*, vol. 11, no. 3, pp. 271–276, 2005.

[11]   W. S. Kang *et al.*, "Non-Ototoxic Local Delivery of Bisphosphonate to the Mammalian Cochlea.," *Otol. Neurotol.*, vol. 36, no. 6, pp. 953–60, Jul. 2015.

[12]   K. Mizutari *et al.*, "Notch Inhibition Induces Cochlear Hair Cell Regeneration and Recovery of Hearing after Acoustic Trauma," *Neuron*, vol. 77, no. 1, pp. 58–69, Jan. 2013.

[13]   V. Tandon *et al.*, "Microfabricated reciprocating micropump for intracochlear drug delivery with integrated drug/fluid storage and electronically controlled dosing,"

Lab Chip, vol. 16, no. 5, pp. 829–846, 2016.

[14]   E. E. L. Swan, M. J. Mescher, W. F. Sewell, S. L. Tao, and J. T. Borenstein, "Inner ear drug delivery for auditory applications," *Adv. Drug Deliv. Rev.*, vol. 60, no. 15, pp. 1583–1599, 2008.

[15]   M. Schütz *et al.*, "The human deafness-associated connexin 30 T5M mutation causes mild hearing loss and reduces biochemical coupling among cochlear non-sensory cells in knock-in mice," *Hum. Mol. Genet.*, vol. 19, no. 24, pp. 4759–4773, Dec. 2010.

[16]   D. G. Johnson, "Integration Technologies For Implantable Microsystems by," 2013.

[17]   M. Thorne, A. N. Salt, J. E. DeMott, M. M. Henson, O. W. Henson, and S. L. Gewalt, "Cochlear Fluid Space Dimensions for Six Species Derived From Reconstructions of Three-Dimensional Magnetic Resonance Images," *Laryngoscope*, vol. 109, no. 10, pp. 1661–1668, Oct. 1999.

[18]   R. A. Buckingham and G. E. Valvassori, "Inner ear fluid volumes and the resolving power of magnetic resonance imaging: Can it differentiate endolymphatic structures?," *Ann. Otol. Rhinol. Laryngol.*, vol. 110, no. 2, pp. 113–117, Feb. 2001.

[19]   M. Igarashi, K. Ohashi, and M. Ishii, "Morphometric Comparison of Endolymphatic and Perilymphatic Spaces in Human Temporal Bones," *Acta Otolaryngol.*, vol. 101, no. 3–4, pp. 161–164, Jan. 1986.

[20]   A. Fridberger, J. T. van Maarseveen, E. Scarfone, M. Ulfendahl, B. Flock, and A. Flock, "Pressure-induced basilar membrane position shifts and the stimulus-evoked potentials in the low-frequency region of the guinea pig cochlea.," *Acta Physiol. Scand.*, vol. 161, no. 2, pp. 239–252, Sep. 1997.

[21]   E. E. L. Pararas *et al.*, "Kinetics of reciprocating drug delivery to the inner ear," *J. Control. Release*, vol. 152, no. 2, pp. 270–277, Jun. 2011.

[22]   K. Kawamoto, S.-H. Oh, S. Kanzaki, N. Brown, and Y. Raphael, "The Functional and Structural Outcome of Inner Ear Gene Transfer via the Vestibular and Cochlear Fluids in Mice," *Mol. Ther.*, vol. 4, no. 6, pp. 575–585, Dec. 2001.

[23]   A. Sclafani and J. I. Glendinning, "Flavor preferences conditioned in C57BL/6 mice by intragastric carbohydrate self-infusion," *Physiol. Behav.*, vol. 79, no. 4–5, pp. 783–788, Sep. 2003.

[24]   B. S. Carson *et al.*, "New approach to tumor therapy for inoperable areas of the brain chronic intraparenchymal drug delivery," *J. Neurooncol.*, vol. 60, no. 2, pp. 151–158, 2002.

[25]   D. A. Borkholder, X. Zhu, and R. D. Frisina, "Round window membrane

intracochlear drug delivery enhanced by induced advection," *J. Control. Release*, vol. 174, no. 1, pp. 171–176, 2014.

[26] Z. Chen *et al.*, "Inner ear drug delivery via a reciprocating perfusion system in the guinea pig," *J. Control. Release*, vol. 110, no. 1, pp. 1–19, 2005.

[27] J. Fiering *et al.*, "Local drug delivery with a self-contained, programmable, microfluidic system," *Biomed. Microdevices*, vol. 11, no. 3, pp. 571–578, Jun. 2009.

[28] M. J. Mescher *et al.*, "Fabrication methods and performance of low-permeability microfluidic components for a miniaturized wearable drug delivery system," *J. Microelectromechanical Syst.*, vol. 18, no. 3, pp. 501–510, Jun. 2009.

[29] D. A. Borkholder, X. Zhu, B. T. Hyatt, A. S. Archilla, W. J. Livingston, and R. D. Frisina, "Murine intracochlear drug delivery: Reducing concentration gradients within the cochlea," *Hear. Res.*, vol. 268, no. 1–2, pp. 2–11, 2010.

[30] M. J. Cima, "Microsystem Technologies for Medical Applications," *Annu. Rev. Chem. Biomol. Eng.*, vol. 2, no. 1, pp. 355–378, 2011.

[31] H. Orita, H. Shimogori, and H. Yamashita, "Unilateral intra-perilymphatic infusion of substance P enhances ipsilateral vestibulo-ocular reflex gains in the sinusoidal rotation test," *Neurosci. Lett.*, vol. 449, no. 3, pp. 207–210, Jan. 2009.

[32] H. Shimogori and H. Yamashita, "Efficacy of intracochlear administration of betamethasone on peripheral vestibular disorder in the guinea pig," *Neurosci. Lett.*, vol. 294, no. 1, pp. 21–24, Nov. 2000.

[33] A. A. Eshraghi, E. Adil, J. He, R. Graves, T. J. Balkany, and T. R. Van De Water, "Local dexamethasone therapy conserves hearing in an animal model of electrode insertion trauma-induced hearing loss," *Otol. Neurotol.*, vol. 28, no. 6, pp. 842–849, Sep. 2007.

[34] A. Salt, J. Hartsock, R. Gill, D. Smyth, J. Kirk, and K. Verhoeven, "Perilymph pharmacokinetics of marker applied through a cochlear implant in guinea pigs," *PLoS One*, vol. 12, no. 8, p. e0183374, Aug. 2017.

[35] V. Tandon *et al.*, "Microfabricated infuse-withdraw micropump component for an integrated inner-ear drug-delivery platform," *Biomed. Microdevices*, vol. 17, no. 2, 2015.

[36] A. Nisar, N. Afzulpurkar, B. Mahaisavariya, and A. Tuantranont, "MEMS-based micropumps in drug delivery and biomedical applications," *Sensors Actuators, B Chem.*, vol. 130, no. 2, pp. 917–942, 2008.

[37] D. G. Johnson and D. A. Borkholder, "Towards an implantable, low flow micropump that uses no power in the blocked-flow state," *Micromachines*, vol. 7,

no. 6, 2016.

[38] D. G. Johnson, R. D. Frisina, and D. A. Borkholder, "In-Plane Biocompatible Microfluidic Interconnects for Implantable Microsystems," *IEEE Trans. Biomed. Eng.*, vol. 58, no. 4, pp. 943–948, 2011.

[39] D. J. Laser and J. G. Santiago, "A review of micropumps," *J. Micromechanics Microengineering*, vol. 14, no. 6, pp. R35–R64, Jun. 2004.

[40] S. Shoji and M. Esashi, "Microflow devices and systems," *J. Micromechanics Microengineering*, vol. 4, no. 4, pp. 157–171, 1994.

[41] N.-T. Nguyen, X. Huang, and T. K. Chuan, "MEMS-Micropumps: A Review," *J. Fluids Eng.*, vol. 124, no. 2, p. 384, 2002.

[42] P. Goswami, J. Chakraborty, A. Bandopadhyay, and S. Chakraborty, "Electrokinetically modulated peristaltic transport of power-law fluids," *Microvasc. Res.*, vol. 103, pp. 41–54, 2016.

[43] W. Kim and J. W. M. Bush, "Natural drinking strategies," *J. Fluid Mech.*, vol. 705, pp. 7–25, Aug. 2012.

[44] A. Bandopadhyay, D. Tripathi, and S. Chakraborty, "Electroosmosis-modulated peristaltic transport in microfluidic channels," *Phys. Fluids*, vol. 28, no. 5, 2016.

[45] A. Loth and R. Forster, "Disposable high pressure peristaltic micro pump for standalone and on-chip applications," in *2016 IEEE 11th Annual International Conference on Nano/Micro Engineered and Molecular Systems, NEMS 2016*, 2016, pp. 29–33.

[46] B. D. Iverson and S. V. Garimella, "Recent advances in microscale pumping technologies: A review and evaluation," *Microfluid. Nanofluidics*, vol. 5, no. 2, pp. 145–174, 2008.

[47] T. S. Leu, D. C. Gong, and D. Pan, "Numerical and experimental studies of phase difference effects on flow rate of peristaltic micro-pumps with pumping chambers in series configurations," *Microsyst. Technol.*, vol. 23, no. 2, pp. 329–341, 2017.

[48] J. G. Smits, "Piezoelectric micropump with three valves working peristaltically," *Sensors Actuators A Phys.*, vol. 21, no. 1–3, pp. 203–206, Feb. 1990.

[49] S.-Y. Yang, S.-K. Hsiung, Y.-C. Hung, C.-M. Chang, T.-L. Liao, and G.-B. Lee, "A cell counting/sorting system incorporated with a microfabricated flow cytometer chip," *Meas. Sci. Technol.*, vol. 17, no. 7, p. 2001, 2006.

[50] D. Sabourin *et al.*, "The MainSTREAM Component Platform: A Holistic Approach to Microfluidic System Design," *J. Lab. Autom.*, vol. 18, no. 3, pp. 212–228, 2013.

[51] I. Lee, P. Hong, C. Cho, B. Lee, K. Chun, and B. Kim, "Four-electrode micropump with peristaltic motion," *Sensors Actuators, A Phys.*, vol. 245, pp. 19–25, 2016.

[52] A. Nightingale, G. W. H. Evans, P. Xu, B. J. Kim, S. Hassan, and X. Niu, "Phased peristaltic micropumping for continuous sampling and hardcoded droplet generation," *Lab Chip*, 2017.

[53] Y. Cheng, Y. Wang, Z. Ma, W. Wang, and X.-Y. Ye, "Bubble- and clogging-free microfluidic particle separation platform with multi-filtration," *Lab Chip*, vol. 16, pp. 4517–4526, 2016.

[54] T. F. Didar, K. Li, M. Tabrizian, and T. Veres, "High throughput multilayer microfluidic particle separation platform using embedded thermoplastic-based micropumping.," *Lab Chip*, vol. 13, no. 13, pp. 2615–22, 2013.

[55] Y. Cheng, X. Ye, Z. Ma, S. Xie, and W. Wang, "High-throughput and clogging-free microfluidic filtration platform for on-chip cell separation from undiluted whole blood," *Biomicrofluidics*, vol. 10, no. 1, p. 014118, Jan. 2016.

[56] M. Busek, K. Hofmann, U. Grätz, and F. Sonntag, "Pneumatically Actuated Peristaltic Micropump – Characterized With Mpiv and Modelled Using Simulationx," pp. 1–4, 2014.

[57] Y. C. Hsu, S. J. Lin, and C. C. Hou, "Development of peristaltic antithrombogenic micropumps for in vitro and ex vivo blood transportation tests," *Microsyst. Technol.*, vol. 14, no. 1, pp. 31–41, 2008.

[58] C. H. Weng, W. M. Yeh, K. C. Ho, and G. Bin Lee, "A microfluidic system utilizing molecularly imprinted polymer films for amperometric detection of morphine," *Sensors Actuators, B Chem.*, vol. 121, no. 2, pp. 576–582, 2007.

[59] Y. Bar-cohen and Z. Chatig, "Piezoelectrically Actuated Miniature Peristaltic Pump," *Jet Propuls. Lab.*, vol. 3992, no. I, pp. 669–676, 2001.

[60] C. H. Wang and G. Bin Lee, "Automatic bio-sampling chips integrated with micro-pumps and micro-valves for disease detection," *Biosens. Bioelectron.*, vol. 21, no. 3, pp. 419–425, 2005.

[61] a. Doll, M. Heinrichs, F. Goldschmidtboeing, H. J. Schrag, U. T. Hopt, and P. Woias, "A high performance bidirectional micropump for a novel artificial sphincter system," *Sensors Actuators, A Phys.*, vol. 130–131, no. SPEC. ISS., pp. 445–453, 2006.

[62] M. Busek, M. Nötzel, C. Polk, and F. Sonntag, "Characterization and simulation of peristaltic micropumps," *J. Sensors Sens. Syst.*, vol. 2, no. 2, pp. 165–169, 2013.

[63] U. Marx *et al.*, "'Human-on-a-chip' developments: A translational cuttingedge

alternative to systemic safety assessment and efficiency evaluation of substances in laboratory animals and man?," *ATLA Altern. to Lab. Anim.*, vol. 40, no. 5, pp. 235–257, 2012.

[64]   F. Sonntag *et al.*, "Design and prototyping of a chip-based multi-micro-organoid culture system for substance testing, predictive to human (substance) exposure," *J. Biotechnol.*, vol. 148, no. 1, pp. 70–75, 2010.

[65]   I. Wagner *et al.*, "A dynamic multi-organ-chip for long-term cultivation and substance testing proven by 3D human liver and skin tissue co-culture," *Lab Chip*, vol. 13, no. 18, pp. 3538–3547, 2013.

[66]   P. Skafte-Pedersen, D. Sabourin, M. Dufva, and D. Snakenborg, "Multi-channel peristaltic pump for microfluidic applications featuring monolithic PDMS inlay.," *Lab Chip*, vol. 9, no. 20, pp. 3003–3006, 2009.

[67]   K. W. Oh, R. Rong, and C. H. Ahn, "Miniaturization of pinch-type valves and pumps for practical micro total analysis system integration," *J. Micromechanics Microengineering*, vol. 15, no. 12, pp. 2449–2455, 2005.

[68]   L. Cao, S. Mantell, and D. Polla, "Design and simulation of an implantable medical drug delivery system using microelectromechanical systems technology," *Sensors Actuators, A Phys.*, vol. 94, no. 1–2, pp. 117–125, 2001.

[69]   A. Geipel, F. Goldschmidtboeing, P. Jantscheff, N. Esser, U. Massing, and P. Woias, "Design of an implantable active microport system for patient specific drug release," *Biomed. Microdevices*, vol. 10, no. 4, pp. 469–478, 2008.

[70]   P. H. Cazorla *et al.*, "Piezoelectric micro-pump with PZT thin film for low consumption microfluidic devices," *Procedia Eng.*, vol. 87, pp. 488–491, 2014.

[71]   P. H. Cazorla *et al.*, "Integration of PZT thin films on a microfluidic complex system," *IEEE Int. Ultrason. Symp. IUS*, pp. 491–494, 2014.

[72]   P. H. Cazorla *et al.*, "A low voltage silicon micro-pump based on piezoelectric thin films," *Sensors Actuators, A Phys.*, vol. 250, pp. 35–39, 2016.

[73]   F. Forouzandeh *et al.*, "A nanoliter resolution implantable micropump for murine inner ear drug delivery," *J. Control. Release*, vol. 298, no. January, pp. 27–37, 2019.

[74]   K. B. Vinayakumar, G. Nadiger, V. R. Shetty, N. S. Dinesh, M. M. Nayak, and K. Rajanna, "Packaged peristaltic micropump for controlled drug delivery application," *Rev. Sci. Instrum.*, vol. 88, no. 1, p. 015102, 2017.

[75]   G. Traverso *et al.*, "Microneedles for drug delivery via the gastrointestinal tract," *J. Pharm. Sci.*, vol. 104, no. 2, pp. 362–367, 2015.

[76] A. Geipel *et al.*, "A novel two-stage backpressure-independent micropump: modeling and characterization," *J. Micromechanics Microengineering*, vol. 17, no. 5, pp. 949–959, 2007.

[77] Q. Lin, B. Yang, J. Xie, and Y.-C. Tai, "Dynamic simulation of a peristaltic micropump considering coupled fluid flow and structural motion," *J. Micromechanics Microengineering*, vol. 17, no. 2, pp. 220–228, 2006.

[78] L. S. Jang *et al.*, "A stand-alone peristaltic micropump based on piezoelectric actuation," *Biomed. Microdevices*, vol. 9, no. 2, pp. 185–194, 2007.

[79] J. M. Berg, R. Anderson, M. Anaya, B. Lahlouh, M. Holtz, and T. Dallas, "A two-stage discrete peristaltic micropump," *Sensors Actuators, A Phys.*, vol. 104, no. 1, pp. 6–10, 2003.

[80] P. Woias, "Micropumps - Past, progress and future prospects," *Sensors Actuators, B Chem.*, vol. 105, no. 1, pp. 28–38, 2005.

[81] A. K. Au, H. Lai, B. R. Utela, and A. Folch, *Microvalves and micropumps for BioMEMS*, vol. 2, no. 2. 2011.

[82] F. Amirouche, Y. Zhou, and T. Johnson, "Current micropump technologies and their biomedical applications," *Microsyst. Technol.*, vol. 15, no. 5, pp. 647–666, 2009.

[83] M. Du, Z. Ma, X. Ye, and Z. Zhou, "On-chip fast mixing by a rotary peristaltic micropump with a single structural layer," *Sci. China Technol. Sci.*, vol. 56, no. 4, pp. 1047–1054, 2013.

[84] C. Chen, S. Shih, and C. Hsu, "Fabrication of a Peristaltic Micropump with UV Curable Adhesive," *Proc. 3rd Int. Conf. Intell. Technol. Eng. Syst.*, vol. 293, pp. 119–125, 2016.

[85] C.-H. Chiou, T.-Y. Yeh, and J.-L. Lin, "Deformation Analysis of a Pneumatically-Activated Polydimethylsiloxane (PDMS) Membrane and Potential Micro-Pump Applications," *Micromachines*, vol. 6, no. 2, pp. 216–229, 2015.

[86] S. A. M. Shaegh *et al.*, "Plug-and-play microvalve and micropump for rapid integration with microfluidic chips," *Microfluid. Nanofluidics*, vol. 19, no. 3, pp. 557–564, 2015.

[87] W. Zhang and R. E. Eitel, "An Integrated Multilayer Ceramic Piezoelectric Micropump for Microfluidic Systems," *J. Intell. Mater. Syst. Struct.*, vol. 24, no. 13, pp. 1637–1646, 2013.

[88] R. Kant, H. Singh, M. Nayak, and S. Bhattacharya, "Optimization of design and characterization of a novel micro-pumping system with peristaltic motion," *Microsyst. Technol.*, vol. 19, no. 4, pp. 563–575, 2013.

[89]   N. T. Nguyen and X. Huang, "Miniature valveless pumps based on printed circuit board technique," *Sensors Actuators, A Phys.*, vol. 88, no. 2, pp. 104–111, 2001.

[90]   J. Cui and T. Pan, "A vacuum-driven peristaltic micropump with valved actuation chambers," *J Micromech Microeng*, vol. 21, no. 6, p. 065034, 2011.

[91]   F. Sassa, Y. Al-Zain, T. Ginoza, S. Miyazaki, and H. Suzuki, "Miniaturized shape memory alloy pumps for stepping microfluidic transport," *Sensors Actuators, B Chem.*, vol. 165, no. 1, pp. 157–163, 2012.

[92]   C. Grosjean and Y. Tai, "A thermopneumatic peristaltic micropump," *Proc. Transducer*, 1999.

[93]   M. Wackerle, M. Richter, A. Drost, U. Schaber, and D. H. J. Bigus, "A bidirectional micro pump for the handling of liquids and gases," in *Procdings: ACTUATOR 2004; 9th International Conference on New Actuators*, 2004, pp. 216–219.

[94]   J. Judy, T. Tamagawa, and D. L. Polla, "Surface-machined micromechanical membrane pump," *[1991] Proceedings. IEEE Micro Electro Mech. Syst.*, pp. 182–186, 1991.

[95]   J. Xie and J. Shih, "Integrated Parylene Electrostatic peristaltic pump," pp. 0–3, 2003.

[96]   F. Goldschmidtböing, A. Doll, M. Heinrichs, P. Woias, H.-J. Schrag, and U. T. Hopt, "A generic analytical model for micro-diaphragm pumps with active valves," *J. Micromechanics Microengineering*, vol. 15, no. 4, pp. 673–683, 2005.

[97]   M. Q. Bu, M. Tracy, G. Ensell, J. S. Wilkinson, and A. G. R. Evans, "Design and theoretical evaluation of a novel microfluidic device to be used for PCR," *J. Micromechanics Microengineering*, vol. 13, no. 4, pp. S125–S130, 2003.

[98]   C.-W. Huang, S.-B. Huang, and G.-B. Lee, "Pneumatic micropumps with serially connected actuation chambers," *J. Micromechanics Microengineering*, vol. 16, no. 11, pp. 2265–2272, 2006.

[99]   C.-H. Wang and G.-B. Lee, "Pneumatically driven peristaltic micropumps utilizing serpentine-shape channels," *J. Micromechanics Microengineering*, vol. 16, no. 2, pp. 341–348, 2006.

[100]   H. So, A. P. Pisano, and Y. H. Seo, "Caterpillar locomotion-inspired valveless pneumatic micropump using a single teardrop-shaped elastomeric membrane," *Lab Chip*, vol. 14, no. 13, pp. 2240–2248, 2014.

[101]   H. So, Y. H. Seo, and A. P. Pisano, "Refillable and magnetically actuated drug delivery system using pear-shaped viscoelastic membrane," *Biomicrofluidics*, vol. 8, no. 4, p. 044119, 2014.

[102] K. Nakahara, M. Yamamoto, Y. Okayama, K. Yoshimura, K. Fukagata, and N. Miki, "A peristaltic micropump using traveling waves on a polymer membrane," *J. Micromechanics Microengineering*, vol. 23, no. 8, p. 085024, Aug. 2013.

[103] K. Nakahara, K. Yoshimura, Y. Okayama, and N. Miki, "A peristaltic micropump using traveling waves of polymer membranes driven by a single actuator," *Proc. IEEE Int. Conf. Micro Electro Mech. Syst.*, pp. 1083–1086, 2011.

[104] B. Pečar, D. Križaj, D. Vrtačnik, D. Resnik, T. Dolžan, and M. Možek, "Piezoelectric peristaltic micropump with a single actuator," *J. Micromechanics Microengineering*, vol. 24, no. 10, p. 105010, 2014.

[105] B. Pečar *et al.*, "A strip-type microthrottle pump: Modeling, design and fabrication," *Sensors (Switzerland)*, vol. 13, no. 3, pp. 3092–3108, 2013.

[106] V. Shkolnikov, J. Ramunas, and J. G. Santiago, "A self-priming, roller-free, miniature, peristaltic pump operable with a single, reciprocating actuator," *Sensors Actuators, A Phys.*, vol. 160, no. 1–2, pp. 141–146, 2010.

[107] H. Lai and A. Folch, "Design and dynamic characterization of 'single-stroke' peristaltic PDMS micropumps.," *Lab Chip*, vol. 11, no. 2, pp. 336–342, 2011.

[108] J. Shao *et al.*, "Integrated microfluidic chip for endothelial cells culture and analysis exposed to a pulsatile and oscillatory shear stress," *Lab Chip*, vol. 9, no. 21, pp. 3118–3125, 2009.

[109] G. Beckers and B. Dehez, "Design and modeling of a quasi-static peristaltic piezoelectric micropump," *2013 Int. Conf. Electr. Mach. Syst. ICEMS 2013*, no. Immc, pp. 1301–1306, 2013.

[110] Y. Y. Tsui and T. C. Chang, "A novel peristaltic micropump with low compression ratios," *Int. J. Numer. Methods Fluids*, vol. 69, no. 8, pp. 1363–1376, Jul. 2012.

[111] Y. C. Hsu and N. B. Le, "Equivalent electrical network for performance characterization of piezoelectric peristaltic micropump," *Microfluid. Nanofluidics*, vol. 7, no. 2, pp. 237–248, 2009.

[112] B. D. Wackerle M, Richter M, Drost A, Schaber U, "A bidirectional micro pump for the handling of liquids and gases," in *ACTUATOR 2004; 9th International Conference on New Actuators 2004*, 2004, pp. 216–219.

[113] Y.-J. Yang and H.-H. Liao, "Development and characterization of thermopneumatic peristaltic micropumps," *J. Micromechanics Microengineering*, vol. 19, no. 2, p. 025003, 2009.

[114] C. Koch, V. Remcho, and J. Ingle, "PDMS and tubing-based peristaltic micropumps with direct actuation," *Sensors Actuators, B Chem.*, vol. 135, no. 2, pp. 664–670,

2009.

[115] C.-W. Huang, S.-B. Huang, and G.-B. Lee, "Pneumatic micropumps with serially connected actuation chambers," *J. Micromechanics Microengineering*, vol. 16, no. 11, pp. 2265–2272, 2006.

[116] D. S. Lee, J. S. Ko, and Y. T. Kim, "Bidirectional pumping properties of a peristaltic piezoelectric micropump with simple design and chemical resistance," *Thin Solid Films*, vol. 468, no. 1–2, pp. 285–290, 2004.

[117] L. Yobas, K.-C. Tang, S.-E. Yong, and E. Kye-Zheng Ong, "A disposable planar peristaltic pump for lab-on-a-chip.," *Lab Chip*, vol. 8, no. 5, pp. 660–2, 2008.

[118] S.-B. Huang, M.-H. Wu, Z. Cui, Z. Cui, and G.-B. Lee, "A membrane-based serpentine-shape pneumatic micropump with pumping performance modulated by fluidic resistance," *J. Micromechanics Microengineering*, vol. 18, no. 4, p. 045008, 2008.

[119] J. Xiang, Z. Cai, Y. Zhang, and W. Wang, "A micro-cam actuated linear peristaltic pump for microfluidic applications," *Sensors Actuators, A Phys.*, vol. 251, pp. 20–25, 2016.

[120] K. S. Lee, B. Kim, and M. A. Shannon, "An electrostatically driven valve-less peristaltic micropump with a stepwise chamber," *Sensors Actuators, A Phys.*, vol. 187, pp. 183–189, 2012.

[121] J. Goulpeau, D. Trouchet, A. Ajdari, and P. Tabeling, "Experimental study and modeling of polydimethylsiloxane peristaltic micropumps," *J. Appl. Phys.*, vol. 98, no. 4, 2005.

[122] O. C. Jeong and S. Konishi, "Fabrication of a peristaltic micro pump with novel cascaded actuators," *J. Micromechanics Microengineering*, vol. 18, no. 2, p. 025022, 2008.

[123] D. S. Lee, H. C. Yoon, and J. S. Ko, "Fabrication and characterization of a bidirectional valveless peristaltic micropump and its application to a flow-type immunoanalysis," *Sensors Actuators, B Chem.*, vol. 103, no. 1–2, pp. 409–415, 2004.

[124] T. Pan, E. Kai, M. Stay, V. Barocas, and B. Ziaie, "A magnetically driven PDMS peristaltic micropump.," *Conf. Proc. IEEE Eng. Med. Biol. Soc.*, vol. 4, pp. 2639–2642, 2004.

[125] N. J. Graf and M. T. Bowser, "A soft-polymer piezoelectric bimorph cantilever-actuated peristaltic micropump.," *Lab Chip*, vol. 8, no. 10, pp. 1664–70, 2008.

[126] L. S. Jang and W. H. Kan, "Peristaltic piezoelectric micropump system for

166

biomedical applications," *Biomed. Microdevices*, vol. 9, no. 4, pp. 619–626, 2007.

[127] L. S. Jang, K. Shu, Y. C. Yu, Y. J. Li, and C. H. Chen, "Effect of actuation sequence on flow rates of peristaltic micropumps with PZT actuators," *Biomed. Microdevices*, vol. 11, no. 1, pp. 173–181, 2009.

[128] L. S. Jang and Y. C. Yu, "Peristaltic micropump system with piezoelectric actuators," *Microsyst. Technol.*, vol. 14, no. 2, pp. 241–248, 2008.

[129] K. S. Lee, B. Kim, and M. a Shannon, "Development of a peristaltic gas micropump with a single chamber and multiple electrodes," *J. Micromechanics Microengineering*, vol. 23, no. 9, p. 095006, 2013.

[130] S. N. S. Na, S. Ridgeway, and L. C. L. Cao, "Theoretical and experimental study of fluid behavior of a peristaltic micropump," *Proc. 15th Bienn. Univ. Ind. Microelectron. Symp. (Cat. No.03CH37488)*, pp. 2–6, 2003.

[131] B. Husband, M. Bu, V. Apostolopoulos, T. Melvin, and A. G. R. Evans, "Novel actuation of an integrated peristaltic micropump," *Microelectron. Eng.*, vol. 73–74, pp. 858–863, 2004.

[132] B. Husband, M. Bu, a G. R. Evans, and T. Melvin, "Investigation for the operation of an integrated peristaltic micropump," *J. Micromechanics Microengineering*, vol. 14, no. 9, pp. S64–S69, 2004.

[133] W. Gu, X. Zhu, N. Futai, B. S. Cho, and S. Takayama, "Computerized microfluidic cell culture using elastomeric channels and Braille displays," *Proc. Natl. Acad. Sci. U. S. A.*, vol. 101, no. 45, pp. 15861–15866, 2004.

[134] N. Futai, W. Gu, J. W. Song, and S. Takayama, "Handheld recirculation system and customized media for microfluidic cell culture," *Lab Chip*, vol. 6, no. 1, pp. 149–154, 2006.

[135] A. Geipel *et al.*, "Pressure-Independent Micropump with Piezoelectric Valves for Low Flow Drug Delivery Systems," *19th IEEE Int. Conf. Micro Electro Mech. Syst.*, no. January, pp. 786–789, 2006.

[136] F. Trenkle, S. Haeberle, and R. Zengerle, "Normally-closed peristaltic micropump with re-usable actuator and disposable fluidic chip," *Sensors Actuators, B Chem.*, vol. 154, no. 2, pp. 137–141, 2011.

[137] A. Richter, S. Klatt, G. Paschew, and C. Klenke, "Micropumps operated by swelling and shrinking of temperature-sensitive hydrogels.," *Lab Chip*, vol. 9, no. 4, pp. 613–618, 2009.

[138] E. Kai, T. Pan, and B. Ziaie, "a Robust Low-cost Pdms Peristaltic Micropump," vol. 2, pp. 270–273, 2004.

[139] A. Hatch, A. E. Kamholz, G. Holman, P. Yager, and K. F. Böhringer, "A ferrofluidic magnetic micropump," *J. Microelectromechanical Syst.*, vol. 10, no. 2, pp. 215–221, 2001.

[140] E. G. Kim, W. C. Sim, J. Oh, and B. Choi, "A continuous peristaltic micropump using magnetic fluid," *2nd Annu. Int. IEEE-EMBS Spec. Top. Conf. Microtechnologies Med. Biol. - Proc.*, pp. 509–513, 2002.

[141] E. Kim, J. Oh, and B. Choi, "A study on the development of a continuous peristaltic micropump using magnetic fluids," *Sensors Actuators A. Phys.*, vol. 128, pp. 43–51, 2006.

[142] M. Du, X. Ye, K. Wu, and Z. Zhou, "A Peristaltic Micro Pump Driven by a Rotating Motor with Magnetically Attracted Steel Balls," *Sensors*, vol. 9, no. 4, pp. 2611–2620, Jan. 2009.

[143] K. Lim, S. Kim, and J. H. Hahn, "Roller-type squeezing pump with picoliter handling capability," *Sensors Actuators, B Chem.*, vol. 92, no. 1–2, pp. 208–214, 2003.

[144] T. Tan, S. W. Watts, and R. P. Davis, "Drug delivery: Enabling technology for drug discovery and development. iPRECIO® Micro Infusion Pump: programmable, refillable, and implantable," *Front. Pharmacol.*, vol. JUL, p. 44, Aug. 2011.

[145] C. Abe, T. Tashiro, K. Tanaka, R. Ogihara, and H. Morita, "A novel type of implantable and programmable infusion pump for small laboratory animals," *J. Pharmacol. Toxicol. Methods*, vol. 59, no. 1, pp. 7–12, 2009.

[146] "Infusion Pumps for Small Laboratory Animals." [Online]. Available: https://www.alnmag.com/article/2009/05/infusion-pumps-small-laboratory-animals. [Accessed: 18-May-2018].

[147] "iPRECIO®." .

[148] X. Zhang, Z. Chen, and Y. Huang, "A valve-less microfluidic peristaltic pumping method," *Biomicrofluidics*, vol. 9, no. 1, pp. 1–8, 2015.

[149] O. C. Jeong and S. Konishi, "Fabrication and drive test of pneumatic PDMS micro pump," *Sensors Actuators, A Phys.*, vol. 135, no. 2, pp. 849–856, 2007.

[150] M. C. Cole, A. V. Desai, and P. J. A. Kenis, "Two-layer multiplexed peristaltic pumps for high-density integrated microfluidics," *Sensors Actuators, B Chem.*, vol. 151, no. 2, pp. 384–393, 2011.

[151] M. M. Teymoori and E. A. Abbaspour-Sani, "A novel electrostatic micromachined pump for drug delivery systems," *ICONIP '02. Proc. 9th Int. Conf. Neural Inf. Process. Comput. Intell. E-Age (IEEE Cat. No.02EX575)*, pp. 105–109, 2002.

[152] M. M. Teymoori and E. Abbaspour-Sani, "Design and simulation of a novel electrostatic peristaltic micromachined pump for drug delivery applications," *Sensors Actuators, A Phys.*, vol. 117, no. 2, pp. 222–229, 2005.

[153] J. Xie, J. Shih, Q. Lin, B. Yang, and Y.-C. Tai, "Surface micromachined electrostatically actuated micro peristaltic pump.," *Lab Chip*, vol. 4, no. 5, pp. 495–501, 2004.

[154] M. Patrascu, J. Gonzalo-Ruiz, M. Goedbloed, M. Crego-Calama, and S. H. Brongersma, "Design, fabrication and characterization of electrostatic micro actuators for microfluidic platforms," *Procedia Eng.*, vol. 25, pp. 1181–1184, 2011.

[155] M. Patrascu, J. Gonzalo-Ruiz, M. Goedbloed, S. H. Brongersma, and M. Crego-Calama, "Flexible, electrostatic microfluidic actuators based on thin film fabrication," *Sensors Actuators, A Phys.*, vol. 186, pp. 249–256, 2012.

[156] M. Patrascu, M. Crego-Calama, S. H. Brongersma, and J. de Boeck, "Novel approach for physical modeling of microfluidic systems," *Proc. Asme Int. Mech. Eng. Congr. Expo. 2007, Vol 4*, pp. 247-255\r257, 2008.

[157] L. Maffli, B. O'Brien, S. Rosset, and H. Shea, "Pump it up," *Proc. SPIE*, vol. 8340, no. Figure 1, p. 83402Q, 2012.

[158] H. Kim, A. Astle, K. Najafi, … L. B.-, 2007. MEMS. IEEE, and U. 2007, "A fully integrated high-efficiency peristaltic 18-stage gas micropump with active microvalves," *ieeexplore.ieee.orgSign in*.

[159] S. Lee, S. Y. Yee, A. Besharatian, H. Kim, L. R. Bernal, and K. Najafi, "ADAPTIVE GAS PUMPING BY CONTROLLED TIMING OF ACTIVE MICROVALVES IN PERISTALTIC MICROPUMPS Center for Wireless Integrated Microsystems (WIMS) University of Michigan , Ann Arbor , MI , USA . MULTI-STAGE MICROPUMP : dV dm V + P = RT dt dt," pp. 2294–2297, 2009.

[160] A. A. Astle, H. S. Kim, L. P. Bernal, K. Najafi, and P. D. Washabaugh, "Theoretical and experimental performance of a high frequency gas micropump," *Sensors Actuators A Phys.*, vol. 134, no. 1, pp. 245–256, Feb. 2007.

[161] K. Kumar, L. Bernal, … S. Y.-A. 2011, and U. 2011, "Transient Performance and Coupled Acoustic Structural and Electrostatic Modeling of a Multistage Vacuum Micropump," *… .asmedigitalcollection.asme.orgSign*, pp. 287–296, Jan. 2011.

[162] A. Besharatian, K. Kumar, R. L. Peterson, L. P. Bernal, and K. Najafi, "A scalable, modular, multi-stage, peristaltic, electrostatic gas micro-pump," *Proc. IEEE Int. Conf. Micro Electro Mech. Syst.*, no. February, pp. 1001–1004, 2012.

[163] H. Kim, A. a Astle, K. Najafi, L. P. Bernal, and P. D. Washabaugh, "Integrated Peristaltic 18-Stage Electrostatic Gas Micro Pump With Active Microvalves," *Hilt.*

Head, vol. 24, no. 1, pp. 292–295, 2015.

[164] H. Kim, A. A. Astle, K. Najafi, L. P. Bernal, and P. D. Washabaugh, "An integrated electrostatic peristaltic 18-stage gas micropump with active microvalves," *J. Microelectromechanical Syst.*, vol. 24, no. 1, pp. 192–206, 2015.

[165] B. Kim, K. S. Lee, and M. A. Shannon, "An electrostatically driven peristaltic micropump with an indium tin oxide electrode," *8th Annu. IEEE Int. Conf. Nano/Micro Eng. Mol. Syst. IEEE NEMS 2013*, vol. 1, pp. 927–930, 2013.

[166] K. S. Lee *et al.*, "An electrostatically driven double-sided one-chamber peristaltic pump with four electrodes," *Jpn. J. Appl. Phys.*, vol. 52, no. 6s, p. 06GL05, 2013.

[167] S. Y. Jeong, C. S. Cho, P. H. Hong, D. S. Lee, and B. H. Kim, "Peristaltic Micropump with Multi-Electrodes Using Electrostatic Force," *Adv. Mater. Res.*, vol. 1125, pp. 571–576, Oct. 2015.

[168] J. a. Folta, N. F. Raley, and E. W. Hee, "Design, fabrication and testing of a miniature peristaltic membrane pump," *Technical Digest IEEE Solid-State Sensor and Actuator Workshop*. 1992.

[169] M. Knight and J. House, "Design, fabrication, and test of a peristaltic micropump," *Microsyst. Technol.*, vol. 10, no. 5, pp. 426–431, 2004.

[170] O. C. Jeong, S. W. Park, S. S. Yang, and J. J. Pak, "Fabrication of a peristaltic PDMS micropump," *Sensors Actuators, A Phys.*, vol. 123–124, pp. 453–458, 2005.

[171] A. Tuantranont, W. Mamanee, T. Lomas, N. Porntheerapat, N. V. Afzulpurkar, and A. Wisitsoraat, "A three-stage thermopneumatic peristaltic micropump for PDMS-based micro/nanofluidic systems," *2007 7th IEEE Int. Conf. Nanotechnol. - IEEE-NANO 2007, Proc.*, pp. 1203–1206, 2007.

[172] W. Mamanee, a Tuantranont, N. V Afzulpurkar, N. Porntheerapat, S. Rahong, and a Wisitsoraat, "PDMS Based Thermopnuematic Peristaltic Micropump for Microfluidic Systems," *J. Phys. Conf. Ser.*, vol. 34, pp. 564–569, 2006.

[173] B. T. Chia, H. H. Liao, and Y. J. Yang, "A novel thermo-pneumatic peristaltic micropump with low temperature elevation on working fluid," *Sensors Actuators, A Phys.*, vol. 165, no. 1, pp. 86–93, 2011.

[174] S. Guo, X. Sun, K. Ishii, and J. Guo, "SMA actuator-based novel type of peristaltic micropump," *Proc. 2008 IEEE Int. Conf. Inf. Autom. ICIA 2008*, pp. 1620–1625, 2008.

[175] X. Sun, Y. Hao, S. Guo, X. Ye, and X. Yan, "The development of a new type of compound peristaltic micropump," *2008 IEEE Int. Conf. Robot. Biomimetics, ROBIO 2008*, pp. 698–702, 2008.

[176] P. Gravesen and J. Branebjerg, "Microfluidics-a review," *ournal of micromechanics and microengineering*, vol. 3, no. 4, p. 168, 1993.

[177] E. Stemme and G. Stemme, "A valveless diffuser/nozzle-based fluid pump," *Sensors Actuators A Phys.*, vol. 39, no. 2, pp. 159–167, Nov. 1993.

[178] C. R. Tamanaha, L. J. Whitman, and R. J. Colton, "Hybrid macro–micro fluidics system for a chip-based biosensor," *J. Micromechanics Microengineering*, vol. 12, no. 2, pp. N7–N17, Mar. 2002.

[179] M. Khoo and C. Liu, "A novel micromachined magnetic membrane microfluid pump," *Proc. 22nd Annu. Int. Conf. IEEE Eng. Med. Biol. Soc. (Cat. No.00CH37143)*, vol. 3, pp. 4–7, 2000.

[180] A. R. Gamboa, C. J. Morris, and F. K. Forster, "Improvements in Fixed-Valve Micropump Performance Through Shape Optimization of Valves," *J. Fluids Eng.*, vol. 127, no. 2, p. 339, 2005.

[181] N. Tesla, "Valvular conduit.," 1,329,559, 1920.

[182] I. Izzo, D. Accoto, A. Menciassi, L. Schmitt, and P. Dario, "Modeling and experimental validation of a piezoelectric micropump with novel no-moving-part valves," *Sensors Actuators, A Phys.*, vol. 133, no. 1, pp. 128–140, 2007.

[183] T. T. Nguyen, M. Pham, and N. S. Goo, "Development of a Peristaltic Micropump for Bio-Medical Applications Based on Mini LIPCA," *J. Bionic Eng.*, vol. 5, no. 2, pp. 135–141, 2008.

[184] C.-W. Huang, C. Hua, C.-W. Huang, and G.-B. Lee, "A microfluidic system for automatic cell culture A microfluidic system for automatic cell culture *," *J. Micromechanics Microengineering*, vol. 17, no. 7, pp. 7–8, Jul. 2008.

[185] Z. Chen, A. A. Mikulec, M. J. McKenna, W. F. Sewell, and S. G. Kujawa, "A method for intracochlear drug delivery in the mouse," *J. Neurosci. Methods*, vol. 150, no. 1, pp. 67–73, 2006.

[186] R. Inamoto, T. Miyashita, K. Akiyama, T. Mori, and N. Mori, "Endolymphatic sac is involved in the regulation of hydrostatic pressure of cochlear endolymph," *Am. J. Physiol. Integr. Comp. Physiol.*, vol. 297, no. 5, pp. R1610–R1614, 2009.

[187] a Geipel *et al.*, "A novel two-stage backpressure-independent micropump: modeling and characterization," *J. Micromechanics Microengineering*, vol. 17, no. 5, pp. 949–959, 2007.

[188] Y. Tanaka, "A peristaltic pump integrated on a 100% glass microchip using computer controlled piezoelectric actuators," *Micromachines*, vol. 5, no. 2, pp. 289–299, 2014.

[189] B. T. Chia, H.-H. Liao, and Y.-J. Yang, "A NOVEL THERMO-PNEUMATIC PERISTALTIC MICROPUMP WITH LOW TEMPERATURE ELEVATION Department of Mechanical Engineering , National Taiwan University , Taipei , TAIWAN," *TRANSDUCERS 2009 - 2009 Int. Solid-State Sensors, Actuators Microsystems Conf.*, pp. 8–11, Jun. 2009.

[190] R. Bodén, M. Lehto, U. Simu, G. Thornell, K. Hjort, and J. Å. Schweitz, "A polymeric paraffin actuated high-pressure micropump," *Sensors Actuators, A Phys.*, vol. 127, no. 1, pp. 88–93, 2006.

[191] S. Ogden, L. Klintberg, G. Thornell, K. Hjort, and R. Bodén, "Review on miniaturized paraffin phase change actuators, valves, and pumps," *Microfluid. Nanofluidics*, vol. 17, no. 1, pp. 53–71, 2014.

[192] Q. Kong, J. Ma, and C. Che, "Theoretical and experimental study of volumetric change rate during phase change process," *Int. J. Energy Res.*, vol. 33, no. 5, pp. 513–525, Apr. 2009.

[193] R. Bodén, K. Hjort, J.-Å. Schweitz, and U. Simu, "A metallic micropump for high-pressure microfluidics," *J. Micromechanics Microengineering*, vol. 18, no. 11, p. 115009, 2008.

[194] H. Li, X. Liu, and G. Fang, "Preparation and characteristics of n-nonadecane/cement composites as thermal energy storage materials in buildings," *Energy Build.*, vol. 42, no. 10, pp. 1661–1665, 2010.

[195] C. Vélez, J. M. Ortiz De Zárate, and M. Khayet, "Thermal properties of n-pentadecane, n-heptadecane and n-nonadecane in the solid/liquid phase change region," *Int. J. Therm. Sci.*, vol. 94, pp. 139–146, 2015.

[196] D. Oliver *et al.*, "Intracellular anions as the voltage sensor of prestin, the outer hair cell motor protein," *Science (80-.).*, vol. 292, no. 5525, pp. 2340–2343, Jun. 2001.

[197] W. E. Brownell, "Outer hair cell electromotility and otoacoustic emissions.," *Ear Hear.*, vol. 11, no. 2, pp. 82–92, 1990.

[198] C. Abdala and L. Visser-Dumont, "Distortion product otoacoustic emissions: A tool for hearing assessment and scientific study," *Volta Rev.*, vol. 103, no. 4, pp. 281–302, 2001.

[199] Www.otoemissions.org, "Introduction: Distortion Product Otoacoustic Emissions (DPOAE)." [Online]. Available: https://www.otoemissions.org/old/definitions/DPOAE.html.

[200] R. D. Frisina, B. Ding, X. Zhu, and J. P. Walton, "Age-related hearing loss: Prevention of threshold declines, cell loss and apoptosis in spiral ganglion neurons," *Aging (Albany. NY).*, vol. 8, no. 9, pp. 2081–2099, Sep. 2016.

[201] J. Raju *et al.*, "Diosgenin , a Steroid Saponin of Trigonella foenum graecum (Fenugreek), Inhibits Azoxymethane-Induced Aberrant Crypt Foci Formation in F344 Rats and Induces Apoptosis in HT-29 Human Colon Cancer Cells Diosgenin , a Steroid Saponin of Trigonella foenum g," *Cancer Epidemiol. Biomarkers Prev.*, vol. 13, no. 1, pp. 1392–1399, 2004.

[202] A.-M. Francoeur and A. Assalian, "MICROCAT: A Novel Cell Proliferation and Cytotoxicity Assay Based on WST-1," *Biochemica*, vol. 3, no. 3, pp. 19–25, 1996.

[203] C. L. Stevenson, J. T. Santini, and R. Langer, "Reservoir-based drug delivery systems utilizing microtechnology," *Adv. Drug Deliv. Rev.*, vol. 64, no. 14, pp. 1590–1602, 2012.

[204] J. H. Sakamoto *et al.*, "Enabling individualized therapy through nanotechnology," *Pharmacological Research*, vol. 62, no. 2. Academic Press, pp. 57–89, 01-Aug-2010.

[205] R. A. M. Receveur, F. W. Lindemans, and N. F. De Rooij, "Microsystem technologies for implantable applications," *Journal of Micromechanics and Microengineering*, vol. 17, no. 5. IOP Publishing, pp. R50–R80, 01-May-2007.

[206] A. C. R. Grayson *et al.*, "A BioMEMS review: MEMS technology for physiologically integrated devices," in *Proceedings of the IEEE*, 2004, vol. 92, no. 1, pp. 6–21.

[207] M. Staples, K. Daniel, M. J. Cima, and R. Langer, "Application of micro- and nano-electromechanical devices to drug delivery," *Pharmaceutical Research*, vol. 23, no. 5. pp. 847–863, 05-May-2006.

[208] *Thomson Physicians' Desk Reference*, 63rd ed. Montvale, NJ: Thomson Publishing, 2009.

[209] Y. E. Choonara, V. Pillay, M. P. Danckwerts, T. R. Carmichael, and L. C. Du Toit, "A review of implantable intravitreal drug delivery technologies for the treatment of posterior segment eye diseases," *Journal of Pharmaceutical Sciences*. 2010.

[210] G. E. Sanborn *et al.*, "Sustained-Release Ganciclovir Therapy for Treatment of Cytomegalovirus Retinitis: Use of an Intravitreal Device," *Arch. Ophthalmol.*, 1992.

[211] T. J. Smith *et al.*, "Intravitreal Sustained-Release Ganciclovir," *Arch. Ophthalmol.*, 1992.

[212] P. Mruthyunjaya *et al.*, "Efficacy of low-release-rate fluocinolone acetonide intravitreal implants to treat experimental uveitis," *Arch. Ophthalmol.*, 2006.

[213] D. G. Callanan, G. J. Jaffe, D. F. Martin, P. A. Pearson, and T. L. Comstock, "Treatment of posterior uveitis with a fluocinolone acetonide implant: Three-year

clinical trial results," *Arch. Ophthalmol.*, 2008.

[214] B. D. Kuppermann, "Implant delivery of corticosteroids and other pharmacologic agents," *Retina*, pp. 10–11, 2006.

[215] A. C. Richards Grayson *et al.*, "Multi-pulse drug delivery from a resorbable polymeric microchip device," *Nat. Mater.*, 2003.

[216] G. Y. Kim *et al.*, "Resorbable polymer microchips releasing BCNU inhibit tumor growth in the rat 9L flank model," *J. Control. Release*, 2007.

[217] A. C. R. Grayson, M. J. Cima, and R. Langer, "Molecular release from a polymeric microreservoir device: Influence of chemistry, polymer swelling, and loading on device performance," *J. Biomed. Mater. Res. - Part A*, 2004.

[218] "http://www.debiotech.com/." [Online]. Available: http://www.debiotech.com/.

[219] L.-D. Piveteau, H. Hofmann, and F. Neftel, "Anisotropic nanoporous coatings for medical implants." Google Patents, 09-Jul-2009.

[220] D. Capodanno, F. Dipasqua, and C. Tamburino, "Novel drug-eluting stents in the treatment of de novo coronary lesions," *Vascular Health and Risk Management*. 2011.

[221] E. Grube *et al.*, "A novel paclitaxel-eluting stent with an ultrathin abluminal biodegradable polymer: 9-month outcomes with the jactax hd stent," *JACC Cardiovasc. Interv.*, 2010.

[222] P. J. T. A.N. Paisley, "Recent advances in the treatment of acromegaly," *Recent Adv. Investig. Drugs*, vol. 15, pp. 251–256, 2006.

[223] F. Martin *et al.*, "Tailoring width of microfabricated nanochannels to solute size can be used to control diffusion kinetics," *J. Control. Release*, 2005.

[224] P. Gardner, "Use of a nanopore membrane in novel a drug delivery device," *Futur. Drug Deliv.*, pp. 59–60, 2006.

[225] C. L. Stevenson, F. Theeuwes, and J. C. Wright, "Osmotic implantable delivery systems," *Handb. Pharm. Control. Release Technol.*, 2000.

[226] J. C. Wright *et al.*, "An in vivo/in vitro comparison with a leuprolide osmotic implant for the treatment of prostate cancer," *J. Control. release*, vol. 75, no. 1–2, pp. 1–10, 2001.

[227] C. L. Stevenson, "Formulation of leuprolide at high concentration for delivery from a one-year duration implant," in *Protein Formulation and Delivery, Second Edition*, CRC Press, 2007, pp. 171–194.

[228] D. M. Fisher, N. Kellett, and R. Lenhardt, "Pharmacokinetics of an implanted osmotic pump delivering sufentanil for the treatment of chronic pain," *Anesthesiology*, 2003.

[229] "www.intarcia.com." [Online]. Available: www.intarcia.com.

[230] T. A. B. Yang, C. Negulescu, R. D'vas, C. Eftimie, J. Carr, S. Lautenbach, K. Horwege, C. Mercer, D. Ford, "Stability of ICTA 560 for continuous subcutaneous delivery of Exenatide at body temperature for 12 months," in *2009 Diabetes Technology Meeting*, 2009.

[231] H. R.R., C. R., R. J., A. T., and L. K., "Comparing ITCA 650, continuous subcutaneous delivery of exenatide via DUROS(registered trademark) device, vs. twice daily exenatide injections in metformintreated type 2 diabetes," in *Diabetologia*, 2010.

[232] D. F. B. Yang, T. Alessi, C. Rohloff, R. Mercer, C. Negulescu, S. Lautenbach, J. Gumucio, M. Guo, E. Weeks, J. Carr, "Continuous delivery of proteins and peptides at consistent rates for at least 3 months form the DUROS® device,, Poster T3150," in *AAPS 2008 Meeting,*.

[233] C. M. Rohloff, T. R. Alessi, B. Yang, J. Dahms, J. P. Carr, and S. D. Lautenbach, "DUROS®technology delivers peptides and proteins at consistent rate continuously for 3 to 12 months," *J. Diabetes Sci. Technol.*, 2008.

[234] R. Sheybani, A. Cobo, and E. Meng, "Wireless programmable electrochemical drug delivery micropump with fully integrated electrochemical dosing sensors," *Biomed. Microdevices*, vol. 17, no. 4, pp. 1–13, 2015.

[235] A. J. Chung, Y. S. Huh, and D. Erickson, "A robust, electrochemically driven microwell drug delivery system for controlled vasopressin release," *Biomed. Microdevices*, vol. 11, no. 4, pp. 861–867, 2009.

[236] N. M. Elman, H. L. Ho Duc, and M. J. Cima, "An implantable MEMS drug delivery device for rapid delivery in ambulatory emergency care," *Biomed. Microdevices*, vol. 11, no. 3, pp. 625–631, 2009.

[237] R. Lo, P.-Y. Li, S. Saati, R. Agrawal, M. S. Humayun, and E. Meng, "A refillable microfabricated drug delivery device for treatment of ocular diseases," *Lab Chip*, vol. 8, no. 7, p. 1027, 2008.

[238] R. Lo, P.-Y. Li, S. Saati, R. N. Agrawal, M. S. Humayun, and E. Meng, "A passive MEMS drug delivery pump for treatment of ocular diseases.," *Biomed. Microdevices*, vol. 11, no. 5, pp. 959–70, Oct. 2009.

[239] A. Cobo, R. Sheybani, H. Tu, and E. Meng, "A wireless implantable micropump for chronic drug infusion against cancer," *Sensors Actuators A Phys.*, vol. 239, pp. 18–

25, 2016.

[240] H. Gensler, R. Sheybani, P. Y. Li, R. Lo Mann, and E. Meng, "An implantable MEMS micropump system for drug delivery in small animals," *Biomed. Microdevices*, vol. 14, no. 3, pp. 483–496, 2012.

[241] "Debiotech." [Online]. Available: https://www.debiotech.com. [Accessed: 14-Oct-2018].

[242] E. Zini *et al.*, "Use of an implantable pump for controlled subcutaneous insulin delivery in healthy cats," *Vet. J.*, vol. 219, pp. 60–64, 2017.

[243] F. N. Pirmoradi, J. K. Jackson, H. M. Burt, and M. Chiao, "On-demand controlled release of docetaxel from a battery-less MEMS drug delivery device," *Lab Chip*, vol. 11, no. 16, pp. 2744–2752, 2011.

[244] Y. B. Gianchandani, S. Chiravuri, R. Y. Gianchandani, T. Li, and A. T. Evans, "Compact, power-efficient architectures using microvalves and microsensors, for intrathecal, insulin, and other drug delivery systems," *Adv. Drug Deliv. Rev.*, vol. 64, no. 14, pp. 1639–1649, 2012.

[245] D. Reynaerts, J. Peirs, H. Van Brussel, and K. U. Leuven, "A SMA-ACTUATED IMPLANTABLE SYSTEM FOR DELIVERY OF LIQUID DRUGS," no. June, pp. 26–28, 1996.

[246] M. Wook, S. An, S. S. Yoon, and A. L. Yarin, "Advances in self-healing materials based on vascular networks with mechanical self-repair characteristics," vol. 252, pp. 21–37, 2018.

[247] R. F. Shepherd, A. A. Stokes, R. M. D. Nunes, and G. M. Whitesides, "Soft machines that are resistant to puncture and that self seal," *Adv. Mater.*, vol. 25, no. 46, pp. 6709–6713, 2013.

[248] L. E. F. Circuits and P. Elast, "Re-configu le fluid circuits," *Science (80-.).*, pp. 222–227.

[249] M. K. Chaudhury and G. M. Whitesides, "Direct Measurement of Interfacial Interactions between Semispherical Lenses and Flat Sheets of Poly(dimethylsiloxane) and Their Chemical Derivatives," *Langmuir*, vol. 7, no. 5, pp. 1013–1025, 1991.

[250] J. C. Andrews, S. C. Walker-Andrews, and W. D. Ensminger, "Long-term central venous access with a peripherally placed subcutaneous infusion port: initial results.," *Radiology*, vol. 176, no. 1, pp. 45–47, Jul. 1990.

[251] S. S., M. J., K. A., and J. C., "Improved methods for venous access: The Port-A-Cath, a totally implanted catheter system," *J. Clin. Oncol.*, vol. 4, no. 4, pp. 596–

603, 1986.

[252] "Prometra Pump | Flowonix." [Online]. Available: http://www.flowonix.com/healthcare-provider/products/prometra-pump.

[253] "ithetis Implantable Drug Delivery Devices." [Online]. Available: http://www.ithetis.com.

[254] R. Lo *et al.*, "A passive refillable Intraocular MEMS drug delivery device," *Int. Conf. Microtechnologies Med. Biol.*, no. May, pp. 74–77, 2006.

[255] P. Y. Li *et al.*, "An electrochemical intraocular drug delivery device," *Sensors Actuators, A Phys.*, vol. 143, no. 1, pp. 41–48, 2008.

[256] A. T. Evans, S. Chiravuri, and Y. B. Gianchandani, "A Multidrug Delivery System Using a Piezoelectrically Actuated Silicon Valve Manifold With Embedded Sensors," *J. Microelectromechanical Syst.*, vol. 20, no. 1, pp. 231–238, 2011.

[257] F. L. Trull and B. A. Rich, "More regulation of rodents," *Science*, 1999.

[258] E. Benedikz, E. Kloskowska, and B. Winblad, "The rat as an animal model of Alzheimer's disease," *Journal of Cellular and Molecular Medicine*. 2009.

[259] J. Urquhart, "Rate-Controlled Delivery Systems in Drug and Hormone Research," *Annu. Rev. Pharmacol. Toxicol.*, vol. 24, no. 1, pp. 199–236, Apr. 2002.

[260] D. J. Laser and J. G. Santiago, "A review of micropumps," *J. Micromechanics Microengineering*, vol. 14, no. 6, pp. R35–R64, 2004.

[261] R. Lo and E. Meng, "Integrated and reusable in-plane microfluidic interconnects," *Sensors Actuators, B Chem.*, vol. 132, no. 2, pp. 531–539, 2008.

[262] H. M. Gensler and H. M. Gensler, "A Wireless Implantable MEMS Micropump System for Site-specific Anti-cancer Drug Delivery by Copyright 2013," no. December, 2013.

[263] S. coating Systems, "SCS Parylene properties." [Online]. Available: https://scscoatings.com.

[264] "Hamilton reference guide - Syringes and Needles." [Online]. Available: www.hamiltoncompany.com.

[265] R. Rauck *et al.*, "Accuracy and efficacy of intrathecal administration of morphine sulfate for treatment of intractable pain using the Prometra® Programmable Pump," *Neuromodulation*, vol. 13, no. 2, pp. 102–107, 2010.

[266] A. Sherer and L. B. Kinter, "A Guide to Manufacture, Surgical Implantation,

Maintenance and Use of Micro-Renathane® Vascular Catheters in Laboratory Animals." [Online]. Available: https://www.braintreesci.com/images/MREMANUAL.pdf.

[267] Y. Liu *et al.*, "In vitro and in vivo pharmacokinetic study of a dexamethasone-releasing silicone for cochlear implants."

[268] S. G. Vallejo-Heligon, B. Klitzman, and W. M. Reichert, "Characterization of Porous, Dexamethasone-Releasing Polyurethane Coatings for Glucose Sensors," 2014.

[269] L. W. Norton, H. E. Koschwanez, N. A. Wisniewski, B. Klitzman, and W. M. Reichert, "Vascular endothelial growth factor and dexamethasone release from nonfouling sensor coatings affect the foreign body response," 2007.

[270] S. G. Vallejo-Heligon, N. L. Brown, W. M. Reichert, and B. Klitzman, "Porous, Dexamethasone-loaded polyurethane coatings extend performance window of implantable glucose sensors in vivo," *Acta Biomater.*, vol. 30, pp. 106–115, Jan. 2016.

[271] M. J. Williams *et al.*, "A Low-Cost, Rapidly Integrated Debubbler (RID) Module for Microfluidic Cell Culture Applications," *Micromachines*, vol. 10, no. 6, p. 360, May 2019.

[272] K. W. Oh, K. Lee, B. Ahn, and E. P. Furlani, "Design of pressure-driven microfluidic networks using electric circuit analogy," *Lab Chip*, vol. 12, no. 3, pp. 515–545, 2012.

[273] R. Deng, Y. Cheng, and C. H. Wang, "Experiments and simulation on a pulse dampener system for stabilizing liquid flow," *Chem. Eng. J.*, vol. 210, pp. 136–142, 2012.

[274] C. K. Byun, K. Abi-Samra, Y. K. Cho, and S. Takayama, "Pumps for microfluidic cell culture," *Electrophoresis*, vol. 35, no. 2–3, pp. 245–257, 2014.

[275] T. T. Veenstra, N. R. Sharma, F. K. Forster, J. G. E. Gardeniers, M. C. Elwenspoek, and A. Van den Berg, "The design of an in-plane compliance structure for microfluidical systems," *Sensors Actuators, B Chem.*, vol. 81, no. 2–3, pp. 377–383, 2002.

[276] B. Yang and Q. Lin, "A compliance-based microflow stabilizer," *J. Microelectromechanical Syst.*, vol. 18, no. 3, pp. 539–546, 2009.

[277] M. M. Kenisarin, "Thermophysical properties of some organic phase change materials for latent heat storage. A review," *Sol. Energy*, vol. 107, no. September 2014, pp. 553–575, 2014.

[278] "Engineering Toolbox." [Online]. Available: https://www.engineeringtoolbox.com/convective-heat-transfer-d_430.html.

Appendix A. Details of COMSOL® heat transfer model

A.1   Model Geometry

The detailed geometry of the micropump was made in Solidworks® and imported to COMSOL (Figure A.1). Although the microtubing and fluid in it have a circular cross section, they were modeled as a square shaped cross section due to importing difficulties using COMSOL Multiphysics. All four layers of the copper in the PCB are considered but are masked by PCB in the schematic view.
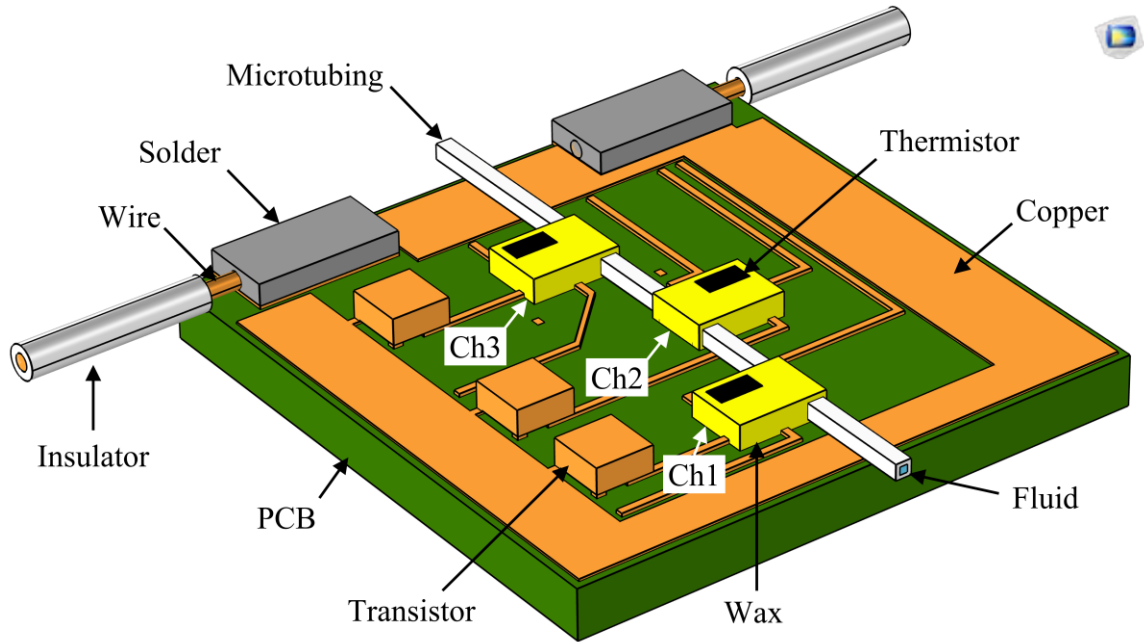
Figure A.1. The model geometry of the micropump used in the COMSOL simulation. The resin around the chambers and on top of it are not shown. The resistive heaters in the chambers are covered with wax. All four layers of the copper are considered in the geometry model, but in this view they are masked with PCB.

A.2   Model validation

The COMSOL model was validated at the primitive step of analysis by comparing with a micropump working in air environment. Two validation schemes of steady and transient state were investigated, both in air environment. In the steady state one the two side chambers (chambers 1 & 3, see Figure A.1) were turned on for 10 min, while chamber 2 was off and its temperature was increased due to the heat from side chambers. The comparison between numerical and experimental results shows acceptable matching (Figure A.2). In the transient experiment two side chambers were turned on for 10 s and turned off for 10 s. During the 20 s chamber 2 was off. The numerical results are consistent with experimental data (Figure A.3). In both experiments the heating chambers work with

15 mW power which was the power of the pump in the experiment. In both graphs values for chamber 3 are not shown, since they are almost identical with chamber 1. The consistency between the experimental data and numerical model validates the model for further design and analysis for both steady and transient states.
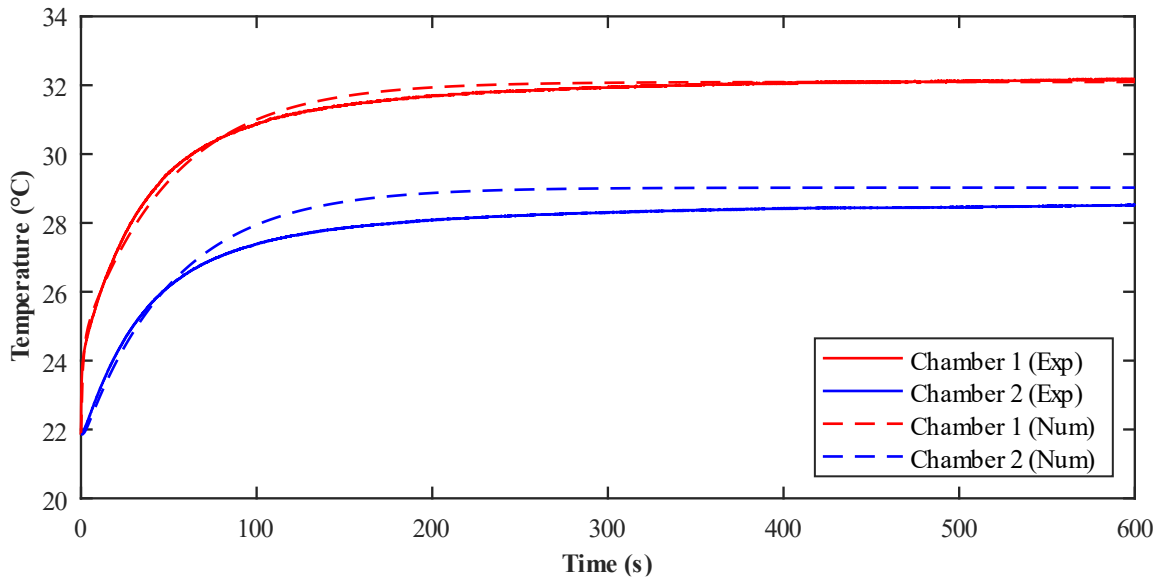
Figure A.2. Consistency between numerical and experimental data where two side chambers are on and the middle chamber is off shows validity of the model to predict steady state conditions.
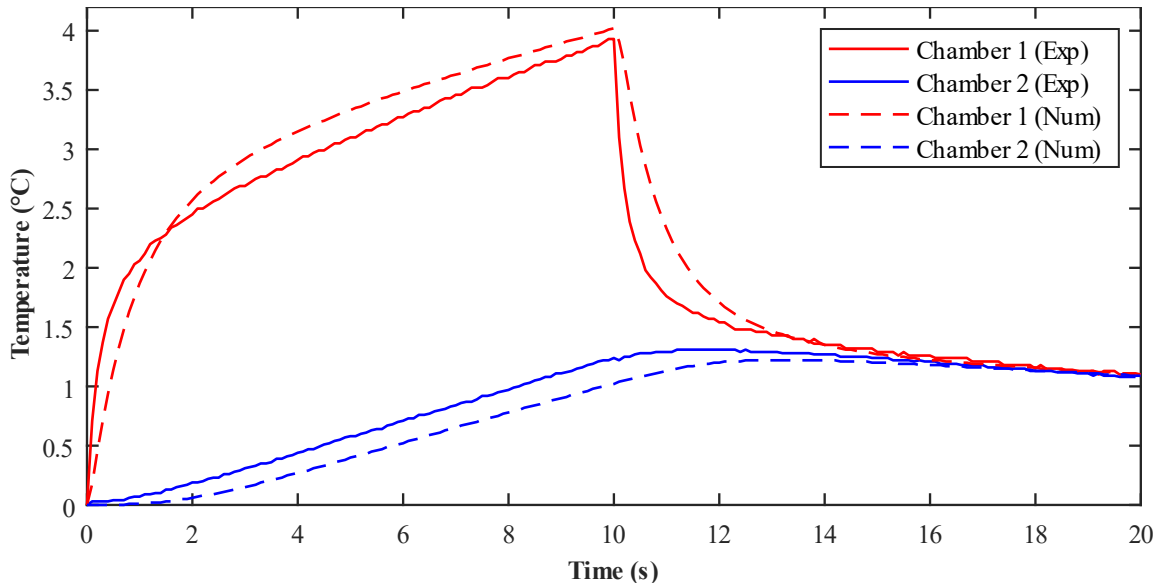
Figure A.3. Consistency between numerical and experimental data where two side chambers are on for 10 s and off for 10 s, while the middle chamber is off shows validity of the model to predict transient conditions.

A.3   Material properties

Table A.1 shows the material properties of key parameters in the model. The drug in the microtubing is modeled as water since the large percentage of the drugs are made of water. Water (*water, liquid* in COMSOL) properties are defined in COMSOL library. The density of the wax is adjusted based on the mass in the device. The material properties of the thermistors and resistors were found according to manufacturer datasheet. The transistor is considered as copper.

The material for wire is considered copper. The wire length was modeled 100 times smaller than the realistic ones, which are unproportionally long (~30 cm) for such a small device (0.8×0.8 cm^2). Therefore, the density and thermal conductivity are adjusted accordingly.

183

For a long component such as the wire the heat transfer can be estimated 1-D along the length of the wire. The simplified equation for conduction is $Q_{conduction} = kA\Delta T/d$, where k, A, ΔT, and d are thermal conductivity, surface area, temperature difference, and distance. Since in this model d is 100 times smaller than the realistic value, $k_{equivalent}$ was 100 times reduced (from 400 to 4 W/mK) to have the $Q_{conduction}$ intact. Further, stored energy in the wire is defined as $Q_{stored} = mc\Delta T$ *where m,c, and ΔT* are mass of object, specific heat of object, and temperature difference. To keep the mass of the object fixed while having 100 times less length/volume, the density of the wire is considered 100 times of copper.

The thermal behavior of the wax (Nonadecane) however was modeled using apparent heat capacity method. In this method the phase-change phenomenon is modeled as a drastic change in the melting range by defining the specific heat as a function of temperature. This function was defined as a user-defined function (UDF) in the present COMSOL model. In this UDF, the latent heat of the wax (170 kj/kg) was spread over the phase-change temperature range of 4 °C [194], [195], [277]. Also the solid-solid energy of the wax is spread over 1 °C at 295 K [277]. Equation (A-1) shows the heat capacity of the wax as a function of temperature.

$$C_{p,wax}\ (T) = \begin{cases} 5000 & T < 294\ \text{K} \\ 14000 & 294\ \text{K} < T < 295\ \text{K} \\ 42500 & 302.65 < T < 306.65\ \text{K} \\ 5000 & T > 306.65\ \text{K} \end{cases} \qquad (\text{A-1})$$

Table A.1. Components and their material properties used in the COMSOL heat transfer simulation.

Component	Material	Density (kg/m³)	Specific heat (J/kgK)	Thermal conductivity (W/mK)
PCB	FR4	1900	1369	0.3
Copper traces	Copper	8960	384	401
Microtubing	Polyurethane	950	1800	0.29
Thermistor	Murata® NCP series*	4247	1128	120
Resistive heater	Panasonic® ERJ series*	3900	900	27
Super glue	Fastcap® 2P-10*	1043	850	0.1
Solder	60Sn-40Pb 1	9000	150	50
Wire	Copper	896000†	384	4†
Drug	Water	997	4157	606
Paraffin wax	Nonadecane $CH_3(CH_2)_{17}CH_3$*	1435	$C_{p,wax}$ (T)	0.22

*Material was found from or based on manufacturer release data. Other materials were in COMSOL library.
†Equivalent values based on the simplified geometry.

A.4 Boundary conditions

The external surface of the model are exposed to free convection in water with adjusted convection coefficient of 1200 W/m²°K, which falls in the typical range for free convection in water and liquids (50-3000 W/m² K)[278]. The convection coefficient was tuned by matching a sample test with experimental pump model. For all the simulations the power of the heaters (P) are 80.6 mW which is consistent with having 1.8 V across 40.2 Ω resistive heaters in the pumps. Similar to the pumps, a closed-loop control limits the generated heat in the chambers. Further, each chamber follows a peristaltic sequence. The generated heat in the chambers are therefore defined as:

$$P_{boundary} = P \times h(t) \times (T_{chamber} < T_{set}) \tag{A-2}$$

where $P_{boundary}$, $h(t)$, $T_{chamber}$, and T_{set} stand for applied heat to the chamber, ON/OFF (1 or 0) condition of the chamber based on peristaltic cycle, temperature of the chamber sensed by the thermistor, and set temperature of the chamber. Figure A.4 shows the peristaltic cycle of chamber 1 defined in the COMSOL model.
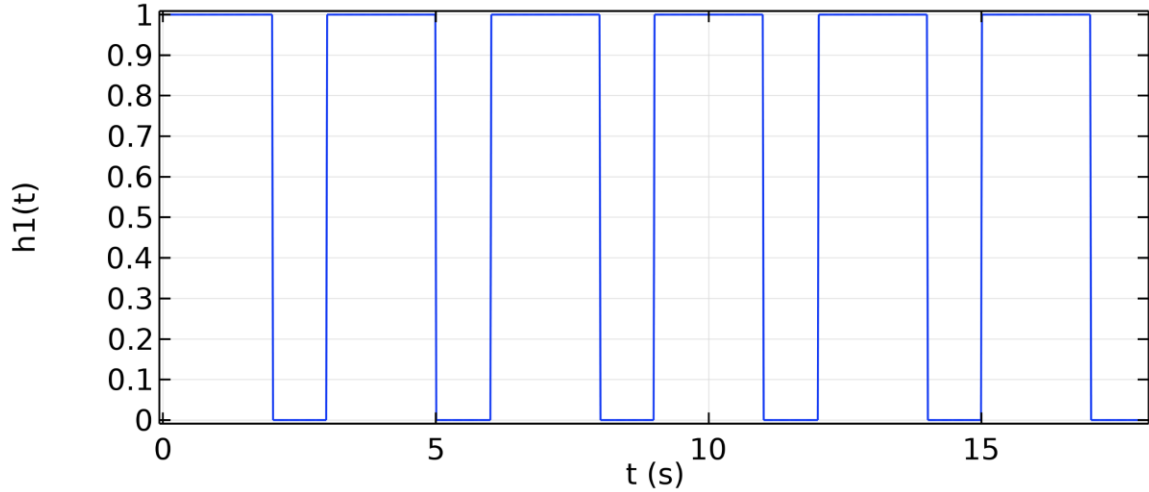
Figure A.4. A sample peristaltic cycle of chamber 1. Similar cycles are defined for chambers 2 and 3 with phase-lags of 120° and 240°.

The radiation between the pump external surface and the surrounding is neglected since it is orders of magnitude smaller than the convection heat transfer. If the pump is considered a small object in a large enclosure the formula for radiation is:

$$Q = \sigma \, \varepsilon \, A \, (T_1^4 - T_2^4) \tag{A-3}$$

where σ, ε, A, T_1, and T_2 are Stefan-Boltzmann constant (5.669×10^{-8} W/m^2 K^4), emissivity of the body, pump overall surface, pump surface temperature, and ambient temperature, respectively. Considering $\varepsilon = 1$, $A = 2.24 \times 10^{-4}$ (pump dimensions: $8 \times 8 \times 3$ mm^3), and (according to COMSOL simulation results) pump external temperature 0.3 higher than the ambient temperature (20 °C), the power loss due to radiation is 0.38 mW. This value is three orders of magnitude smaller than the convection at the same conditions, demonstrating validity of the assumption of neglecting radiation.

187

By using the *COMSOL® Heat Transfer in Solids* module, the convection in the chamber due to phase change from solid to liquid is neglected. It is a simplification of the simulation, since considering phase-change phenomenon required *Heat Transfer in Fluids* module and using COMSOL Multiphysics® to model their interaction which significantly increase the calculation cost. Instead, some of the parameters in the model were tuned by comparison to experimental models.

A.5   Geometry optimization

The COMSOL model was used to optimize the geometry of the pump. The four copper layers in the PCB are the most important element beside the wax, due to high thermal mass and conductivity. Two changes in the copper structure was examined: thinning the copper layers from 36 μ down to 18 μm, spreading copper in the chamber. Due to limitations of the manufacturer we could not reduce the thickness of the copper at the external layers, therefore, just two middle layers were thinned.

A set of experiment was designed to examine effects of each of these geometry modifications. Three models were made: *Reference*, *Spread copper*, and *Thin copper*. The *Reference* model has copper layers with 36 μm thickness, without copper spread in the chamber. The *spread copper* model has the same copper thickness, with an additional sheet of copper connected to thermistors and resistors spread in the chamber. The *Thin copper* model has two internal layers of 18 μm, without any spread of the copper in the chamber.

A peristalsis sequence of 101, 110, 011 is considered (1 is ON, 0 is OFF, numbers in the order of chamber number). The test here has two steps. At the first step the pump is at steady state at phase 3 of the peristalsis cycle (011), where chamber 1 is off and chamber 2 and 3 are ON. At the second step a transition between phase 3 to phase 1 occurs (011 → 101), where chamber 1 is powered on with a realistic power of 80.6 mW, chamber 2 is turned off, and chamber 3 is kept at the set temperature. No closed-loop control on the chamber temperature is applied here, to save computational cost. The results presented in this section are for the second step which runs for 3s. The wax for this simulation is Nonadecane, with a melting range of 4 °C around 32 °C. All temperatures are relative to ambient temperature.

Comparison of the wax temperature of the *Reference* and *Spread copper* shows that spreading copper in the chamber increases the actuation frequency by 21% (Figure A.5). In other word, the temperature of the wax in the chamber can get to the set temperature faster. In addition, a histogram graph is generated to show the distribution of temperature in the chamber, at the moment that the wax in each chamber reaches the set temperature (i.e., t ≈ 2s for the *Reference*, and t ≈ 1.7s for the *Spread copper*). In the *Reference*, the temperature elevation of the wax is distributed in a range of ~ 3-20 °C, with a relatively flat profile. In converse, in the *Spread copper* a significant peak of the amount of the wax in melting range can be observed (Figure A.6). The temperature elevation range also reduces to ~5-17 °C. The spread copper reduces the temperature standard deviation by 35%. The results of Thin copper shows that using thinner copper layers can increase the actuation frequency by 55% (Figure A.7).
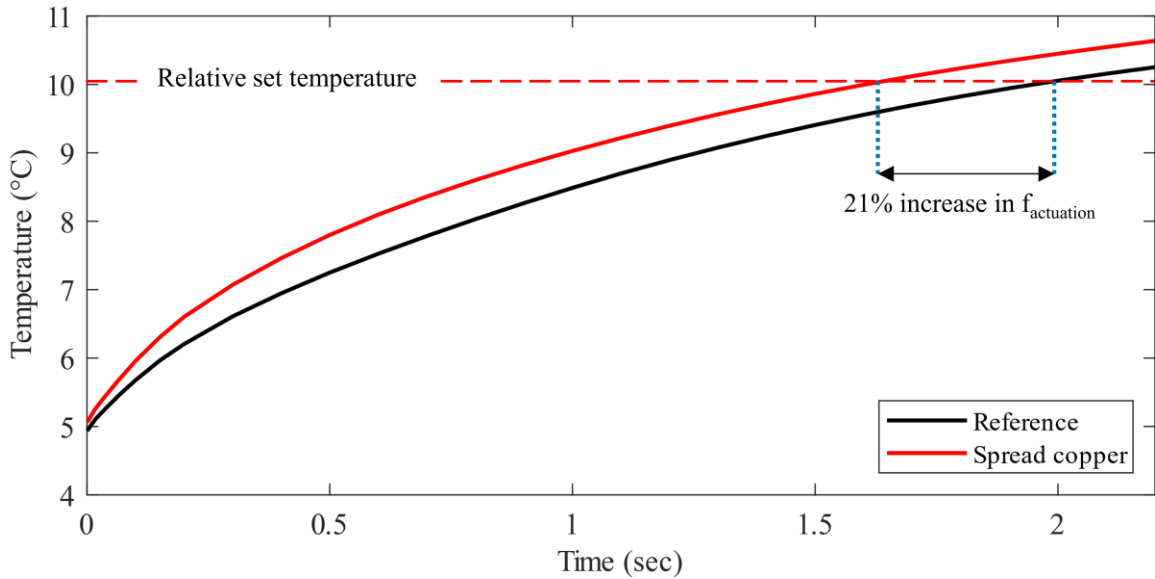
Figure A.5. Comparison of the temperature elevation of the wax in chamber 1 shows that spreading the copper increases the actuation frequency by 21%.
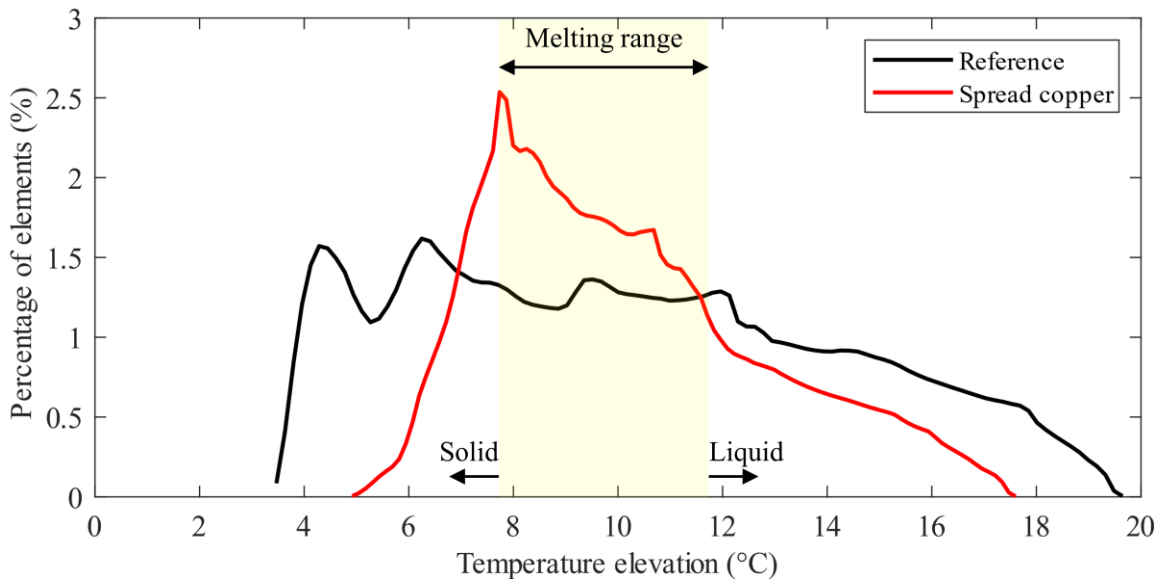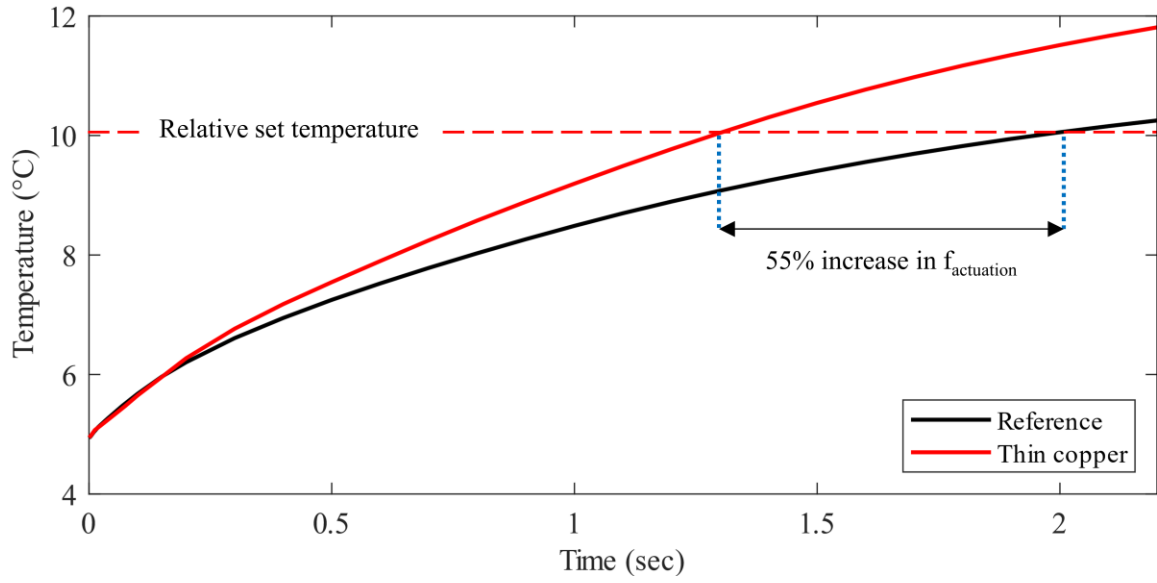

Figure A.6. Temperature distribution of the wax in chamber 1, at the time that it reaches the set temperature shows a significant improve in the homogeneity of the temperature using the _Spread copper_, compared to _Reference_. Spread copper reduces the temperature standard deviation by 35%.

Figure A.7. Reducing the thickness of the copper layers on the PCB increases the operation frequency by 55% due to reduced thermal mass and heat transfer away from the chamber.